A Multi-Scale Cell-Based Model to Simulate and Elucidate the Mechanisms Controlling Tumor-Induced Angiogenesis

by

Amy L. Bauer

A dissertation submitted in partial fulfillment
of the requirements for the degree of
Doctor of Philosophy
(Mathematics)
in The University of Michigan
2007

Doctoral Committee:

Associate Professor Trachette L. Jackson, Co-Chair
Yi Jiang, Co-Chair, Los Alamos National Laboratory
Professor Daniel M. Burns Jr.
Associate Professor Denise E. Kirschner
Professor Charles D. Little, The University of Kansas Medical Center

Only those who will risk going too far can possibly find out how far one can go.

T.S. Eliot

Without the unconditional support and encouragement from my family and dear friends, this research would not have been completed. I dedicate this dissertation to them.

ACKNOWLEDGEMENTS

I gratefully acknowledge my advisers, Trace Jackson and Yi Jiang, for their superior scientific guidance and mentoring. Individually and collectively, you are an inspiring example of exceptional scientific ability and of what is possible to achieve as women in science. Thank you both for showing me the ropes and for your patience. I am grateful to my committee members: Professors Denise Kirschner, Dan Burns, and Charlie Little for their insightful and valuable comments. I would like to express my appreciation to the members of the Mathematical Analysis and Modeling Group at Los Alamos National Laboratory for providing the infrastructure (computing resources and programming training) critical to the computational component of this research. Heartfelt thanks to all who offered words of encouragement, expressed your belief in me, and offered personal and professional advice along the way, especially: SCH, DEK, NLJ, CPS, CAL, JH, RED, JAS, TdF, LBG, TSV, NEB, MOM, DAD.

TABLE OF CONTENTS

LIST OF FIGURES

Figure

LIST OF TABLES

Table

CHAPTER I

Introduction

Cancer kills one in four Americans. It is the leading cause of death in the United States [73]. Cancer invasion and metastasis depend on tumor-induced angiogenesis, which is the formation of new blood vessels from existing vasculature in response to chemical signals from a tumor. Angiogenesis marks the pivotal transition from benign solid tumor growth to vascular growth, a more progressive and potentially fatal stage of cancer beyond which cancer becomes extremely difficult to treat and survival rates decrease [156]. Angiogenesis is a complex process, involving multiple time scales and intricate interplay between biochemical and biomechanical mechanisms, including cell-cell and cell-matrix interactions, cell surface receptor binding, and intracellular signal transduction. The sequential morphogenetic processes required for angiogenesis to occur are well known and a thorough review of these processes is given in Chapter II; however, what is still not completely understood is how cellular and molecular mechanisms are coordinated to control these processes.

The processes that occur during angiogenesis span multiple time and length scales. These time and spatial scales can range from 10^{-2} seconds and 10^{-9} meters during gene transcription and protein production at the molecular level to 10^{6} seconds and 10^{-1} meters at the tissue and whole organ level. However, experimental investigations

and data generated from these investigations focus on specific mechanisms relegated to isolated time or length scales and must be translated between biological scales. For processes relevant to angiogenesis, this information exists at the whole organ and tissue level: where tumor cells develop into cancer and blood vessels grow to form vascular networks, the cellular level: where the study of the biomechanics of cell motility, growth, division, and apoptosis are central themes, and the molecular level: where investigations have led to detailed regulatory and signaling networks. A major challenge facing the modeling and the experimental research communities is to integrate this information in a way that improves our understanding of the principal underpinnings driving angiogenic processes and that will advance efforts aimed at the development of new therapies for treating cancer and other angiogenesis-dependent diseases.

A cell-based multi-scale approach to modeling angiogenesis, which is applicable to other biological systems as well, responds well to this challenge. Mammalian cells are only capable of a limited collection of behaviors. They can grow, divide, migrate, and synthesize biochemical products. However, even with all the impressive research focused on elucidating cellular regulation, scientists are still far from having the complete picture of a single cell and understanding how, from this rather limited repertoire of behaviors, cells cooperate to form very complex biological structures. Moreover, most of the phenomena that we eventually care about occur at the tissue and whole organism scale, for example as in cancer, and host-pathogen interactions leading to disease. A phenomenological description of cell behavior can provide a great deal of insight into these tissue level dynamics, much more than detailed but isolated segments of regulation networks and signaling pathways can ever hope to achieve. In addition, the ability to integrate a cell-based phenomenological model

with some detailed understanding at the regulation level becomes a powerful investigatory tool. Looking forward, coupling a tumor growth model [75] with a cell-based model of angiogenesis [12, 125] and the immune system response against the tumor will be a major step towards the development of an integrated systems approach to modeling tumor growth and cancer invasion and towards the ultimate goal of predicting the effects of novel cancer and anti-angiogenic therapies.

The research conducted for this dissertation concentrates on the development of a multi-scale model of angiogenesis that integrates tissue, cellular, and molecular level dynamics. This multi-scale model captures key biochemical and biomechanical interactions that occur between endothelial cells and the extracellular matrix. Using this model, we investigate the mechanisms responsible for promoting and inhibiting angiogenesis.

This dissertation is organized in the following manner. Chapter II provides a background to the biological processes involved in angiogenesis. This chapter highlights angiogenesis as the key event that enables a benign solid tumor to progress to cancer and metastasis. There is a discussion of the importance of the extracelluar matrix and critical signaling receptors and pathways as critical regulators of the morphologic events during angiogenesis. The chapter concludes with some historical milestones in the angiogenesis field.

Chapter III presents an overview of different mathematical modeling techniques used to describe biological systems and the need for multiple scale methods to capture and integrate the dynamics that frequently occur over widely varying time and length scales. This chapter includes a survey of existing mathematical models of angiogenesis and identifies their strengths and limitations. The choice of a cell-based model to investigate angiogenesis is based on the premise that the interactions that

govern angiogenic events are spatially and temporally localized and cell specific, that is, these interactions are regulated at the level of the individual cells.

The existing body of mathematical and physics research in angiogenesis is void of a model capable of capturing individual cellular behaviors and the fine details of newly formed vascular sprouts and in Chapter IV we present the first cell-based model of angiogenesis. Our approach is a hybrid model integrating continuous and discrete mathematical models. Specifically, cellular dynamics are described using a lattice Monte Carlo model, and a continuous partial differential equation incorporates extracellular chemical dynamics. Using this model, in Chapter V we explore the mechanisms driving different sprout morphologies and test several hypothesis proposed to provide insight on conflicting experimental data. The model is capable of simulating sprout branching and anastomosis, larger scale structures that emerge only as a result of the featured cellular and molecular level dynamics. This result is an important contribution to modeling angiogenesis as no other model has reproduced sprout branching without *a priori* prescribing phenomenological rules for these events. The results presented in Chapters IV and V have already been published in *Biophysical Journal* [12].

Then in Chapter VI, additional mechanisms for cellular motility and sprout extension are incorporated into the model. This extended model accurately reproduces and is validated against empirical measurements of sprout extension speed. Thus, the model can be used to study how extracellular matrix topography influences cell shape, intercellular and cell-matrix interactions, and multicellular sprout extension speed. We find distinct ranges of extracellular matrix density that specifically promote or interrupt sprout growth, and identify a density range optimal for sprout branching. The extended model and the results described in this chapter are in

revision for publication in *Biophysical Journal* [13].

As the first step towards a multi-scale model of angiogenesis, Chapter VII develops a Boolean network model for critical signal transduction pathways involved in regulating key cellular behaviors. This model is then used to understand how a cell interprets the biochemical signals initiated by key external stimuli involved in angiogenesis and the influence of these external signals on cellular function. The major contribution from this study is that it is the first to propose a network model that highlights the cross-talk between growth factor, integrin, and cadherin receptors.

Finally, in Chapter VIII, we integrate the intracellular signaling model from Chapter VII into the extended cellular model from Chapter VI and present a multiple scale model of angiogenesis. This integrated systems approach allows the removal of the phenomenological rules that determine cell phenotype. Instead, each cell is equipped with the internal decision making machinery to survey its local landscape and respond to external cues. The integrated model is used to examine how the external environment guides critical cellular decisions, including whether the cell is going to proliferate, migrate, or initiate apoptosis, and how these decisions influence sprout morphology. In previous models of angiogenesis, apoptosis has largely been neglected and cell quiescence has not been considered at all. Our multi-scale model captures both cell quiescence and apoptosis, and consequently, it can be used to investigate a whole new area of angiogenesis treatment strategies. The model produces some exciting results: the appearance of multiple branches, different proliferation regions, and the brush border effect. Our studies reveal a link between matrix density, cell phenotype, and sprout morphology. This multi-scale model is another step toward a whole systems approach to understanding how the mechanisms controlling angiogenesis are regulated and feedback on each other between hierarchical levels: from

tissue to individual cell to molecular signaling and back again.

The summary chapter IX discusses the impact of this research in a broader context and proposes future applications and extensions of the multi-scale model.

CHAPTER II

Biological Background to Angiogenesis

2.1 Tumor–Induced Angiogenesis

Tumor growth can be characterized as having three distinct stages: (1) avascular growth, (2) angiogenesis, and (3) vascular growth (Figure 2.1). Initially, tumor growth is avascular. The solid tumor mass develops as the cancer cells proliferate in the absence of a blood supply. In this phase, the tumor obtains nutrients, including oxygen and glucose, and exports its metabolic waste by diffusion transport processes alone. Since a tumor's mechanism for growth is a diffusion limited process, avascular tumors cannot grow indefinitely. The diffusion limit for oxygen is approximately 100 microns (μm). Thus, as the tumor increases in size, cells near the center of the tumor are beyond this diffusion limit and become oxygen starved. These cells become hypoxic and stop growing, a state known as quiescence. As the tumor continues to expand, the quiescent cells eventually become so oxygen deprived that they die, forming a necrotic core. Typically avascular tumors can only grow to approximately $1-2$ millimeters in diameter [107].

To ensure its sustained growth, a tumor must acquire a supply of nutrients and the ability to export metabolic waste. It does this by stimulating new blood vessel growth from nearby existing vasculature. This new vessel formation is called angio-

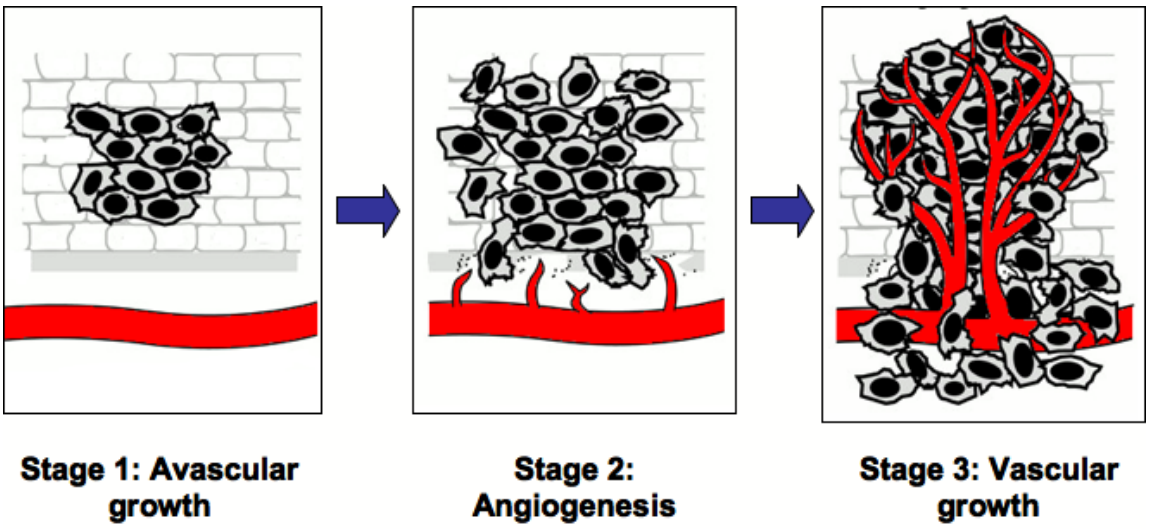

Figure 2.1: Depiction adapted from Zetter et al. [175] showing the three distinct phases of tumor growth. Angiogenesis is the bridge between avascular and vascular tumor growth, a potentially fatal stage of cancer.

genesis. Circulating endothelial precursors, shed from the vessel wall or mobilized from bone marrow can also contribute to tumor angiogenesis [10]. Another way tumor vascularization can occur is when tumor cells grow around an existing vessel forming a perivascular cuff [21]. Oxygen deprived tumor cells release a wide variety of polypeptide angiogenic factors that initiate new vessel growth [93]. These angiogenic factors diffuse through the surrounding tissue, setting up a chemical gradient between the tumor and any existing vasculature. Among these, members of the vascular endothelial growth factor (VEGF) and angiopoietin family have a prominent role [19]. Angiopoietins are involved in maintaining cell-cell contacts, inhibiting apoptosis, and promoting vessel maturation [126]. However, VEGF is the most well-characterized angiogenic factor critical for angiogenesis. When VEGF reaches the blood vessel, it triggers a cascade of events. Figure 2.2 illustrates the major VEGF mediated events that occur during early angiogenesis. Endothelial cells, which form the interior lining of blood vessels, have cell surface receptors specific to VEGF [40]. Endothelial

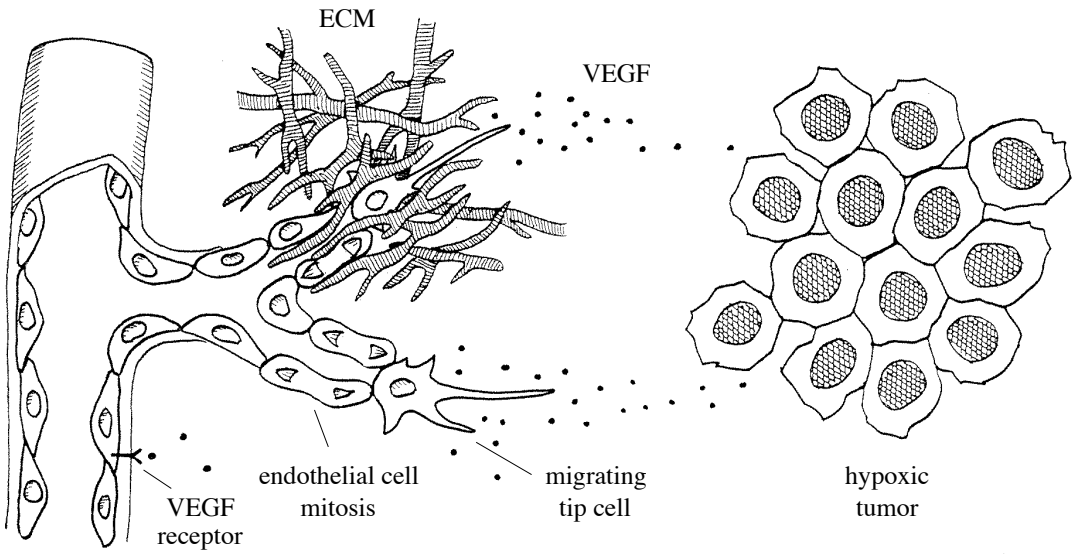

Figure 2.2: An illustration of early events in angiogenesis taken from Bauer et al. [12]: VEGF mediated endothelial cell activation and degradation of the basement membrane, subsequent migration and invasion into the tissue led by tip cells extending filopodia, cell division, and endothelial cell interaction with extracellular matrix fibers. This illustration emphasizes that the processes involved in angiogenesis are controlled at the level of individual cells. In this context, cellular dynamics are a discrete process and a cell-based model is a better description of cellular dynamics than continuous models, which deal solely with cell densities.

cells are activated via two high affinity VEGF receptors, VEGFR1 and VEGFR2. At the onset of angiogenesis, endothelial cell activation results in increased vascular permeability [129] and the production of proteases that locally degrade the basement membrane of the blood vessel [113, 69]. This breakdown of the basement membrane enables the endothelial cells to migrate into the extracellular matrix of the extravascular tissue, also referred to as the stroma. In order to reach the tumor, endothelial cells must navigate the complex structure of the extracellular matrix (ECM). The role of the ECM in sprout guidance is described in detail in Section 2.2. VEGF activated endothelial cells also upregulate additional cell surface receptors called integrins, which regulate cellular adhesion to matrix molecules [146]. To facilitate

their migration, endothelial cells have the ability to condition the ECM by producing a number of different proteolytic enzymes which degrade specific ECM proteins [113, 69]. Two such proteases are plasminogen activators and matrix metalloproteinases. Plasminogen activators are crucial for the degradation of fibronectin and laminin, whereas matrix metalloproteinases degrade collagen and elastin [113, 124]. As endothelial cells interact with the ECM, they can also cause the release of angiogenic factors that were bound to the ECM [107, 63, 91]. These newly liberated angiogenic factors are then available for endothelial cells to use to further coordinate their movement through the stroma [63, 91]. Considerable attention has been given to the role of growth factors, such as vascular endothelial growth factor (VEGF), in endothelial cell migration, survival, and proliferation.

There is substantial empirical evidence indicating that VEGF induces endothelial cell migration [150, 50, 172, 18]. One means of endothelial cell migration is by chemotaxis, which is directed motility toward positive chemical gradients. Using a Boyden chamber assay, Cao et al. showed that VEGF elicits a strong chemotactic response in human umbilical vein endothelial cells [18]. In an *in vitro* study of two populations of porcine aortic cells, one cell line expressing only VEGFR1 and the other only VEGFR2, Waltenberger et al. demonstrated that VEGFR2 was solely responsible for VEGF mediated chemotaxis [167]. Endothelial cell migration also occurs along positive gradients of cellular adhesion sites that are naturally present in the ECM [154], a process called haptotaxis. Endothelial cell degradation and production of collagen and fibronectin can create new or amplify existing local adhesive gradients, which also affects endothelial cell haptotaxis [56].

VEGF can regulate very different cellular responses resulting in phenotypically distinct populations of endothelial cells. Experiments of murine retinal angiogenesis

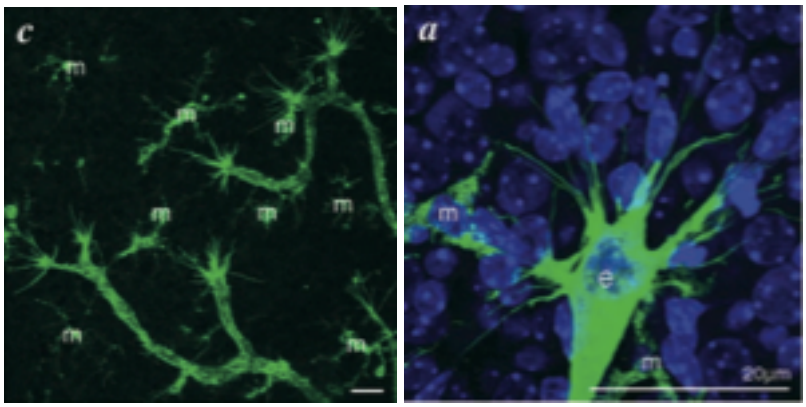

(a) (b)

Figure 2.3: High magnification confocal images showing phenotypically distinct tip cells during angiogenesis [50]. The endothelial cells at the tips of the vascular sprouts extend long filopodia. Scale bar = 20 μm.

show that the sprout tip consists of a single endothelial cell, which responds to VEGF solely by chemotaxis (no proliferation), and that VEGF induced proliferation occurs only in the cells comprising the sprout stalk [50]. Figure 2.3a is a confocal micrograph of VEGF induced angiogenesis demonstrating the distinctive morphology of vascular sprout tip cells. Figure 2.3b is a close-up of one of these tip cells. Evident in both images, the endothelial cells at the tips of the vascular sprouts extend long filopodia. The scale bars represent 20 μm. The mitogenicity of VEGF on endothelial cells is also well substantiated [128, 40, 150, 18]. From the experiments of Waltenberger et al. [167] described above, it is shown that VEGFR2 is the only receptor implicated in VEGF stimulated endothelial cell mitosis. During angiogenesis, endothelial cell proliferation provides the additional cells necessary for the sprout to grow and extend further into the stroma towards the tumor (see Figure 2.2) [54, 124, 151]. Branches develop when the sprout bifurcates and loops form when neighboring sprouts fuse together. This fusing of two vessels is a process called anastomosis. As the new sprout approaches the tumor, there is an increased incidence of sprout branching that is referred to as the brush border effect [116].

Newly formed capillary sprouts are initially immature [171]. Immature sprouts lack a basement membrane and are not yet capable of supporting blood flow [124]. For sprouts to mature, many other processes must first occur, including lumen and vacuole formation, the recruitment of specialized cells, and the construction of a basement membrane. Endothelial cells must abandon their invasive phenotype and reassociate with the ECM via cell surface integrins [107]. *In vitro* experiments of human endothelial cells in three dimensional collagen matrices show that vacuole and lumen formation depend on collagen-binding integrin $\alpha_2\beta_1$ [32]. These studies reveal that intracellular vacuoles enlarge and coalesce to create a luminal compartment. Endothelial cells further associate and develop lumens at sites of cell-cell contact, thereby generating tubular structures. Endothelial cells also recruit specialized cells called pericytes and smooth muscle cells. These cells contribute to vessel stability and maturation by inhibiting endothelial cell proliferation and promoting new basement membrane synthesis [59]. The result is a fully mature vessel capable of blood transport and thus nutrient delivery to the tumor.

Although these fundamental processes that occur during angiogenesis are well established, there is still considerable ambiguity and debate among researchers as to how biochemical and biomechanical mechanisms are coordinated to control vascular development. Recent efforts in experimental research have intensely focused on advancing understanding of these mechanisms in hopes of discovering novel anti-angiogenesis therapies. However, as new experimental assays capable of examining the cellular and molecular level dynamics during angiogenesis are developed, discordant data have been published. The following sections review some of the experimental observations that have given rise to dogma, and present conflicting empirical data that have generated confusion.

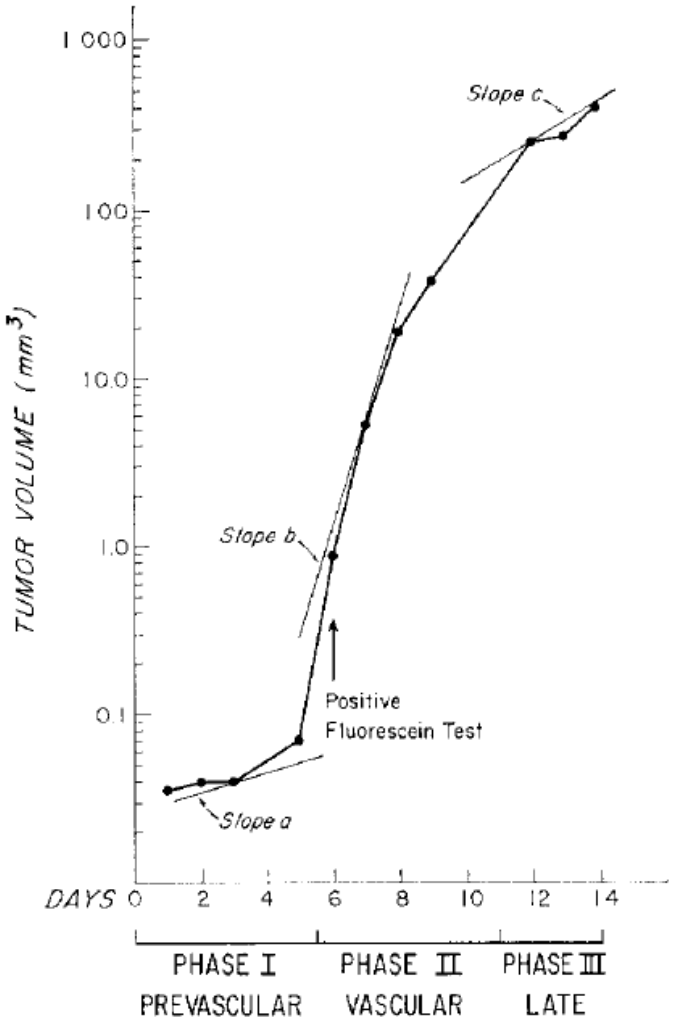

Figure 2.4: Plot of tumor volume for distinct phases of tumor growth in the rabbit cornea [52]. Rapid tumor expansion that occurs after vascularization is evident.

The vascular growth phase of tumor development occurs after the blood vessels reach the tumor (Figure 2.1). The newly acquired vasculature provides a direct source of oxygen and nutrients to the tumor and increases the tumor's capacity to export waste products, thereby allowing the tumor to sustain rapid continued growth unattainable by avascular tumors [52]. In Figure 2.4, tumor volume in mm^3 is measured over time and the prevascular and vascular phases of tumor growth are labeled [52]. This plot punctuates the rapid growth that ensues after tumor vascularization. Tumor vascularization has been closely linked to metastasis [41], which is the transmission of cancer cells distal to the original tumor. Often secondary tumors develop. Vascular growth and metastasis mark a progressive and potentially fatal stage of cancer. Angiogenesis, therefore, is the critical transition between the benign avascular stage of tumor growth and cancer. Because of its important role in cancer, understanding the processes involved in angiogenesis is an area of intense focus for experimental biologists and mathematical modelers, and provides the motivation for this dissertation.

2.2 The Dynamic Role of the Extracellular Matrix in Angiogenesis

The location of the tumor dictates the environment in which endothelial cells must survive and migrate. Depending on the tissue, the density of the matrix and the various other cells that make up the stroma can vary a great deal. It is widely accepted that cellular interactions with the ECM and the location of the tumor have a significant impact on new capillary sprout formation and morphology. Therefore understanding how the ECM modulates angiogenic processes has commanded considerable attention in experimental research. There is, however, speculation concerning the precise mechanisms involved and important questions are, as yet, unanswered.

What role does the ECM play in endothelial cell function? How are growth differentials between neighboring endothelial cells established? How is sprout branching initiated? And, can the composition of the stroma be manipulated to inhibit angiogenesis? A more in depth investigation of the role of the composition and structure of the stroma on capillary formation is needed and cell-based modeling provides a forum for such studies.

The extracellular matrix is a dynamic macromolecular structure that influences the interactions among cells and the organization of tissues. It is a major component of the extravascular tissue region, or stroma, and plays a central role not only in new blood vessel growth [34], but also in other morphogenic processes, including embryogenesis [29], tissue repair and wound healing [112], and cancer invasion [135]. The ECM is made up of fibrous proteins, collagen and elastin, specialized proteins, such as fibronectin and laminin, and chains of complex sugars [4]. It provides molecules for cellular adhesion to the matrix as well as mechanical support for cell migration and morphogenesis. A large body of research is concentrated on understanding how cell-ECM interactions impact and regulate morphogenic processes. Results from such investigations illuminate the active role of the ECM in transmitting biochemical signals and mechanical forces that can mediate cell survival, phenotype, shape, and orientation. This area continues to be a target of intense investigation.

2.2.1 ECM mediated changes in cell phenotype

Cells are equipped with and can upregulate transmembrane receptors that enable them to receive signals from and interact with their environment. Signaling proteins, including focal adhesion kinase, α-actinin, and vinculin, associate with the intracellular integrin domain to form a focal complex that binds to the cell's cytoskeleton [118]. Once assembled, a focal adhesion anchors the cell to the ECM, which is used by the

cell for movement. These focal adhesions are assembled and disassembled dynamically to facilitate cell migration. The presence of highly clustered focal adhesions are a hallmark of a migratory cell phenotype. Migratory guidance via focal adhesion binding sites in the ECM is a phenomenon referred to as contact guidance and plays a key role in guiding new vessel growth [160]. Contact guidance results in biased cellular motion in the direction of matrix fiber alignment. This differs from haptotaxis, which is another mechanism for directed cell motility whereby cells move in response to gradients of adhesion. The haptotactic response is to adhesive glycoproteins, such as fibronectin, found in the extracelluar matrix.

Experiments have linked the mechanical forces induced by cell attachment to the ECM via integrins to changes in a cell's internal molecular machinery [26]. Such tension-dependent alterations affect signal transduction pathways, cellular biochemistry, and changes in the cytoskeleton [26]. Experiments using human microvascular endothelial cells on substrates patterned with adhesive islands were performed to explore how the ECM influences cell shape and cellular function [25, 64]. In these experiments, cell shape was regulated by controlling the size and number of adhesive islands. Cells on adhesive islands that allow sufficient cell spreading successfully enter and progress through their growth cycle. As the size of the adhesive islands is reduced, cell spreading is limited and the cells enter a program of apoptosis. Even in the presence of saturating concentrations of growth factor, loss of anchorage to the ECM results in cell cycle cessation and apoptosis. These studies reveal the important relationship between cell shape and function and the role of the ECM as a key mediator.

2.2.2 Mechanical properties of the ECM

The physical properties of the ECM, such as density, heterogeneity, and stiffness, that affect cell behavior is also an area of current investigation. Type I collagen (collagen) is the most abundant protein in the extracellular matrix [90]. The collagen molecule is a triple helical protein approximately 300 nm long and 1.5 nm in diameter [90]. Due to its molecular sequence, collagen molecules have a tendency to form covalent bonds with each other and self-assemble into larger fibrils [90, 152]. Collagen fibrils also associate into larger bundles of matrix fibrils, referred to as fibers, that have been estimated to be between 100 and 1000 nm thick [44].

Matrigel^{TM} is a heterogenous gelatinous protein substrate manufactured to culture cells in *in vitro* experiments of angiogenesis. It is largely composed of collagen and laminin and contains growth factor concentrations, all of which provide an environment conducive to cell survival. It is a popular choice for observing angiogenesis because of its ability to stimulate complex cellular behaviors. In experiments of endothelial cells on Matrigel^{TM}, increasing the stiffness of this gel or disrupting the organization of the cellular cytoskeleton, inhibits the formation of vascular cell networks [165, 164]. It has also been shown that matrices with lower fiber density transfer more strain to the cell [130]. Cells respond to alterations in the mechanical properties of the ECM, for example, by upregulating their focal adhesions on stiffer substrates [37]. For anchorage-dependent cells, including endothelial cells, increasing the stiffness of the ECM therefore results in increased cell traction and slower migration speeds [37]. Moreover, experiments of endothelial cells cultured on collagen gels demonstrate that directional sprouting, called branching, is induced by collagen matrix tension [85]. Thus, via integrin receptors, the mechanical properties of the ECM influence cell-matrix interactions and modulate cell shape, cell migration speed, and

the formation of vascular networks.

Cells also have the ability to condition the ECM for invasion by producing proteolytic enzymes which degrade specific ECM proteins [117]. In addition, cells can synthesize ECM components, such as collagen and fibronectin [164, 86], and can further reorganize the ECM by the forces they exert on it during migration [164, 165, 130]. Collagen fibrils align in response to mechanical loading and cells reorient in the direction of the applied load [130]. Tractional forces exerted by vascular endothelial cells on Matrigel^{TM} cause cords or tracks of aligned fibers to form promoting cell elongation and motility [164]. Experimental studies of matrix remodeling demonstrate the importance of cell-matrix interactions in controlling cell migration, proliferation, and apoptosis and clarify the need for further investigation of the effects of local matrix structure on cell migration [25, 78]. As more experimental data is amassed, the ECM is emerging as the vital component to morphogenic processes.

Understanding how individual cells interpret biochemical and mechanical signals from the ECM is only part of the whole picture. Morphogenic processes also require multicellular coordination. In addition to the guidance cues cells receive from the ECM, they also receive signals from each other. During new vessel growth, cells adhere to each other through cell-cell junctions, called cadherins, and in order to migrate, cells must coordinate integrin mediated focal adhesions with these cell-cell bonds. This process is referred to as collective or cluster migration [45]. During collective migration, cell clusters often organize as two dimensional sheets [45]. The next section reviews relevant intracellular signal transduction pathways, the mechanism by which cells integrate and coordinate information from other cells, environmental growth factors, and the ECM.

2.3 Intracellular Signal Transduction Pathways in Angiogenesis

The cellular processes that occur during tumor angiogenesis are tightly coordinated and regulated by signaling molecules, such as tumor secreted growth factors. Signaling molecules activate endothelial cell surface receptors and initiate intracellular signaling cascades. Intracellular signaling leads to gene transcription, the production of enzymes and angiogenic factors, increased cell survival, migration, and proliferation [58]. We know that endothelial cell binding of VEGF induces proliferation, cell migration, and the expression of proteases that degrade the ECM, but this is an oversimplification that neglects the role of different VEGF isoforms, other signaling molecules present in the ECM, and the various types of cell surface receptors.

Signal transduction is the mechanism through which cells translate molecular stimuli to activate intracellular response mechanisms. This process usually involves a rapid, ordered sequence of biochemical reactions inside the cell. These biochemical reactions occur on the order of milliseconds during ion flux, and up to minutes for the activation of protein mediated kinase cascades. Signal transduction is part of a complex communication system responsible for regulating fundamental cellular activities, including metabolism, protein synthesis, division, migration, and survival. The capacity of cells to perceive and precisely respond to their environment forms the basis for development, tissue repair, immunity, and normal tissue homeostasis [14].

Cells are equipped with a class of proteins called cell surface receptors that act as sensory detectors and signal transducers that enable the cell to respond to external stimuli. There are different types of receptors which are classified according to their function and by the molecules they bind. Transmembrane receptors are one type of cell surface receptor and are so called because they bind, or ligate, extracellular

molecules stimulating a biochemical response across the cell membrane to activate internal signaling cascades. Examples of transmembrane receptors include receptor tyrosine kinases (RTK), integrins, toll-like receptors, and G protein-coupled receptors. Another class of receptors are intracellular receptors, which are located inside the cell and are further divided into cytoplasmic receptors and nuclear receptors. Located in the cell nucleus, nuclear receptors are activated by hormones and can bind to DNA to regulate gene expression and protein production. Nuclear receptors are also called transcription factors. Cytoplasmic receptors, as their name suggests, are located in the cell cytoplasm and are a general class of receptor that binds soluble ligands in the cytoplasm. Steroid hormone receptors in the cytoplasm are one example.

One aim of this dissertation is to investigate the mechanisms by which, in response to VEGF and other signaling molecules, an endothelial cell decides to migrate versus proliferate and how vascular development is subsequently effected. Because of their importance in regulating key events during angiogenesis, we focus on three specific transmembrane receptors: VEGF specific RTK receptors, integrin receptors, and vascular endothelial (VE) cadherins.

2.3.1 The VEGF receptors

Although there is a large body of experimental literature describing the behavior of endothelial cells in response to VEGF binding different VEGF specific receptors on the cell's surface [20, 39, 50, 66, 46], the mechanisms by which an endothelial cell can respond differently to what seems to be the same chemical signal are still unclear. VEGF is an endothelial cell specific protein which has several isoforms generated by alternative exon splicing. $VEGF_{121}$, $VEGF_{165}$, $VEGF_{189}$, and $VEGF_{206}$ are four common forms. $VEGF_{121}$ is a freely diffusible protein produced by tumor

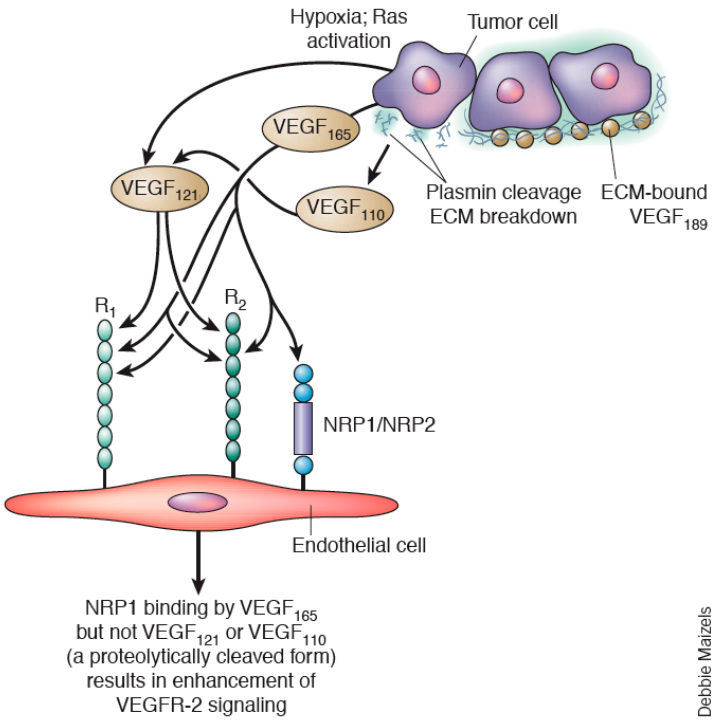

Figure 2.5: A depiction of the various tumor-secreted and matrix bound VEGF isoforms and their interaction with endothelial cell receptors (VEGFR1, VEGFR2, NRP1/NRP2) [39]. It is still unclear how receptor-VEGF ligation transmits different signals to regulate endothelial cell behavior.

cells, whereas $VEGF_{189}$, and $VEGF_{206}$ are predominantly bound to and sequestered in the ECM. The most common isoform is $VEGF_{165}$. $VEGF_{165}$ is also secreted by hypoxic tumor cells, but it is unique in that it is a diffusible protein that can also bind to the ECM. Matrix bound VEGF may be released when tumor or endothelial cells proteolytically cleave ECM molecules. VEGF released in this way generates a diffusible and viable form of VEGF locally available for use by endothelial cells [107, 63].

As shown in Figure 2.5, endothelial cells are activated via two receptor tyrosine kinases, fms-like tyrosine kinase-1 and fetal liver kinase-1, which are often referred to as VEGFR1 and VEGFR2, respectively [171]. VEGF binds to these receptors triggering intracellular signaling pathways. One example is the VEGF-Bcl2-CXCL8

signaling pathway, which mediates pro-angiogenic and pro-survival phenotypes in endothelial cells [120]. VEGFR2 is considered to be the main signaling receptor for endothelial cells. Neuropilin (NRP1 and NRP2) are $VEGF_{165}$ isoform specific receptors that enhance the binding of $VEGF_{165}$ to VEGFR2 and $VEGF_{165}$ mediated chemotaxis [39]. The possibility that NRP acts as a co-receptor to VEGFR2 is proposed as a possible explanation for the greater mitogenic potency of $VEGF_{165}$ relative to $VEGF_{121}$ [39]. There is evidence that VEGFR1 may act as a decoy receptor since it binds VEGF but does not induce a mitogenic signal. It may also act to suppress VEGFR2 signaling by competing for available VEGF [107].

2.3.2 Integrin receptors

Integrins are transmembrane receptors that promote the adhesion of cells to extracellular molecules. They are crucial components for signal transduction from the ECM. There are many different types of integrins and many cells have multiple types on their surface. Integrin binding to the ECM regulates the expression of cyclin-dependent kinases and activation of the MAPK signal transduction pathway, which control cell cycle progression and growth [64]. Integrins are one such receptor family and are stimulated by binding to the various proteins of the ECM [137, 108]. Integrins are heterodimers composed of α and β subunits. Each subunit has a large extracellular domain, a transmembrane segment, and two smaller cytoplasmic tails [144]. Integrin receptors mediate transmembrane signal transduction via "inside-out" and "outside-in" signaling. Biochemical signals originating within the cell can affect integrin-ligand binding affinity (inside-out) and consequently modulate cellular adhesion to the matrix. For example, intracellular signaling and adaptor proteins, such as α-actinin, vinculin, and focal adhesion kinase ($pp125^{FAK}$), associate with the cytoplasmic integrin domain forming an integrin-activating complex or focal ad-

hesion complex [118, 144]. This activating complex induces spatial changes in the cytoplasmic tails, which in turn, alters the configuration of the extracellular domain and the binding affinity of the integrin receptor. Endothelial cells attach directly to the collagen fibers in the ECM through the $\alpha 1\beta 1$ and $\alpha 1\beta 2$ integrin receptors [152]. Intracellular signaling pathways are then initiated that influence cell survival, growth, and that regulate the actin cytoskeleton necessary for cell motility (outside-in) [25, 34].

2.3.3 Vascular endothelial (VE)–cadherins

Cells must adhere to each other to form cohesive multicellular structures and tissues. In particular, to maintain a tight barrier between the blood in the blood vessel and the extracellular space, endothelial cells must secure tight junctions with each other. The mechanism for such adherence in endothelial cells is through transmembrane receptors called VE-cadherins. The VE-cadherin transmembrane receptor is endothelial cell specific. Inside the cell, these receptors can associate with the protein β-catenin to regulate cadherin binding to the cell's actin cytoskeleton [98]. Externally, cadherins form homodimers with the cadherin proteins present on adjacent cells, connecting the actin cytoskeltons of neighboring cells and thereby providing a mechanism for intercellular communication.

2.3.4 Receptor cross-talk

During signal transduction, signaling molecules are not always specific to a single transduction pathway. Often these signaling components are shared between different pathways. For example, signals originating from an integrin receptor can influence the signals received from growth factor ligation to the VEGF receptors. This phenomenon is referred to as cross-talk. Figure 2.6 is a picture of the focal ad-

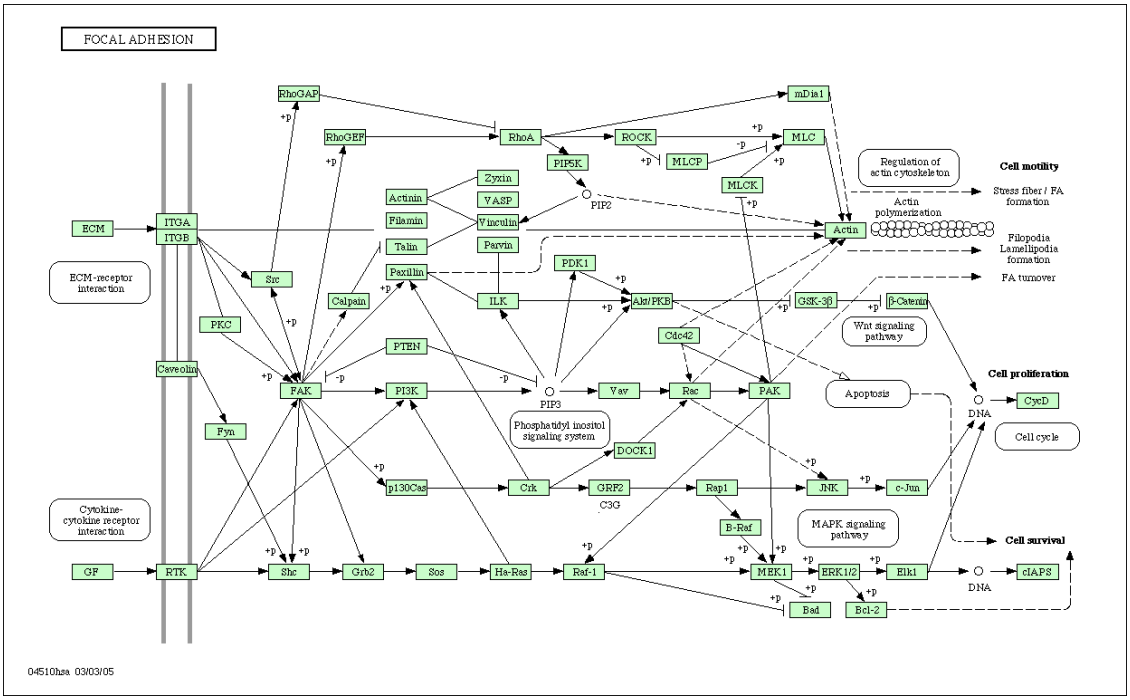

Figure 2.6: An example of cross-talk between different signaling pathways (adapted from KEGG Pathway Database [122]).

hesion signaling network taken from the KEGG Pathway Database [122] and shows some of the cross-talk between growth factor and integrin receptors. This database synthesizes a vast amount of disjoint information taken from multitudes of different experimental laboratories using different cell lines to produce such signaling pathways. These types of networks should be viewed only as a starting point or a road map to direct further research.

During angiogenesis, the growth factor, integrin, and cadherin signaling pathways are highly connected and provide regulatory feedback to each other [47]. For example, in response to VEGF, endothelial cells upregulate the expression of integrin receptors [107]. Hutchings et al. 2003 [66] found that integrins can additionally serve as receptors for immobilized $VEGF_{165}$ and $VEGF_{189}$ present in the ECM. Through the RTK receptor, VEGF activates the MAPK signal transduction pathway that

stimulates proliferation and cell survival. It has also been demonstrated, however, that cell survival and proliferation critically depend on adherence to the matrix, since even in the presence of saturating concentrations of growth factor, loss of anchorage to the ECM results in cell cycle cessation and apoptosis [25, 64]. Another example of receptor cross-talk in angiogenesis occurs through cadherin activation. Cadherins bind to actin, which is an important structural and signaling molecule for cytoskeleton reorganization. Therefore cadherin receptors not only facilitate cell-cell communication but also influence motility. Moreover, there is evidence that cadherins also induce signals that mitigate growth factor activation and repress cell proliferation [173]. This process is called contact inhibition. The coupled signals from growth factor, integrin, and cadherin receptors are interpreted by the cell to determine cell phenotype and dynamically regulate angiogenic processes [147].

2.4 Historical Milestones in the Angiogenesis Field

Angiogenesis has been an active field of research for many decades. The term angiogenesis was first coined in 1787 to describe new blood vessel growth. In 1971, Judah Folkman, the pioneer and grandfather of angiogenesis research, hypothesized that tumor growth is angiogenesis dependent. His hypothesis was the impetus for focus research on tumor-induced angiogenesis and the discovery of the mechanisms controlling new blood vessel growth. To present a broad overview of the progression of the experimental advances in angiogenesis research, some historical highlights are summarized below [67].

- 1787 - British surgeon Dr. John Hunter first uses the term angiogenesis to describe blood vessels growing in the reindeer antler
- 1971 - Surgeon Dr. Judah Folkman hypothesizes that tumor growth is depen-

dent upon angiogenesis. His theory, published in the New England Journal of Medicine, is initially regarded as heresy by leading physicians and scientists.

- 1989 - One of the most important angiogenic factors, VEGF, is discovered by Dr. Napoleone Ferrara and Dr. Jean Plouet. VEGF turns out to be identical to a molecule called Vascular Permeability Factor discovered in 1983 by Dr. Harold Dvorak.

- 1992 - The first clinical trial of an anti-angiogenic drug (TNP-470) begins in cancer patients.

- 1997 - First angiogenesis stimulating drug (becaplermin, Regranex) is FDA approved for treatment of diabetic foot ulcers.

- 1997 - Dr. Michael O'Reilly publishes a research finding in the journal Nature showing complete regression of cancerous tumors following repeated cycles of anti-angiogenic therapy using angiostatin and endostatin.

- 1999 - Massive wave of anti-angiogenic drugs in clinical trials: 46 anti-angiogenic drugs for cancer patients; 5 drugs for macular degeneration; 1 drug for diabetic retinopathy; 4 drugs for psoriasis.

- 1999 - Wave of pro-angiogenesis drugs in clinical trials: 5 drugs for coronary artery disease; 5 drugs for peripheral vascular disease; 1 drug for stroke; 10 drugs for wound healing.

- 1999 - Laboratory research, led by Dr. Robert Kerbel and Dr. Judah Folkman, shows that some traditional cytotoxic chemotherapies may inhibit tumor angiogenesis when administered at low-doses.

- 1999 - Dr. Richard Klausner, Director of the U.S. National Cancer Institute, designates the development of antiangiogenic therapies for cancer as a national priority.

- 2003 - The monoclonal antibody drug Avastin (Bevacizumab) becomes the first anti-angiogenic drug shown in large-scale clinical trials to inhibit tumor blood vessel growth and to prolong survival in cancer patients.

The field of angioigenesis continues to be an area of intense research. New anti-angiogenetic drugs are being developed and are in various stages of clinical testing. In addition, experimental and theoretical researchers continue to actively search for promising, new therapeutic targets in hopes that we may gain control of angiogenesis and contain or cure cancer. Although cancer provides compelling motivation for further research in and resource allocation to the study of angiogensis, the control of angiogenesis has important implications to other physiological processes, including embyrogenesis, arteriogenesis and wound healing. In addition, understanding the mechanisms that regulate new blood vessel growth may lead to new insights for advancing both pro- and anti-angiotherapies critical to the treatment of diabetic retinopathy, macular degeneration, psoriasis, rheumatoid arthritis, heart attack and stroke.

CHAPTER III

Modeling Angiogenesis Mathematically

A major challenge is to integrate the vast amount of basic science information available and relevant to angiogenesis to advance understanding of the system as a whole. This challenge is even more onerous due to the fact that this information is generated by a number of different research groups, each focusing on a small piece of the puzzle. The result is disjoint and compartmentalized data at multiple scales and hierarchies: from gene transcription and protein synthesis, to cellular response and dynamics, to tissue and organ level organization. Mathematical models and computational simulation can be used as translational tools to synthesize these research results into a unified whole.

3.1 Modeling Biological Systems Mathematically

Differential equation models describe deterministic relationships of continuously changing quantities. Ordinary differential equation (ODE) models, which involve a single independent variable, are often employed as a starting point to describe biological systems. One of the advantages of using ODEs is that much is known about their behavior. ODE models are simple and elegant and generally require fewer parameters than their spatial counterparts (agent-based models or partial differential equations). This is an important consideration when experimental data are obtained

from a well-mixed compartment where spatial information is lacking, for example in the blood, or from a tissue homogenate, such as the spleen or lymph node. When sufficiently simple, ODEs have the added benefit of being analytically tractable, and techniques such as those employed in bifurcation theory can be used to predict parameter values that switch a system from one steady state to another. However, using ODE models assumes that the populations they describe are homogeneous and uniformly distributed over the simulation space for all time. This is an assumption that may not be biologically realistic, and that may significantly influence the resulting dynamics. The assumption can be wholly mitigated by employing partial differential equation (PDE) models. PDEs are used to describe systems whose dynamics depend on multiple independent variables. Most physical processes are functions of several independent variables, distributed in multiple dimensions, or in both space and time. However, as the ODEs and PDEs become more complicated, they are more computationally challenging and the advantages to using differential equation models diminish.

An alternative to differential equation models are agent-based or individual-based models. Agent-based models (ABMs) are used to describe populations of interacting agents, such as insects and people, using simple rules that dictate their behaviors. Agent actions are asynchronous, that is, they do not evolve at constant time steps. Instead, agents respond dynamically and independently to changing environmental or discrete event cues. From a simple set of rules, ABMs can exhibit highly complex and emergent phenomena. As experimental assays are developed that increase understanding of biological systems, the level of description needed for realistic and relevant models becomes increasingly more complex. Thankfully, the expanding computational ability of computers make possible the use of ABMs for more complex

systems. As a result ABMs are quickly gaining in popularity [145, 62, 176]. Moreover, because ABM implementation is achieved at the agent level, the description of the agents and rules tends to mimic the language used to describe the real system, that is, the description is more physical in character than mathematical. For example, models using differential equations consider rates of creation, rates of death, rates of binding, rates of diffusion for whole populations of agents, whereas an ABM considers the rules guiding the actions of the agent: will it bind this cell, will it move towards that cell? The familiar and natural modeling language used in agent based models not only makes ABMs approachable and useful to experimentalists and clinicians, but also engages them in the modeling process.

3.2 The Role of Agent Based Models in Multi-Scale Systems

Bridging multiple scales is a formidable modeling challenge. Because agent-based models are constructed by considering the behaviors of individual system components and can be developed for each biological subsystem or hierarchy, they are also naturally well suited for linking these different models together. For example, merging ABMs focusing on different biological scales has been used to translate the results of and facilitate collaboration between experimentalists working on various aspects of the acute inflammatory response [7]. In this work, a group of agent based models were developed to simulate intracellular signal transduction pathways that were then incorporated into ABMs for different cell types. Subsequently, these cellular models were integrated to simulate tissue and whole organ function during the acute inflammatory response.

Another modeling technique that has emerged in response to the computational challenge presented by multiple scales integrates differential equation models with

ABMs to couple the dynamics occurring on different time and length scales [125, 2, 75, 12, 82, 176]. This technique has been applied to the development of models describing tumor growth, a complex biological system with important clinical applications [2, 75, 176]. In Jiang et al. [75], a three-dimensional model of avascular tumor growth was developed that spans three distinct scales. A lattice Monte Carlo model is used to describe tumor cell growth, adhesion, and viability. These cell dynamics are regulated at the intracellular level by a Boolean network for protein expression that controls the cell cycle. At the extracellular level, nutrients, metabolic waste, and growth factor and inhibitory chemical concentrations are described by a system of reaction diffusion equations. Growth curve measurements and measurements of the size of the proliferating rim and necrotic core regions from simulated tumors agree with the quantitative results generated from tumor spheroid experiments. This model predicts what environmental conditions tumor cells require for survival, and the molecular weight of potential growth promoters and inhibitors regulating tumor cell viability. As demonstrated by these results, validated models of biological systems can be used for prediction and to guide future experimental pursuits.

Because of the expense of *in vivo* and *in vitro* experimentation, mathematical modeling and simulation are becoming important and critical research tools. For quantitative results, all modeling approaches rely on accurate parameter estimation. Without parameter values based on experimental data, models may provide qualitative information, but not necessarily quantitative results. This is a difficult aspect of modeling that often requires interpretation and/or interpolation of experimental data to obtain accurate parameter values. Models need to be calibrated and researchers should confirm that their parameter values are within physically relevant ranges. Consequently, it is useful to perform a sensitivity analysis in order to

identify key parameters and to understand the effect of parameter uncertainty and variability on the observed outcomes. In addition, every effort possible should be made to quantitatively validate model results with independent experiments or with reports in the literature, using different data than those that were used for model calibration. Model validation ensures that the model correctly reflects the workings of the biological process or system and provides a better understanding of the models capabilities, limitations, and appropriateness for addressing a range of important questions. Validation is an essential step towards developing a predictive model. Finally, and perhaps most importantly, modelers should strive to make experimentally verifiable predictions. Validated models provide a framework for formulating and testing hypotheses, may offer new perspectives or interpretations of existing results, and may suggest or guide future experiments.

3.3 Existing Mathematical Models of Angiogenesis

A great number of factors must be tightly coordinated to promote tumor-induced angiogenesis. No single model has yet incorporated every aspect of every process involved in sprouting angiogenesis, nor is this level of complexity necessary for a model to be useful or predictive. Focused investigations on particular mechanisms and processes advance the development of a number of angiogenesis models. For instance, Levine et al. models growth factor mediated protease production, incorporating an important biochemical mechanism for ECM degradation and regulation of endothelial cell proliferation [95, 96]. Cell receptor level treatment of this critical biochemical pathway derived from first principle Michaelis-Menten chemical kinetics is a significant contribution to angiogenesis models. Other advances in angiogenesis modeling are being achieved at a more macroscopic level. The development of a dy-

namic adaptive tumor-induced angiogenesis model took into account hemodynamic forces, such as shear stress and variable blood viscosity, in the dynamic remodeling of vascular architecture [109]. These and other existing mathematical models offer many insights into the processes driving angiogenesis and highlight necessary conditions for angiogenesis to occur, such as endothelial cell proliferation, haptotaxis, and chemotaxis [8, 155], by concentrating on very specific mechanisms influencing capillary sprout development.

Mathematical investigations of tumor-related angiogenesis have employed discrete, continuous, and mechanical models to describe a variety of dynamics believed to affect angiogenesis. Continuum models, that is, models that use differential equations, rely on the principles of mass conservation and chemical kinetics and, in contrast to discrete models, allow for the investigation of aggregate behavior without having to keep track of individual cells. In one dimension, these models can produce important averaged quantities, such as blood vessel, endothelial cell sprout and tip densities, and capillary network expansion rates. However, one-dimensional models are unable to capture information about the form and structure of the developing capillary network. Two-dimensional models, while providing a more realistic description of the capillary networks formed during angiogenesis, fall short of producing hallmark network behavior, such as repeated sprout branching. In two and three dimensions however, continuum model predictions can be compared to qualitative data obtained from in vitro and in vivo experiments. One disadvantage, of course, is that the detailed morphological features of individual cells cannot be studied within a continuum framework.

The discrete analogue of continuous models are models in which cellular behaviors, such as growth and motility, occur according to a predefined set of rules. These

models have the advantage of being computationally fast and efficient, but their greatest advantage is that they allow the motion and behavior of individual cells to be studied. As a result, discrete models are especially useful for generating more realistic capillary structures by incorporating rules for sprout branching and anastomosis, and may lead to insights about endothelial cell movement and capillary structures not offered by other types of models [155, 9]. One disadvantage however, is that assigning rules or probabilities to events may "artificially" generate some phenomena; for example, the branching in Anderson and Chaplain 1998 [9] is not an inherently emergent phenomenon, but a prescribed one. More realistic capillary morphology has been attained in two dimensions, but these models, have been unable to reproduce branching and the brush border effect without artificial rules [9, 158]. Most models of angiogenesis largely neglect the dynamic interaction between endothelial cells and the extracellular matrix. Until very recently, models only considered haptotaxis, a key interaction between endothelial cells and the ECM through fibronectin [9, 95]. Even at this simple level of description, the capillary networks generated by numerical simulations agree well with the morphology of capillary networks observed *in vivo*. These results strongly suggest that cell-matrix interactions cannot be ignored if a predictive model of tumor-induced angiogenesis is to be achieved.

There are also mechanical models of angiogenesis that emphasize physical forces, such as cell traction and motility, to generate vascular networks [105]. At the macroscopic level, mechanical models have been used to describe the macroscopic changes in vessel wall structure and vascular tree formation as a result of changes in blood pressure and vessel wall stress [109]. At the molecular level, mechanical models have been employed to study the mechanisms by which forces applied to endothelial cells alter gene expression and the effects on the signaling pathways. Another variation

of mechanical modeling of angiogenesis attempts to capture the key interactions between the mechanical forces generated by the cell and the ECM. Murray and his co-authors have shown that a purely mechanical theory is capable of predicting patterned networks of endothelial cells similar to those observed *in vitro* [106]. Holmes and Sleeman [61], combine this approach with a model proposed by Chaplain, and develop a mechano-chemical model of tumor-induced angiogenesis. This model is the first attempt to reconcile the mechanical and chemical aspects of angiogenesis. However, this model neglects to address ECM degradation, and a cell-biased diffusion tensor is included arbitrarily rather than derived from first principles. There are a few successful efforts to model vascular networks by focusing on the mechanical properties of the ECM, such as elasticity and stiffness [115, 106]. In Manoussaki 2003 [105], a model incorporating both chemical and mechanical forces, specifically endothelial cell traction on a viscoelastic ECM, produces network structures that resemble cellular network structures observed in *in vitro* experiments. However, this work only considers tractile forces in a continuum model framework geared towards vasculogenesis and does not fully investigate the role of chemotaxis and sprouting vessels in tumor-induced angiogenesis. Another leading effort in tumor-induced angiogenesis modeling is described in Sun et al. 2005 [158]. In this model, the anisotropy and heterogeneity of the ECM is explicitly treated and the model captures the dendritic structure of capillary network formation. However, sprout branching still only occurs as a result of imposed rules. A new branch is generated when both the age of the sprout is above some prescribed age and the variation of the tip velocity transverse to the existing sprout orientation is greater than a certain threshold value. Although the structure of the ECM is incorporated into their model, direct endothelial cell-matrix interactions are not, and consequently, the model is unable to capture the

individual cell dynamics that allow cells to respond differently according to their specific local microenvironment.

3.4 Cell-Based Modeling Approach to Simulate Angiogenesis

Mathematical modeling and experimental observations provide convincing evidence that both mechanical and chemical processes may govern tumor-induced angiogenesis, and that interactions between tumor cells and endothelial cells within the host environment cannot be ignored. While significant progress has been made toward a complete model of tumor-induced angiogenesis, there is still much work to be done in developing a model that (i) couples multiple time and length scales, (ii) generates realistic capillary structures including branching and anastomoses without *a priori* prescribing rules and probabilities to these events, and (iii) considers the complex chemical and mechanical interactions that occur between endothelial cells and the ECM.

A cell-based model is a type of ABM, where the agents are individual biological cells. However, in contrast to an ABM where an agent is represented by a single point on a lattice, a cell in a cell-based model occupies many lattice sites. This type of representation preserves the unique identity and behavior of each cell, properties that make ABMs powerful. In addition, a cell-based model characterizes and captures dynamic changes in a cell's size and shape. Figure 2.2 emphasizes that the processes involved in angiogenesis happen at the level of individual cells. Because the typical sprout is only a few endothelial cells long and one to two cells wide, a cell-based model provides a better description of the cellular dynamics during early angiogenesis than continuum models, which deal with cell densities. In addition, discrete and continuum models of angiogenesis that model sprout tip cells or cell

densities are predicated on the fact that the tip cell governs the motion of the entire capillary sprout. These models assume that the rest of the cells in the capillary sprout are inactive. However, the endothelial cells in the sprout dynamically contribute to vascular structure through the forces of cellular adhesion, cell signaling, and the local restructuring of the ECM [102]. To reproduce realistic vascular networks, these models must assign probabilities to rules for branching [8, 9, 155, 109]. A cell-based model is able to account for individual cell interactions with and influence on their local environment. Consequently, cell specific biochemical and biomechanical dynamics are easily incorporated. A cell-based model also has the capacity to simulate emergent dynamics or structures, for example sprout branching. Another advantage to cell-based modeling is that adding another scale to the system, for example by incorporating intracellular signaling as was done in Jiang et al. [75], is a relatively straightforward extension. As discussed earlier in the context of agent-based models, a cell-based model of angiogenesis can assist in our understanding and synthesis of the large amounts of existing composite empirical data.

CHAPTER IV

First Cell-Based Model of Tumor-Induced Angiogenesis

4.1 Model Architecture

The processes involved in angiogenesis naturally suggest a three tier time and length scale architecture. At the extracellular level, angiogenic factors diffuse through the stroma. At the cellular level, cellular dynamics include interactions between cells and cell interaction with the ECM. At the intracellular level, signal transduction pathways within each cell control cell behavior. In this chapter, we develop a cell-based model structured in terms of these multiple scales by modeling the extracellular and intercellular environments. This cell-based model is a hybrid model, that is, it utilizes the advantages of both discrete and continuous modeling. At the extracellular level, a partial differential equation describes diffusion, uptake, and half-life decay of tumor-secreted VEGF. Cellular level dynamics are captured using a discrete lattice Monte Carlo model (the cellular Potts model) that considers cell migration, growth, proliferation, cellular adhesion, and extracellular matrix degradation. The extra- and intercellular environments are integrated and directly impact each other. In Chapter VIII, an intracellular level is added to capture signaling pathways that control cell cycle and other signaling dependent decisions that occur inside the cells.

4.2 Model Domain and Geometry

We initiate the simulations with a single endothelial cell that has degraded the basement membrane of the primary blood vessel, which lies adjacent to the left hand boundary. Adjacent to the right hand boundary rests a mature avascular tumor that delivers VEGF to the stroma. Figure 4.1 shows the initial configuration and geometry of the domain. Using a two dimensional domain provides a first approximation to capillary sprout formation *in vivo* and allows us to compare our results with both experimental models on planar substrates (e.g., [174, 91, 138]) and other two dimensional computational models [9, 155, 158]. Our model has the flexibility to examine capillary sprout development at different length scales. The avascular cornea of the rodent eye is a classical angiogenesis assay, which allows the process of neovascularization to occur over long distances (1−2 mm) in a normally avascular tissue [11, 116]. However, tumors that form in other tissues, for example in the lung, brain, stomach, and breast, are much closer to the existing vasculature. Our interest is on individual cell interactions during early sprouting angiogenesis. Sprout initiation and branching have been shown to occur over distances ranging from 20 to 100 μm [79, 91]. Therefore, in our model, the distance between the parent blood vessel and the tumor is approximately 165 μm. This distance is slightly larger than the diffusion limit for oxygen ($\sim$100 μm). We choose this length scale so that we can focus on cell-cell and cell-matrix interactions, to replicate the hypoxic conditions that may arise *in vivo*, and to allow sufficient space for the new sprouts to grow 100 μm without encountering an artificial boundary.

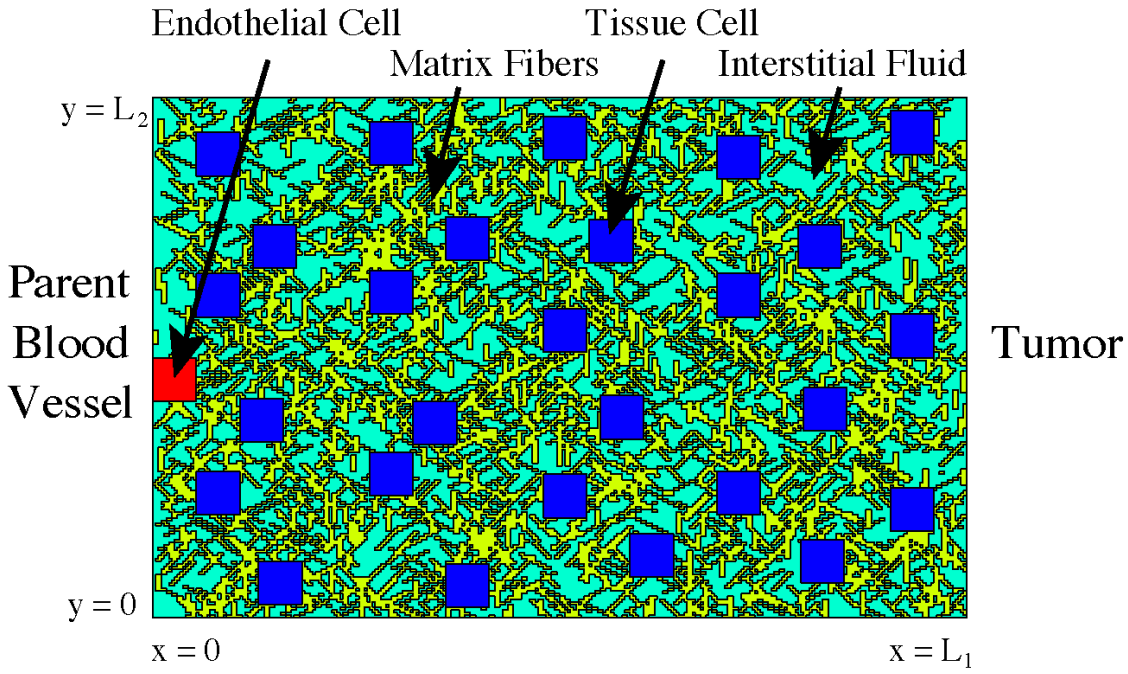

Figure 4.1: The geometry of the initial domain. An endothelial cell bud (red) grows into the tissue from a parent blood vessel adjacent to the left boundary; an avascular tumor resides adjacent to the right hand side of the domain and supplies VEGF to the stroma. The space between represents the stroma and is composed of extracellular matrix fibers (yellow), tissue specific cells (dark blue) and interstitial fluid (light blue).

4.3 Extracellular Dynamics (VEGF)

The evolution of VEGF sets up a chemical gradient between the tumor and the parent blood vessel and constitutes the extracellular environment to which the endothelial cells respond. VEGF is secreted by the tumor and diffuses through the stroma where it decays at a constant rate and is also taken up by endothelial cells. Mathematically, the spatial profile of VEGF satisfies a partial differential equation of the form

$$\frac{\partial V}{\partial t} = D\nabla^2 V - \lambda V - B(x, y, V) \tag{4.1}$$

where $V = V(x, y, t)$ denotes VEGF concentration. The coefficient of diffusivity for VEGF in tissue, $D > 0$, is assumed to be homogeneous throughout the simulation domain. The rate VEGF decays, $\lambda > 0$, is also assumed to be constant, and $B(x, y, V)$ is a function describing endothelial cell binding and uptake of VEGF.

The maximum amount of VEGF that can be bound and internalized by an endothelial cell per unit of time is denoted by β. To compute β, we consider the number of VEGF receptors per endothelial cell and the rate at which VEGF-receptor complexes can be internalized and surface receptors recycled. Vascular endothelial cells express both VEGFR1 and VEGFR2. While VEGFR2 is VEGF specific, VEGFR1 is not and can bind adhesion molecules and other growth factors [20]. In our calculation of β, we use the total number of VEGFR1 and VEGFR2 receptors for a human colon microvascular endothelial cell (311,200) [168, 46]. However, in the model, we do not consider multiple VEGF isoforms or growth factors, or the explicit binding of adhesion molecules, both of which compete for available binding sites and may reduce the amount of VEGF an endothelial cell can bind. That being said, it is difficult to ascertain whether β provides an over or underestimate of endothelial cell

VEGF uptake *in vivo* because VEGF activated endothelial cells upregulate the number of VEGF receptors they express. Moreover, the actual number of endothelial cell VEGF receptors depends on cell size, tissue of origin, and vessel size [46]. We use an instantaneous VEGF-receptor complex internalization rate of 4.3 x 10^{-4} per second, and 45 kDa as the molecular weight for VEGF_{165} [40, 20]. The value of β is computed in the following manner. The maximum amount of VEGF that can be bound per endothelial cell, $\beta_{\max}$, is given by

$$\begin{aligned}\beta_{\max} &= \text{molecular weight of } \text{VEGF}_{165} * \#\text{ VEGF receptors} \\ &= 7.47225 * 10^{-8} * 311,200 \\ &= 0.02325 \text{ pg/cell}\end{aligned}$$

and the endothelial cell VEGF uptake per MCS due to receptor recycling, β_r, is

$$\begin{aligned}\beta_r &= \text{VEGF rate of receptor recycling} * \beta_{\max} \\ &= I * \beta_{\max} \\ &= 1.548 * 0.02325 \\ &= 0.1293 \text{ pg/cell/hr} .\end{aligned}$$

The total amount of VEGF an endothelial cell can bind in an hour is

$$\beta = \beta_{\max} + \beta_r = 0.02325 + 0.1293 = 0.06 \text{ pg/cell/hr}$$

Receptor binding occurs very rapidly compared to the timescale of endothelial cell migration and proliferation. Thus, we assume that an endothelial cell instantly binds an amount of VEGF equal to the lesser of available chemical concentration V or the maximum amount that can be bound to endothelial cell surface receptors and

internalized, β. This function is given by

$$B(x,y,V) = \begin{cases} \beta, & \text{if } \beta \leq V \text{ and } \{(x,y) \subset \text{endothelial cell}\}; \\ V, & \text{if } 0 \leq V < \beta \text{ and } \{(x,y) \subset \text{endothelial cell}\}\ ; \\ 0, & \text{if } \{(x,y) \not\subset \text{endothelial cell}\}. \end{cases}$$

Initially, there is no VEGF in the stroma. The amount of VEGF supplied to the right hand boundary of the domain was estimated by assuming that in response to a hypoxic environment, quiescent tumor cells secrete a constant amount of VEGF and that VEGF decays at a constant rate. It is reasonable to assume that the concentration of VEGF within the tumor has reached a steady state and therefore that a constant amount of VEGF, denoted S, is available at the boundary of the tumor. To determine S, we calculate the amount of VEGF secreted by a hypoxic tumor cell, s, in picograms (pg) and multiply this by an estimate for the number of hypoxic cells in a mature avascular tumor. So,

$$\begin{aligned} s &= 624.3 \text{ pg}/10^6\text{cells} \\ &= 6.243 * 10^{-4} \text{ pg/cell} \end{aligned}$$

and therefore

$$\begin{aligned} S &= s * \#\text{ hypoxic tumor cells secreting VEGF/boundary lattice sites} \\ &= 6.243 * 10^{-4} * 10,724/L_1 \\ &= 6.695/L_1 \text{ pg/boundary lattice site} \end{aligned}$$

VEGF secretion rates for hypoxic human cancer cells are taken from experimental data [93] and the number of hypoxic cells secreting VEGF is estimated based on the total number of quiescent cells in an avascular tumor as measured in Jiang et al. [75], where cell quiescence occurs as a result of hypoxic conditions. At a distance of

165 μm and given that a mature avascular tumor grows to approximately 1−2 mm in diameter [107], the supply of VEGF from the tumor is approximated by a line source. Accordingly, the following initial and boundary conditions are used:

$$V(x, y, 0) = 0,$$

$$V(0, y, t) = 0, \quad V(L_1, y, t) = S, \quad V(x, 0, t) = V(x, L_2, t)\,.$$

These initial and boundary conditions for VEGF have frequently been employed in previous models of tumor-induced angiogenesis [9, 22, 23]. A dimensional analysis indicates that the concentration of VEGF in the stroma will also very quickly reach a steady state profile due to rapid diffusion (see Section 4.9). Numerical computations confirm this. Consequently, the steady state solution is a good approximation to Eq. 4.1 and we use the steady state VEGF profile as an initial condition for the discrete model as was similarly done in Stokes and Lauffenburger [155] and in Anderson and Chaplain [9].

4.4 Modeling the Stroma and Extracellular Matrix

The explicit modeling of the stroma and the extracellular matrix fibers is a novel feature of this model. The stroma is composed of matrix fibers, interstitial fluid, and tissue specific cells creating an inhomogenous composition and structure. We include tissue cells in our model to mimic a more anatomically accurate extracellular environment for the growing and migrating endothelial cells. The properties associated with these cells are tissue specific and depend on the particular biological processes being studied. For example, specialized cells, such as mast cells, fibroblasts, macrophages, or pericytes, could be modeled to capture the effects of other guidance cues on sprout formation or to examine their roles in sprout maturation and stability. Our current focus is to study how the composition of the stroma affects sprout morphology and

migration, and therefore, at this stage a "general" tissue cell is modeled to provide an additional level of structure to the stroma. We assume that tissue cells are roughly the same size as an endothelial cell [4], are immobile, and are more difficult to invade than matrix fibers and interstitial fluid. Consequently, tissue cells compete for space and create intercellular pressure on and resistance to the migrating and proliferating endothelial cells. Matrix fibers comprise approximately 37% of the stroma and the architecture of the ECM is anisotropic, with regions of varying densities [4]. A single collagen fibril is approximately 300 nm long and 1.5 nm wide and is substantially smaller than an endothelial cell, which is approximately 10 μm in diameter [4]. Thus, to model the mesh-like anisotropic structure of the ECM, we assume that many individual collagen fibrils and other matrix proteins are bound together constituting larger cords or bundles of matrix fibers that have been estimated to be between 100 and 1000 nm thick [44]. We randomly distributed 1.1 μm thick fiber bundles at randomly chosen discrete orientations ranging from 0 to 180 degrees until 37% of the stroma was occupied. The left picture of Figure 4.2 shows the heterogeneity and random distribution of Type I collagen and the right picture shows that the model representation of the matrix fibers captures this structure.

4.5 Cellular Potts Model for Cellular Dynamics

The processes involved in new capillary formation occur at the level of individual cells. Accordingly, we use the cellular Potts model to capture the interactions between endothelial cells or between an endothelial cell and the stroma (matrix fibers, tissue cells and interstitial fluid). The cellular Potts model is a discrete lattice Monte Carlo model developed by Glazier and Graner and is based on an energy minimization principle [53]. The cellular Potts model has already been used to model

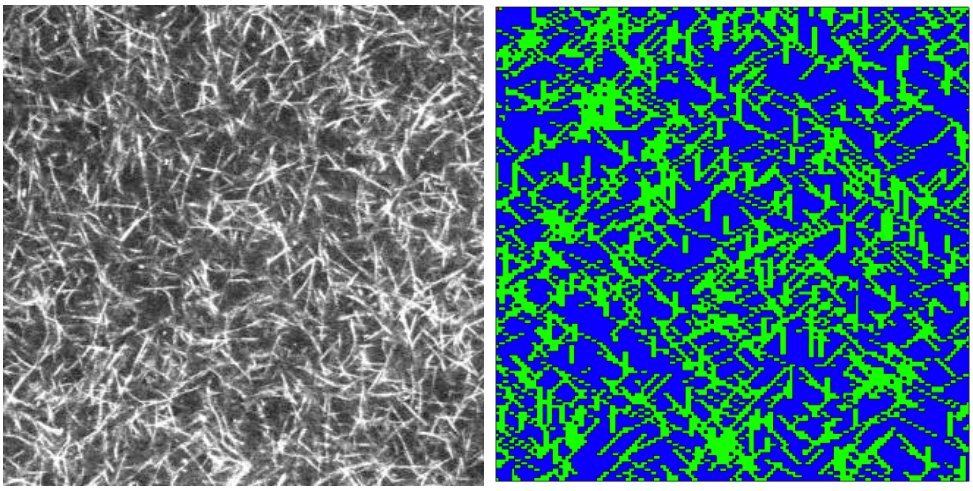

Figure 4.2: Left: Magnification of Type I collagen fibers. Right: Model representation of heterogeneity and random distribution of ECM fibers of constant width.

a multitude of biological phenomena including differential adhesion-driven cell rearrangement [53], cellular differentiation and growth of tissues [60], fruiting body formation of *Dictyostelium* [74], avascular tumor growth [75], cancer invasion [161], and vasculogenesis [111, 110].

In this dissertation, we extend the cellular Potts model to simulate tumor-induced angiogenesis. Our work is distinct from that presented in Merks et al. [111, 110], which models the reorganization of randomly dispersed cells into a vascular network pattern, simulating *in vitro* vasculogenesis. In contrast, our work focuses on the processes that generate the sprouting of new capillaries from a pre-existing vasculature *in vivo* (angiogenesis). Moreover, our model considers cell growth and division, dynamics that are not modeled in Merks et al. [111, 110] and we explicitly model the ECM, a component critical to vascular formation.

The cellular Potts model partitions the computational domain into endothelial cells, matrix fibers, tissue cells and interstitial fluid which are situated on a lattice and are denoted by type $\tau = \{\text{e, m, t, f}\}$ respectively. To account for individual

cells, each cell is further associated with a unique identifying number, denoted by σ, that is assigned to every lattice site occupied by that entity (see Figure 2 in JIang et al. [74] for an example). Matrix fibers and interstitial fluid are collectively identified by 1 and 0 respectively. Under this framework, each entity has a finite volume, a deformable shape, and competes for space. Intercellular interactions occur only at the cell's surface and have a cell type dependent surface (or adhesion) energy given by $J_{\tau,\tau'}$, which is a measure of the coupling strength between the entities τ and τ'. Cellular dynamics are characterized by an equation for total energy given by

$$E = \sum_{sites} J_{\tau,\tau'} \left(1 - \delta_{\sigma,\sigma'}\right) + \sum_{cells} \gamma_\tau \left(a_\sigma - A_\sigma^T\right)^2 . \tag{4.2}$$

The first term in Eq. 4.2 is the contribution to total energy resulting from cell adhesion at cell surfaces. The second term takes into account the fact that cell growth and deformation require energy, where a_σ denotes cell σ's current volume and A_σ^T is a designated "target" volume. We assume that the target volume of an endothelial cell undergoing mitosis is the volume that it would grow to in the absence of external forces and given sufficient nutrition and is designated as twice its initial volume.

Additionally, we know that VEGF acts as a chemoattractant for endothelial cells [172]. The effective energy required for chemotaxis, $\Delta E_{\text{Chemotaxis}}$, can be derived as follows: In our model, cell movement is governed by energy gradients and, over time, cells move to reduce the total energy of the system. Empirical evidence indicates that VEGF concentration gradients induce endothelial cells to move in the direction of increasing concentration with a velocity proportional to the VEGF gradient. Because the cells must move through the highly viscous ECM, their motion is overdamped and the force required for motion is proportional to velocity, $\vec{F}_{\text{Chemotaxis}} \propto \vec{v}$. Consequently, the force is proportional to the chemical gradient. We can construct

an effective chemotaxis potential that is proportional to the local chemical gradient:

$$\Delta E_{\text{Chemotaxis}} = \mu_\sigma \left[V(\vec{x}) - V(\vec{x}\,') \right].$$

The parameter $\mu_\sigma < 0$ is the effective chemical potential, which influences the strength of chemotaxis relative to other parameters in the model. $\vec{x}\,'$ and $\vec{x}$ represent the two neighboring lattice sites randomly selected during one trial update in a Monte Carlo step and are described in detail below.

The cellular Potts model evolves in time using repeated probabilistic updates of unique cell identification numbers, σ, on the lattice. One update occurs as follows: a lattice site, $\vec{x}$, is selected at random and assigned the σ from one of its unlike second nearest neighbors, $\vec{x}\,'$, which has also been randomly selected. The total energy of the system is computed before and after σ is changed. If the total energy of the system is reduced as a result of this change, the update is accepted. If the change in *sigma* increases the energy of the system, we accept the update with a Boltzmann probability. Thus the probability of accepting an update is given by

$$P_{\text{acceptance}} = \begin{cases} 1, & \text{if } \Delta E < 0; \\ e^{-\Delta E/kT}, & \text{if } \Delta E \geq 0, \end{cases}$$

where ΔE is the change in total energy of the system as a result of the update, k is the Boltzmann constant and T is the effective temperature that corresponds to the amplitude of cell membrane fluctuations. This probability influences the likelihood of energetically unfavorable events taking place [161]. A total of n proposed updates, where n is the number of sites on the lattice, constitutes one Monte Carlo step (MCS) and is the unit of time used in the model.

In the model, endothelial cells will move to promote stronger over weaker adhesive bonds, shorter over longer cell boundaries, and toward regions of higher chemical

concentrations. Only endothelial cells are allowed to grow, move and invade; ECM, tissue specific cells and interstitial fluid do not grow or actively invade each other or endothelial cells. Endothelial cells interact both mechanically and biochemically with the ECM. Effective mechanical forces exerted on the ECM by endothelial cells as they migrate are incorporated as a result of the matrix fibers' resistance to compression given by γ_m. Biochemical interactions include VEGF binding to, uptake by, and activation of endothelial cells, endothelial cell matrix degradation, and the chemical bonds between endothelial cells and between endothelial cells and matrix fibers, which are designated by J_{ee} and J_{em}, respectively. Haptotaxis is naturally incorporated through this adhesion term whenever an endothelial cell interacts with a matrix fiber. The endothelial cells also interact with the tissue cells via surface adhesion and competition for space. In addition, each endothelial cell carries its own internal cell clock, which is used to determine where the cell is in its mitotic cycle and whether or not cell division can occur. The endothelial cell cycle is not explicitly modeled, but this model can be modified to incorporate intracellular signaling cascades regulating the cell cycle and cell cycle dependent events as was done by Jiang et. al. [75] in their multi-scale model of avascular tumor growth. Cell division occurs when a proliferating cell has doubled in size and has gone through one complete cell cycle, which we take to be 18 hours [170]. Cell division produces two daughter cells; one daughter cell keeps the cell ID of the parent and the other is assigned its own unique ID. Because endothelial cells demonstrate an increased rate of survival in the presence of VEGF [48], endothelial cell death is not considered in the model.

This model also distinguishes between tip and stalk cell phenotypes [50]. A tip cell is defined as the leading endothelial cell and when activated by VEGF, the tip cell migrates chemotactically using the matrix fibers for support. The tip cell is also

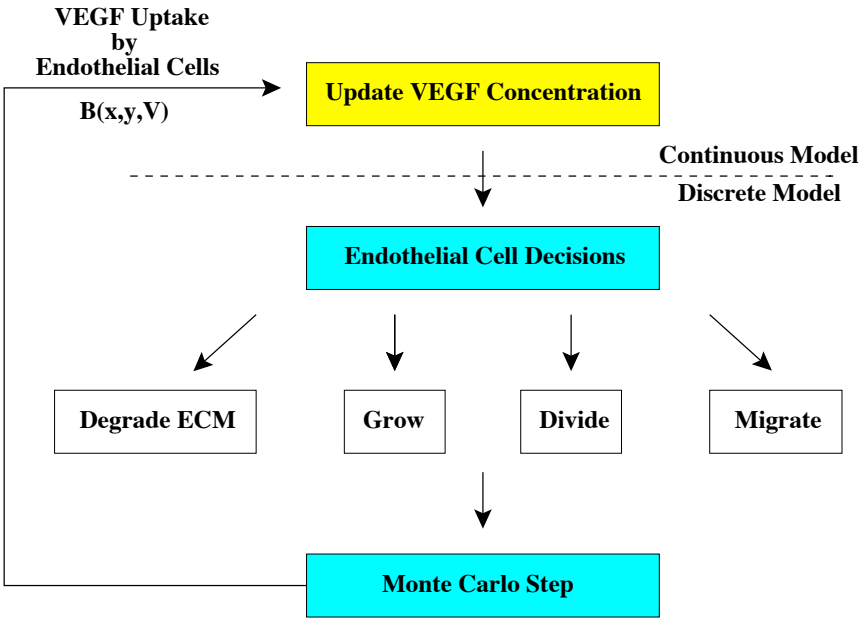

Figure 4.3: A schematic that shows the interface between the discrete and the continuous models. The continuous model for VEGF and the discrete model of cellular dynamics are used as initial conditions for each other at every time step to produce a coupled system of extra- and intercellular dynamics.

capable of degrading the matrix fibers thereby establishing local adhesion gradients and further promoting its migration through the stroma [154, 56]. Proliferation occurs behind the tip cell [124, 151] and this phenomenon is captured by allowing those stalk cells to proliferate. In the model, if the cell is proliferating, it does not move chemotactically [11, 124, 50] and vice versa. The remaining stalk cells, as long as they are VEGF activated, only move in response to cell-cell and cell-matrix adhesion, and through random membrane fluctuation.

4.6 Hybridization: Interfacing the Discrete & Continuous Models

The continuous model describing the VEGF profile and the discrete model of cellular dynamics are used as initial conditions for each other at every time step to produce a coupled system of extra- and inter-cellular dynamics. At time zero, the steady state solution to Eq. 4.1 provides the initial VEGF profile used in the discrete

cellular model. Within the discrete model, each endothelial cell uniquely responds to the amount of VEGF present by deciding whether there is sufficient VEGF to become activated. VEGF must be present in quantities above a threshold level, v_a, for endothelial cell activation to occur. Once activated, each individual endothelial cell decides whether it is a tip cell and will migrate and degrade the ECM, or if it is a proliferating cell, and will grow and divide. After the discrete model evolves through one Monte Carlo step in time, the function for endothelial cell VEGF uptake and binding, $B(x, y, V)$, is re-derived based on the new distribution of endothelial cells on the lattice. A new spatial profile for VEGF at the next time step is obtained by solving Eq. 4.3 using the updated function $B(x, y, V)$. The lattice is then updated with the new VEGF profile. As the continuum and discrete models feedback on each other, each endothelial cell responds to its evolving microenvironment.

4.7 Parameters

Whenever possible, we take parameters from experimental data. A list of all parameter values used in this model is provided in Table 4.1, including references. If no reference is given, the parameter is a relative value chosen to recapitulate observed phenomenological behaviors. By equating the time it takes an endothelial cell to divide during the simulation with the endothelial cell cycle duration of 18 hours, Monte Carlo steps are calibrated to real time units. In the simulations, 1 Monte Carlo step is equivalent to 1 hour.

The value for endothelial cell activation v_a is based on our numerical solutions to Eq. 4.1 and is chosen to activate the initial endothelial cell. A smaller relative value for $J_{\tau,\tau'}$ establishes a stronger cell surface bond. Endothelial cells will bind more tightly to each other than they will with other constituent types, whereas interstitial

fluid has very little binding affinity. The membrane elasticities, γ_τ, are chosen to reflect the relative compressibility of the constituent. A larger value makes it more difficult for a constituent to deviate from its target volume and consequently more difficult to invade. Interstitial fluid is relatively easy to invade compared to the tissue specific cells. The chemotactic potential, μ_σ, is chosen so that its contribution to total energy is on average equal to the contribution to total energy due to cell growth.

Table 4.1: Table of Parameters. Dimensions are given in terms of L=length, T=time, M=mass and E=energy. For instance, the adhesion terms have dimensions of energy per unit length of cell membrane. An asterisk designates a parameter that varies across numerical experiments; all other parameters are held fixed. The exact parameter values used in a simulation are given in the discussion corresponding to that experiment. Unless otherwise noted, all simulations used the same parameter set, initial configuration of matrix fibers and tissue cell distribution, and follow the assumptions described in the previous section. EC denotes endothelial cell.

Parameter	Symbol	Dimensions	Model Value
VEGF Diffusion	D	L^2/T	$3.6x10^{-4}$ cm^2/h [148]
VEGF Decay	λ	T^{-1}	.6498 h^{-1} [148]
VEGF Uptake	β	M/cell/T	.06 pg/EC/hr [20, 46, 168]
VEGF Source	S	M/L	.035 pg/pixel [93, 75]
Activation Threshold	v_a	M	.0001 pg
Proliferation Threshold	v_p	M	.005 pg
Adhesion			
EC−EC	J_{ee}	E/L	1
EC−Fluid	J_{ef}	E/L	32
EC−Matrix	J_{em}	E/L	16
EC−Tissue	J_{et}	E/L	31
Fluid−Fluid	J_{ff}	E/L	35
Fluid−Matrix	J_{fm}	E/L	35
Fluid−Tissue	J_{ft}	E/L	32
Matrix−Matrix	J_{mm}	E/L	5
Matrix−Tissue	J_{mt}	E/L	30
Tissue−Tissue	J_{tt}	E/L	2
Membrane Elasticty			
*EC**	γ_e	E/L^4	1.0
Matrix	γ_m	E/L^4	0.4
Fluid	γ_f	E/L^4	0.1
*Tissue Cell**	γ_t	E/L^4	1.2
Chemotaxis*	μ	E/conc	$-1.5x10^5$
Boltzmann Temperature	kT	E	.01

4.8 Discussion

There are a great many number of factors and dynamics at play during angiogenesis. In this model, we do not attempt to introduce every dynamic known to influence angiogenesis. A primary aim of this dissertation is to understand the roles of cell-cell and cell-matrix interactions on angiogenesis. We therefore focus our investigations on those specific cell-cell and cell-matrix dynamics that occur at the very onset of angiogenesis. We incorporate several key biochemical dynamics: (i) VEGF binding to, internalization, and recycling of endothelial cell surface receptors, (ii) VEGF mediated cellular activation, migration, and proliferation, and (iii) proteolytic extracellular matrix degradation.

This model constitutes the first cell-based model of tumor-induced angiogenesis. This model is distinct from previous models of tumor-induced angiogenesis in several ways. First, this model captures single cell biochemical and biomechanical dynamics allowing individual cells to interact with and influence their local environment. Second, the stroma is explicitly modeled, including structural variations, such as the anisotropy of the matrix fiber distribution, and tissue specific cells. Third, a distinction is made between sprout tip and stalk cells and the unique behavior each cell phenotype exhibits is incorporated into the model. Finally, this model is capable of simulating capillary sprout branching and anastomosis, which are larger scale structures that emerge only as a result of the featured cellular and molecular level dynamics; no rules specifically incorporating branching or anastomosis are imposed.

4.9 Dimensional Analysis of VEGF Dynamics

In two dimensions, the PDE describing VEGF dynamics is given by

$$\frac{\partial V}{\partial t} = D\left(\frac{\partial^2 V}{\partial x^2} + \frac{\partial^2 V}{\partial y^2}\right) - \lambda V - B(x,y)\,.$$

Nondimensionalizing, we introduce the following scalings

$$\widetilde{V} = \frac{V}{V_0}\,, \quad \tilde{t} = \frac{t}{t_0}\,, \quad \tilde{x} = \frac{x}{x_0}\,, \quad \tilde{y} = \frac{y}{x_0}\,, \quad \widetilde{B} = \frac{B}{B_0}$$

where $V_0, t_0, x_0, B_0 \neq 0$. Calculating the derivatives we find that

$$\begin{aligned}
\frac{\partial V}{\partial t} &= \frac{V_0}{t_0}\,\frac{\partial \widetilde{V}}{\partial \tilde{t}} \\
\frac{\partial^2 V}{\partial x^2} &= \frac{V_0}{x_0^2}\,\frac{\partial^2 \widetilde{V}}{\partial \tilde{x}^2} \\
\frac{\partial^2 V}{\partial y^2} &= \frac{V_0}{x_0^2}\,\frac{\partial^2 \widetilde{V}}{\partial \tilde{y}^2}\,.
\end{aligned}$$

Substituting into the PDE we obtain

$$\frac{V_0}{t_0}\,\frac{\partial \widetilde{V}}{\partial \tilde{t}} = \frac{DV_0}{x_0^2}\left(\frac{\partial^2 \widetilde{V}}{\partial \tilde{x}^2} + \frac{\partial^2 \widetilde{V}}{\partial \tilde{y}^2}\right) - \lambda V_0\,\widetilde{V} - B_0\widetilde{B}.$$

Dividing by $DV_0/x_0^2 \neq 0$ and simplifying, we get

$$\frac{x_0^2}{Dt_0}\,\frac{\partial \widetilde{V}}{\partial \tilde{t}} = \left(\frac{\partial^2 \widetilde{V}}{\partial \tilde{x}^2} + \frac{\partial^2 \widetilde{V}}{\partial \tilde{y}^2}\right) - \frac{x_0^2\lambda}{D}\,\widetilde{V} - \frac{B_0 x_0^2}{DV_0}\,\widetilde{B}.$$

Choosing

$$B_0 = \frac{DV_0}{x_0^2},$$

the terms describing diffusion and cell binding of VEGF are both $\mathcal{O}(1)$ and we obtain

$$\frac{x_0^2}{Dt_0}\,\frac{\partial \widetilde{V}}{\partial \tilde{t}} = \Delta\widetilde{V} - \frac{x_0^2\lambda}{D}\,\widetilde{V} - \widetilde{B}.$$

From the literature, we obtain the following experimental values for our parameters

$$D = 10^{-7}\ \mathrm{cm^2 s^{-1}} \quad \text{and} \quad \lambda = 0.65\ \mathrm{h^{-1}}.$$

If we choose the characteristic time scale to be equal to one Monte Carlo step and the characteristic length scale to be on the order of 1 pixel, we have

$$t_0 = 1 \text{ min} \quad \text{and} \quad x_0^2 = \frac{\pi 5^2}{16^2} = 0.3066 \ \mu\text{m}^2.$$

Now, we want to show that

$$\frac{x_0^2}{Dt_0} \ll 1.$$

Calculating, we find the following values for the nondimensional parameters

$$\frac{x_0^2}{Dt_0} = \frac{0.3066 \ \mu\text{m}^2 * 10^{-8} \frac{\text{cm}^2}{\mu\text{m}^2}}{10^{-7} \frac{\text{cm}^2}{\text{sec}} * 60 \frac{\text{sec}}{\text{min}} * 1\text{min}} \approx 0.00051$$

and

$$\frac{x_0^2 \lambda}{D} = \frac{3.066 * 10^{-9}\text{cm}^2 * \frac{0.65}{\text{hr}}}{10^{-7} \frac{\text{cm}^2}{\text{sec}} * 3600 \frac{\text{sec}}{\text{hr}}} \approx 5.5 * 10^{-6}$$

Here $\frac{x_0^2}{Dt_0} \ll 1$ and $\frac{x_0^2 \lambda}{D} \ll 1$ and therefore we can use the solution to

$$0 = \Delta \widetilde{V} - \widetilde{B}$$

to approximate the VEGF field in our model.

4.10 ANGIO – Simulation Software Developed in Python

The implementation of this theoretical model is a program called ANGIO. ANGIO uses more than 2000 lines of Python code, a high-level open source programming language, to simulate angiogenesis. To use ANGIO, a number of freely available Python modules must be installed. Specifically, the proper functioning of ANGIO relies on Python, PyLab, NumPy, SciPy, Matplotlib, and ScientificPython. In addition, IPython, an interactive shell for the Python programming language, aids in de-bugging and real-time simulation visualization and analysis. ANGIO is designed

to run locally, at the University of Michigan, or at Los Alamos National Laboratory. At a command prompt, typing `'> python ANGIO.py'` requires the user to specify where ANGIO is being run. This determines from what directory input files are read and to which directory the output data files are written. This program also has the built-in flexibility to specify the size of the computational domain at run-time and the user is prompted to provide this information. Cell type specific parameters, including adhesion and compressibility properties, and the number of Monte Carlo steps need to be modified within ANGIO in a function called ANGIO.parameters(). One advantage to using Python is that changes in the input files or the actual program code do not require the user to recompile the program. During the simulation, ANGIO solves the PDE describing VEGF dynamics, uses this as an input for cellular decision making, runs the Metropolis algorithm for the cellular dynamics, which then feeds back into the PDE as an input parameter. At each time step, ANGIO writes data files for the VEGF concentration, the distribution of endothelial cells, the composition of the stroma, cell properties, and data arrays identifying tip, proliferating, migrating, quiescent, and apoptotic cells. On the Mathematical Modeling and Analysis Group server at Los Alamos National Laboratory, a 900 MCS simulation takes approximately 1 hour.

4.10.1 Fourier transform solutions to the PDE

ANGIO makes use of Python's scientific computing libraries and packages to solve the partial differential equation describing the spatio-temporal profile of VEGF at each MCS. ANGIO.RDEsolve() solves the non-dimensional quasi-steady state reaction diffusion equation in two dimensions

$$\left(\frac{\partial^2 V}{\partial x^2} + \frac{\partial^2 V}{\partial y^2}\right) = \lambda V + B(x, y, V)\,. \tag{4.3}$$

The inputs into ANGIO.RDEsolve() are the size of the domain (x, y), the MCS we wish to solve for, the profile for endothelial cell consumption of VEGF, $B(x, y, V)$ the function for endothelial cell VEGF binding from the cellular model, and whether the source of VEGF from the tumor boundary is a line source, a point source, or parabolic. This function employs fast Fourier transforms to efficiently solve this parabolic partial differential equation and returns the new spatial profile for VEGF at the next time step.

4.10.2 Visualization techniques

ANGIO also has the built-in functionality for visualizing the simulation data. There are two functions that provide different quality two dimensional images: ANGIO.quikplot() and ANGIO.plotit(). ANGIO.quikplot() is exactly what it sounds like, it is a plotting function designed to create a sequence of *.png files for quick visualization and result interpretation. This function takes a directory path as an input and uses the pylab.matshow() command to produce an image using the standard jet colormap. It does not create publication ready images. On the other hand, ANGIO.plotit() uses a custom colormap developed specifically for these simulations of angiogenesis, which colors endothelial cells red, tissue cells dark blue, matrix fibers yellow, and interstitial fluid light blue. ANGIO.getcm() can save the images in multiple formats (png, jpg, etc.) at a specific resolution (dpi) and is appropriate for images intended for publication.

Another visualization technique we use to render publication quality images is a software program called MayaVi. MayaVi is a free visualization platform written in Python that uses the visualization toolkit (vtk) for its graphics. MayaVi has a GUI interface and can be imported and manipulated within Python. Using MayaVi does however require some data pre-processing. In particular, vtk files have to be

written for use in MayaVi. Once this is done, MayaVi is an extremely powerful graphical imaging solution and can be easily automated to handle large numbers of files. MayaVi generated all the final simulation images in this dissertation.

CHAPTER V

Cell-Based Model Exhibits Emergent Phenomena: Branching and Anastomosis

5.1 Using Simulation as an Investigative Tool

Although the fundamental processes that occur during angiogenesis are well established, there is still considerable ambiguity and debate regarding how biochemical and biomechanical mechanisms are coordinated to control vascular development. Recent efforts in experimental research have intensely focused on advancing our understanding of these mechanisms in hopes of discovering novel anti-angiogenesis therapies. However, as new experimental assays capable of examining the cellular and molecular level dynamics during angiogenesis are developed, discordant data have been published. Below we review some of the experimental observations which have generated confusion and given rise to dogma. We then formulate specific hypotheses and test these with our computational model.

A common perception has been that a freely soluble form of VEGF is solely responsible for both the activation and the differentiation of function seen in endothelial cells during tumor-induced angiogenesis. This belief, however, is being revised as experiments demonstrate that sequential activation of various endothelial cell surface receptors by multiple ligands are required for angiogenesis. Experiments show that the same VEGF receptor (VEGFR2) is responsible for mediating very dif-

ferent cellular functions, including endothelial cell growth, mitogenesis, migration, and increased survival [167, 39]. Some studies propose that the outcome of VEGFR2 signaling depends on the particular VEGF isoform present [39, 50]. The effects of different VEGF isoforms on vascular structure have been examined and significantly different capillary morphologies were observed in the presence of matrix bound versus soluble VEGF [91]. To further complicate matters, other investigations show that local growth differentials can exist even in areas saturated with soluble angiogenic factor [64].

There is convincing experimental evidence that endothelial cell proliferation is a necessary process for tumor vascularization [151]. It is generally believed that during angiogenesis, proliferation occurs right behind the tip cell and only after the endothelial cells have already migrated into the stroma some distance [151, 124]. Presently, however, discrepancies persist concerning the precise location of the proliferating cells during angiogenesis. Experimental models report mitotic activity occurring at the base of a newly formed sprout [79, 124], some distance behind the sprout tip [124, 65], localized immediately behind the sprout tip cell [124, 151] and at the tip [11, 138]. Another area where contradictory experimental data exist is whether proliferation and migration are mutually exclusive events. Some studies demonstrate that endothelial cell migration is a process separate and independent from proliferation, that is, an endothelial cell will either migrate or proliferate, but not both [11, 50]. More recent empirical evidence suggests that a proliferating cell is also capable of migrating [79, 138]. Remarkably, both proliferation and migration are mediated by VEGF. Although the exact mechanism is still unclear, the activation of VEGFR2 is interpreted differently by capillary tip cells that migrate versus stalk cells (cells behind the leading plexus) that proliferate [50]. There is evidence that tip cells

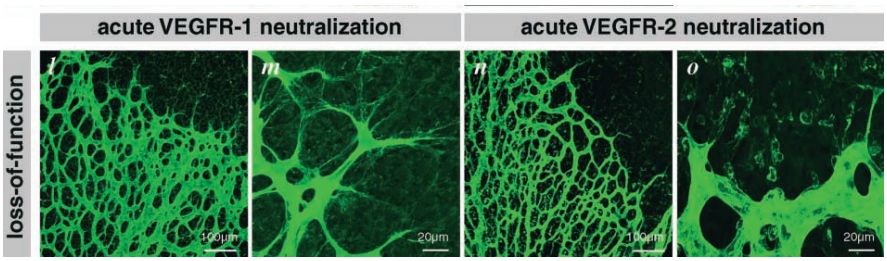

Figure 5.1: Neutralization of VEGFR2 (n & o) but not VEGFR1 (l & m) leads to retraction of tip cell filopodia [50].

and stalk cells have distinctly different gene expression profiles [50]. Tip cells can be distinguished from stalk cells by their proliferative quiescence, their prominent expression of VEGFR2 mRNA, and by the existence of filopodia. These filopodia, which can be as long as 100 μm, sense chemical gradients and guide endothelial cell migration [50]. The existence of filopodia on sprout tip cells indicates a migratory phenotype. *In situ* experiments suggest that VEGFR2 is most strongly expressed in tip cells and that VEGFR2 mediated signaling is necessary for tip cell filopodia extension (Figure 5.1) [50]. These studies also show that VEGF expression is strongest near the sprout tip and very low behind the sprout tip [50]. The work of Ruhrberg et al. [134] suggests that filopodia in conjunction with ECM bound VEGF plays an important role in the capillary sprout branching observed in angiogenesis. Despite convincing experimental evidence that growing vascular sprouts have specialized tip structures, differentiation between tip cells and stalk cells has received very little attention in models of vascular development.

Our presentation of and discussion on conflicting experimental data suggest the following research hypotheses:

H1: The presence of matrix bound and soluble VEGF results in different vascular morphologies.

H2: The location of the proliferating region of cells has an impact on capillary morphology and the rate of capillary sprout extension.

H3: The composition of the stroma, such as ECM density and the presence of other tissue cells, influences endothelial cell migration and capillary formation during angiogenesis.

Cell based modeling can assist our understanding and synthesis of such empirical data because it allows us to study the impact of the location of the proliferating region on capillary formation. To the best of our knowledge, no other model has explored the effects of various proliferating regions or segregation of function on capillary morphology. We investigate the role various VEGF isoforms play in the guidance and formation of capillary sprouts, and begin to address questions such as: How does the binding and release of bioavailable VEGF affect local chemical gradients? What are the respective effects on vascular structure of diffusible and matrix bound VEGF? What mechanisms induce proliferation in one cell but not its neighbor? And, can the presence of matrix bound or cleaved soluble angiogenic factors distinguish a proliferating region, possibly explaining both the observed growth differentials and the reports of different proliferating regions?

5.2 Results

5.2.1 Realistic capillary sprout morphology captured

Figure 5.2 depicts a typical simulation demonstrating the model's ability to reproduce realistic capillary sprout morphologies. So that we could attribute any changes in sprout morphology directly to the mechanism or parameter being tested, unless otherwise noted, all simulations used the same parameter set, initial configuration of matrix fibers and tissue cell distribution, and follow the assumptions described in

Chapter IV. Sprout migration is facilitated as the tip cell degrades the matrix fibers and effectively migrates via haptotaxis up these local adhesion gradients. Comparing simulations with and without ECM degradation, we found that tip cell ECM degradation increased the average rate of sprout extension toward the tumor by 5%, a small but statistically significant effect. The resulting morphology of the capillary sprout is determined by several mechanisms: tip cell migration toward positive VEGF and adhesion gradients, cellular adhesion to the ECM, and competition for space. Coordination of or competition among these mechanisms affects cell shape and orientation and can be readily observed during movies of the simulations For instance, interplay between haptotaxis and chemotaxis can result in endothelial cell elongation, a characteristic cell shape for migrating cells, without needing a rule prescribing an elongated cell shape as is done in Merks et al. [110](arrow in Figure 5.2).

Whenever possible, we make every effort to compare cell and sprout dynamics and morphologies observed during simulations with observations from experimental assays. On average, simulated capillary sprouts are $14.2 \pm 2.44\ \mu$m (mean $\pm$ standard deviation) in diameter and $1-2$ cells wide, which compares quantitatively well to measured VEGF induced vessel diameters [91, 101]. We quantify and report the rates of sprout extension under various simulation conditions. Sprout length is determined by measuring the distance from the center of mass of the initial endothelial cell at the base of the sprout to the tip cell's center of mass at the end of the simulation. Average sprout extension velocity is then calculated as the final sprout length over time. Sprout extension rates are presented and discussed in Section 5.2.3 below.

In Section 5.1, several key hypotheses are formulated that are driven by confusing or conflicting results from empirical data. In the following subsections, we use our

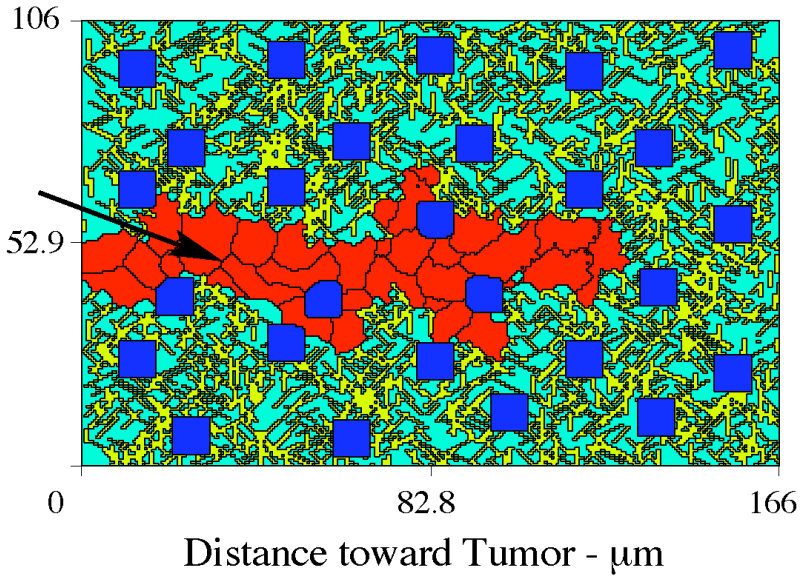

Figure 5.2: Representative simulation showing the model's ability to reproduce realistic capillary sprout morphologies. Sprouts migrate along matrix fibers up chemical gradients of VEGF. The structure of the matrix guides sprout migration and affects cell shape and orientation. The arrow identifies a cell that has elongated due to chemotactic forces and adhesion to the matrix. Parameters used are as given in Table 4.1 except $\gamma_e = 0.7$ and $\gamma_t = 0.8$. Snapshot at 16.6 days.

model to test these hypotheses by relaxing the relevant baseline assumption(s) set forth in Chapter IV.

5.2.2 Local VEGF gradient influences capillary sprout morphology

Recent studies focus on the role of various VEGF isoforms in cellular function [20, 50] and morphogenesis [91] and find that VEGF in soluble versus bound form has a different effect on vascular appearance. There is evidence that steep VEGF gradients can be generated due to either high matrix binding affinity isoforms or as a result of additional soluble VEGF cleaved from the matrix [91, 63, 50]. Since we model capillary sprout formation starting from a single cell, cell densities in the simulations are very low. Numerical solutions to Eq. 4.1 indicate that cell uptake of diffusible VEGF for low cell densities has only a very slight effect on the chemical profile at any time. Consequently, only very shallow gradients of freely diffusible

VEGF are established. Other mathematical models of angiogenesis simulate steep chemical gradients, but these form strictly as a result of VEGF consumption by a large number of endothelial cells [95, 158]. In addition, different tumor geometries (linear versus circular) are assumed that also produce different VEGF gradients [9]. All of these models, however, focus on the effects of VEGF gradients on capillary *network* development and vascular patterning. They are not able to explore the effects of different VEGF gradients on individual cell behavior (stalk, proliferating, and tip cells) or on the changes in sprout morphology that occur as a result of single cell dynamics. Using our model, we investigate the effects of different VEGF gradient profiles on cellular function and how cellular function affects sprout morphology (H1).

In this investigation, we do not explicitly model different isoforms or the binding of VEGF to the matrix. Instead, shallow VEGF gradients are constructed by assuming endothelial cells bind a diffusible VEGF isoform. The resulting gradients are very shallow (Figure 5.3a). To mimic a VEGF isoform that is sequestered in the ECM, we begin with the same initial VEGF profile but no longer provide a constant source of VEGF. Consequently, once an endothelial cell binds to and internalizes a VEGF molecule, VEGF is depleted over time thereby establishing steep local concentration gradients (Figure 5.3c). As in the baseline simulations, each cell decides independently whether or not it has enough VEGF to become activated, v_a. Now, an activated cell additionally decides whether there is enough VEGF present to stimulate proliferation, v_p. We no longer specify a proliferating region just behind the sprout tip, but instead allow the concentration of VEGF to determine endothelial cell proliferation [50]. No experimental data is available for the threshold amount of VEGF required for proliferation, therefore we choose a value to stimulate proliferation approximately 48 hours after the initial cell began migrating into the stroma

[151, 124]. If there is insufficient VEGF, a cell will deactivate and become inert.

Figure 5.3b shows the endothelial cell response to soluble VEGF. As the sprout grows, a greater number of endothelial cells are activated and stimulated to proliferate. Because more cells are growing, the entire sprout is on average 46% larger and the sprout is more invasive. The average diameter of the sprout is 60 μm. Furthermore, because only shallow gradients are formed, the tip cell does not have strong directional preference from chemoattractant gradients. The resulting morphology is a swollen sprout, a morphology consistent with vascular hyperplasia [91]. We also see lateral and backward cell movement following adhesive gradients. Backward migration, or migration back towards the parent vessel, is an observed phenomenon *in vivo* (see Figure 1 in [158]) and is also numerically simulated in Sun et al. [158]. Figure 5.3d depicts the capillary morphology that results from steep extracellular gradients of matrix bound VEGF. The morphology is strikingly different. As VEGF is depleted, there is a reduction in the size of the proliferating region and some cells eventually became inactive. In addition, steep gradients provide strong migrational cues to the tip cell and the result is a less invasive sprout with an average diameter of 20 μm. For shallow gradients, increasing the proliferating threshold effectively introduces a delay in the dynamics. In both cases, however, the ultimate capillary morphology is unchanged. The morphologies we observe agree well with the experimental observations in Lee et al. [91], experiments that test the angiogenic responses to different VEGF isoforms *in vivo* (see Figure 5.4). Lee et al. [91] demonstrates that endothelial cell receptor activation by soluble VEGF induces significant cell proliferation and broad invasion of the stroma (vessel diameter of 109 μm), whereas receptor activation by matrix bound isoforms result in filopodia extension, limited stromal invasion, and cell-cell associations consistent with sprouting angiogenesis

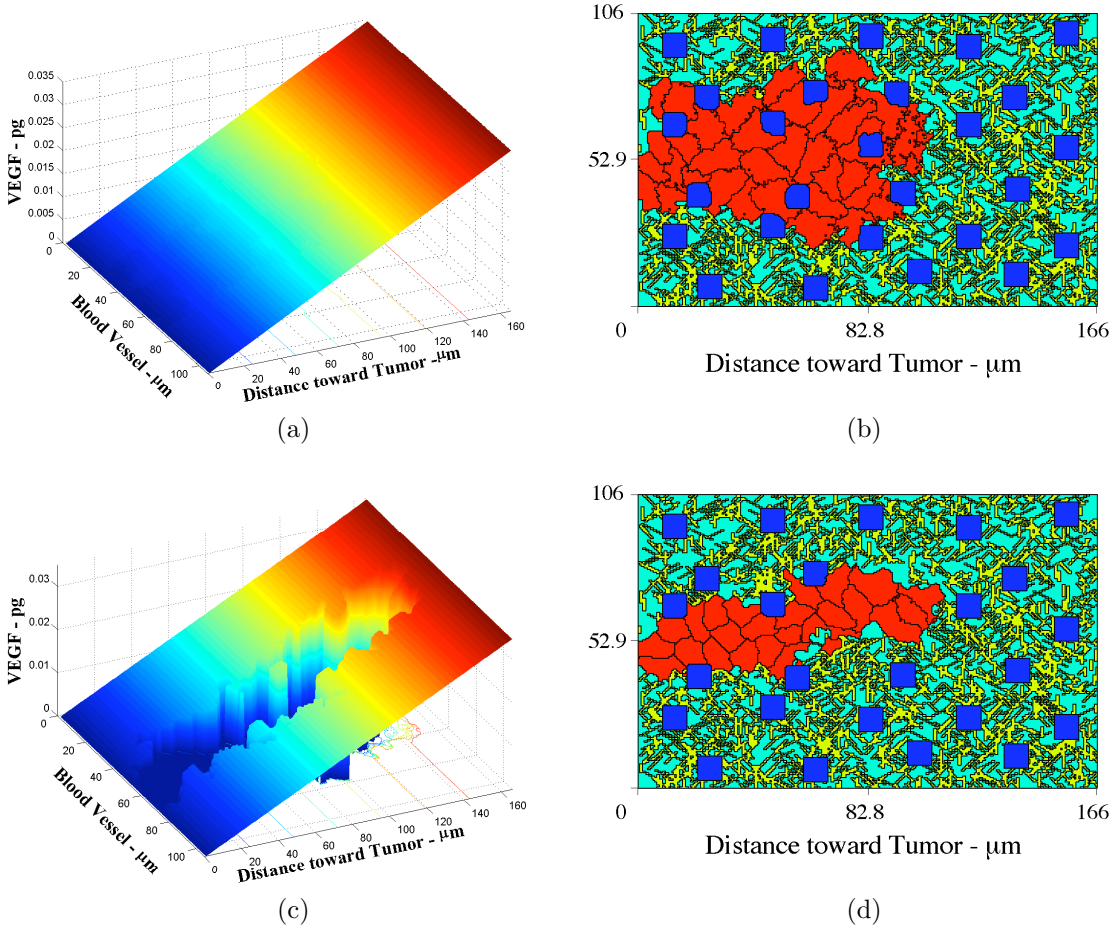

Figure 5.3: Markedly different capillary sprout morphologies result from shallow (a) versus steep (c) VEGF gradients. Swollen, invasive sprouts result from shallow VEGF gradients that develop when freely soluble VEGF is expressed (b), whereas when matrix bound VEGF isoforms are assumed, steep gradients develop and result in narrower capillary sprouts (d). Both results concur with the experimental observations of Lee et al. [91] shown in Figure 5.4. Parameters are given in Table 4.1. Snapshots at (b) 9.4 and (d) 16.6 days.

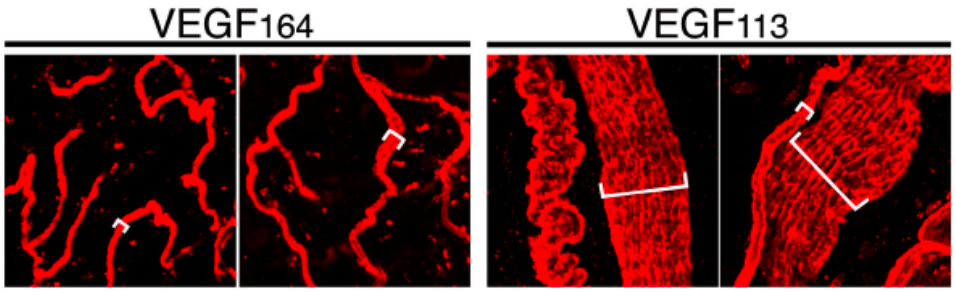

Figure 5.4: Results from experiments testing the angiogenic responses to different VEGF isoforms *in vivo* [91]. Left: Endothelial cell activation by $VEGF_{164}$, a matrix bound isoform, results in limited stromal invasion and average vessel diameters of 15 μm. Right: Soluble $VEGF_{113}$ induces significant cell proliferation and broad invasion of the stroma (vessel diameters 109 μm). Compare with simulated sprout morphologies shown in Figure 5.3.

(vessel diameter of 15 μm). Moreover, endothelial cells in shallow VEGF gradients lose their directional guidance cues [50]. This observation agrees with the results of [50], where tip cell filopodia lose their polarity and excessive filopodia extend from stalk cells in response to shallow gradients of VEGF in transgenic mice expressing only $VEGF_{120}$.

5.2.3 Average rates of sprout extension are affected by proliferating region and cooperation of cellular functions

As previously discussed, experimental models report conflicting results regarding the precise region of proliferating cells during angiogenesis. We use our model to investigate the effects of various proliferating regions on capillary morphology and on the average rate of sprout extension toward the tumor (H2). We look at capillaries that develop with proliferation occurring (i) only at the tip of the growing sprout, (ii) immediately behind the sprout tip, (iii) three cell lengths behind the advancing tip, and (iv) at the base of the sprout. Because newly formed sprouts have not yet re-synthesized a basement membrane, proliferation in these different regions is biologically feasible. Empirical evidence quantifying the distribution of cell divisions during sprout formation shows that proliferation can occur at the tip, behind the

tip, and at the base of newly formed sprouts [79]. As in our baseline simulations, if a cell is proliferating, it does not move chemotactically. We run all simulations for the same duration and use the same parameter set (Table 4.1).

Figure 5.5 shows the resulting sprouts when proliferation occurs at the base (top inset) and at the tip (lower inset) of the sprout. We find that the position of the proliferating region does not significantly influence sprout morphology. Figure 5.5 also shows the relationship between the proximity of the proliferating region to the tip and sprout extension speeds toward the tumor. The data indicate that as the proliferating region moves further away from the migrating tip, the average rate of sprout extension toward the tumor increases. These results suggest some interplay or competition between the mechanical or biochemical forces exerted by the migrating tip and the proliferating cells. The migrating tip moves toward the source of chemoattractant and the neighboring cells are pulled along via cell-cell adhesion. On the other hand, proliferating cells do not necessarily grow directly toward the chemical source. This is because it requires less energy for the cells that make up the capillary sprout to grow into matrix and fluid than to invade the space occupied by other cells. In addition, a proliferating cell does not migrate and consequently anchors neighboring cells via cell-cell adhesion. When a proliferating cell is adjacent to a migrating cell, each phenotype has to overcome the forces exerted by the other. However, once the proliferating region is far enough away, there is no statistically significant change in sprout extension speed, suggesting that the forces exerted by each phenotype have only short range effects.

To investigate the validity of this explanation, we perform a numerical experiment identical to (i) above except that migration and proliferation are no longer independent and exclusive cellular events. It has been shown empirically that proliferation

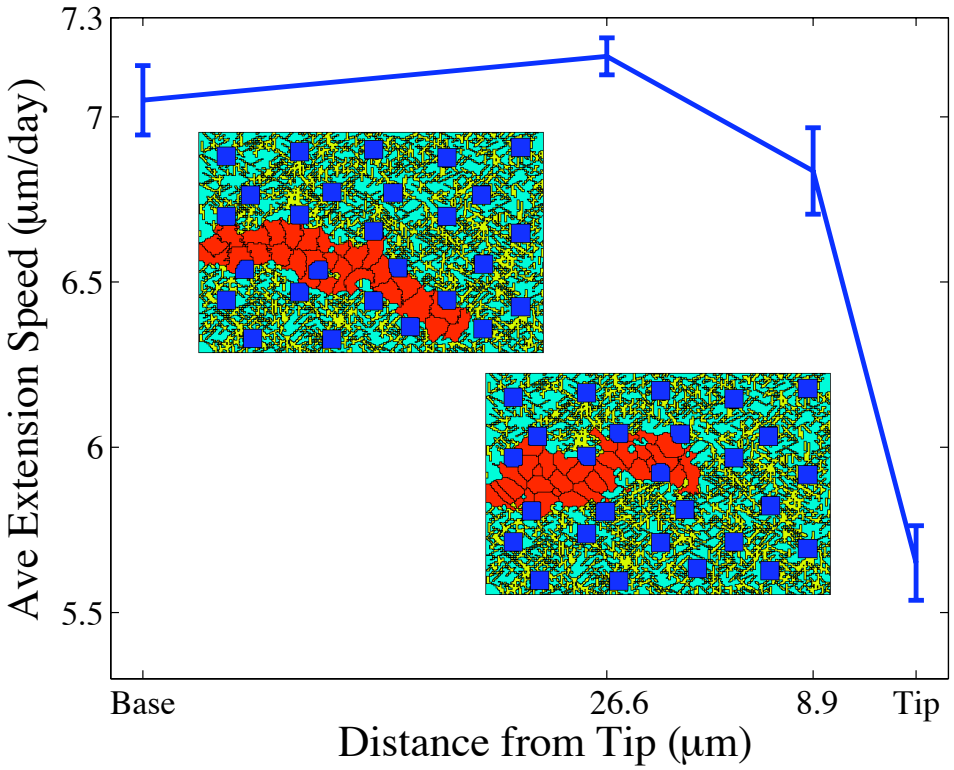

Figure 5.5: The relationship between the average rate of sprout extension and the location of the proliferating region. The further the proliferating region from the migrating tip, the faster the average rate of sprout extension due to the interplay between the chemotactic forces exerted by the migrating tip and competition for space by the proliferating cells. Error bars represent standard deviations from the mean using a sample of 12 simulations. Parameters are as given in Table 4.1 except $\gamma_e = 0.7$ and $\gamma_t = 0.8$.

and migration are not isolated cellular functions [79]. We find that when proliferating cells also move chemotactically, the average rate of sprout extension increases to 7.7 μm/day, significantly faster than any of the speeds observed for all proliferating regions tested. This rate represents a 36.5% increase above the rate observed in (i) and a 7.4% increase over the fastest average speed observed (i-iv). This finding supports the view that proliferating and migrating cells exert short range competing forces on each other and further suggests that coordination of these cellular functions could have a significant effect on the rate of capillary extension. Our examination does not rule out the possibility that multiple proliferating regions may exist.

5.2.4 Stroma composition & ECM structure: Mechanisms for capillary sprout branching and anastomosis

As shown in Figure 5.6a, our model is able to reproduce branching structures. An exciting feature of this model is that branching occurs naturally as a result of known cellular and molecular level dynamics, not as a result of predefined probabilistic rules. To our knowledge, no other model of tumor-induced angiogenesis has simulated sprout branching without *a priori* prescribing a phenomenological rule. Movies of capillary sprout evolution are evaluated to examine the possibility that heterogeneities in the stroma induced branching. We observe that the direction of sprout migration is predominantly determined by chemotaxis and endothelial cell adhesion to and movement along the matrix fibers. As the leading cells encounter variable matrix densities and other stromal cells, the sprout changes direction to find a path of lower resistance through the stroma. Regions of higher density matrix impose a barrier to forward migration, whereas regions of relatively low densities do not provide enough adhesion or cellular support for migration. Both extremes cause the sprout to change direction and lead to more tortuous sprout morphologies. We hypothesize that matrix fiber heterogeneity or intercellular pressure by tissue cells provides an opportunity for the redirection of the entire sprout or of individual cells (H3). It is possible that it is this redirection or migration of individual cells that leads to branch formation. Whether or not a branch emerges depends on the combination of local forces acting on the individual cells. Forces induced by cell-matrix adhesion coupled with chemotaxis or intercellular pressures may facilitate cellular migration away from the main body of the developing sprout. Compared to other models of tumor-induced angiogenesis that simulate the "brush border" effect [9, 158], which is an increased incidence of branching as the sprout approaches the tumor [116], the

length of our computational domain is much shorter. Consequently, in our small simulation domain, we do not expect to reproduce the brush border effect captured on longer length scales (1−2 mm) that allow multiple branching points to form.

To investigate the possibility that the tessellated structure of the stroma may have generated the observed capillary sprout branching, we conduct three additional numerical experiments: sprout formation 1) in the absence of tissue specific cells, 2) in the absence of matrix fibers, and 3) within a homogeneous extravascular environment (no matrix and no tissue cells). We then examine the effects of altering the compressibility of the tissue cells. All simulations are identical except for the absence of tissue cells or matrix fibers. Figure 5.6b-d show representative final images from numerical experiments 1−3 respectively. In the first experiment, we completely remove the tissue cells from the stroma. Figure 5.6b shows that a branch still emerges, but in this case it develops solely in response to chemotactic gradients and cell-matrix adhesion. We then observe sprout formation in the absence of matrix fibers (Figure 5.6c). In this simulation, the tip cell is slowed by and deforms itself to accommodate a tissue cell. The resistance from the tissue cell is enough to redirect the leading cells and the sprout splits forming a branch. In the last experiment, we simulate sprout formation in the absence of both tissue specific cells and matrix fibers (Figure 5.6d). This experiment examines sprout migration due to chemotaxis and cell-cell adhesion alone. As may be expected, the sprout is more linear and cells appear more elongated due to the effects of chemotaxis, but the sprout is also larger in diameter and much slower (see Table 5.1). This is because the absence of an extracellular matrix results in a loss of adhesive guidance cues generally provided by the matrix fibers and consequently a decrease in tip cell polarity. Interestingly, we also observe greater persistence in sprout migration, that is, once the sprout is oriented, it does not easily change its

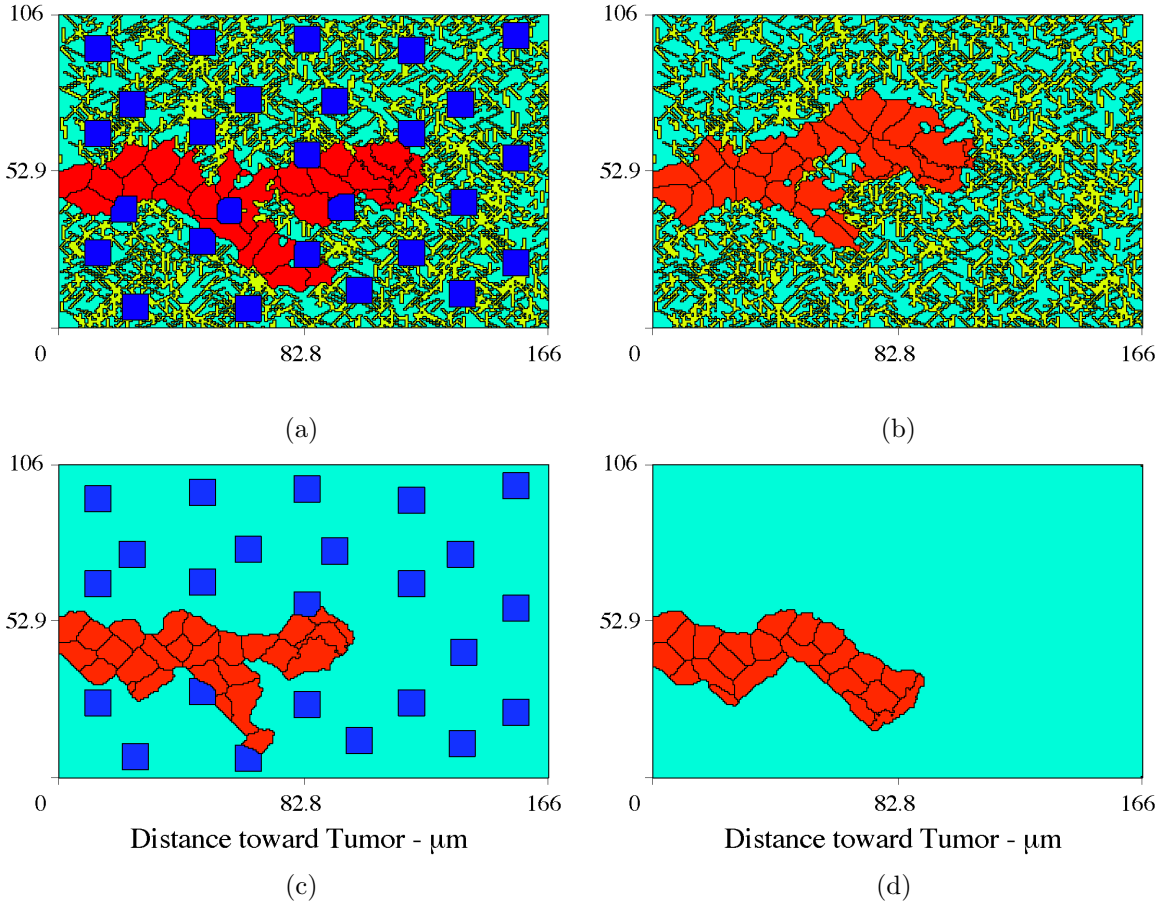

Figure 5.6: Numerical simulations ruling out the possibility that branching is induced solely by the tessellated structure of the stroma. For an identical parameter set, (a) depicts a branch emerging from the main capillary as a result of anisotropies in the stroma, (b) demonstrates that the structure of the matrix fibers alone can induce branching, and (c) shows branch formation induced by resident tissue cells. No branching occurs in a homogeneous extracellular environment due to a loss of adhesive guidance cues (d). Parameters are given in Table 4.1. Results suggest two plausible mechanisms for sprout branching: the resistance created by other cells in the tissue and the structure of matrix fibers. Snapshot at 16.6 days.

direction. This is not surprising when presented with the extensive evidence that the ECM plays a crucial role in sprout guidance and morphology. In support of our hypothesis that inhomogeneities in the stroma are a mechanism for branching, we do not see sprout branches in the absence of variable stromal structure. Table 5.1 compares the average extension speeds and average sprout diameters for the various stromal compositions. The rates of sprout extension for sprouts developing without an extracelluar matrix are significantly slower than those that develop with the additional migratory cues provided by the matrix fibers. Average extension speeds and average diameters are not statistically different for sprouts growing in the absence of an ECM. The average rate of sprout extension due to chemotaxis is 5.33 μm/day. The possibility for endothelial cells to additionally employ extracellular matrix fibers for migration results in a 18−28% increase in average extension speed. In another

Table 5.1: Table comparing average migration speeds and average sprout diameters for different stromal compositions. Averages are computed from a sample of 12 simulations with identical parameters and initial conditions. Average migration speed of the sprout is calculated as sprout tip displacement at the end of the simulation from the initial endothelial cell per time.

Stromal Composition	Ave. Migration Speed mean ± std error (μm/day)	Ave. Sprout Diameter mean ± std error (μm)
No fibers, no tissue cells	5.33 ± 0.075	19.29 ± 0.26
Tissue cells only	5.41 ± 0.074	19.08 ± 0.46
Matrix fibers only	6.33 ± 0.131	14.41 ± 0.26
With fibers & tissue cells	6.84 ± 0.131	14.20 ± 0.70

series of numerical experiments, varying the compressibility of the tissue cells does not result in any significant differences in capillary development.

Figure 5.7 shows the development of capillary sprouts from five endothelial cell buds. As the sprouts extend toward the tumor, two neighboring sprouts merge and form a loop, a process called anastomosis. Anastomosis is also simulated by other mathematical models of angiogenesis, where the lateral motion of the sprout tip

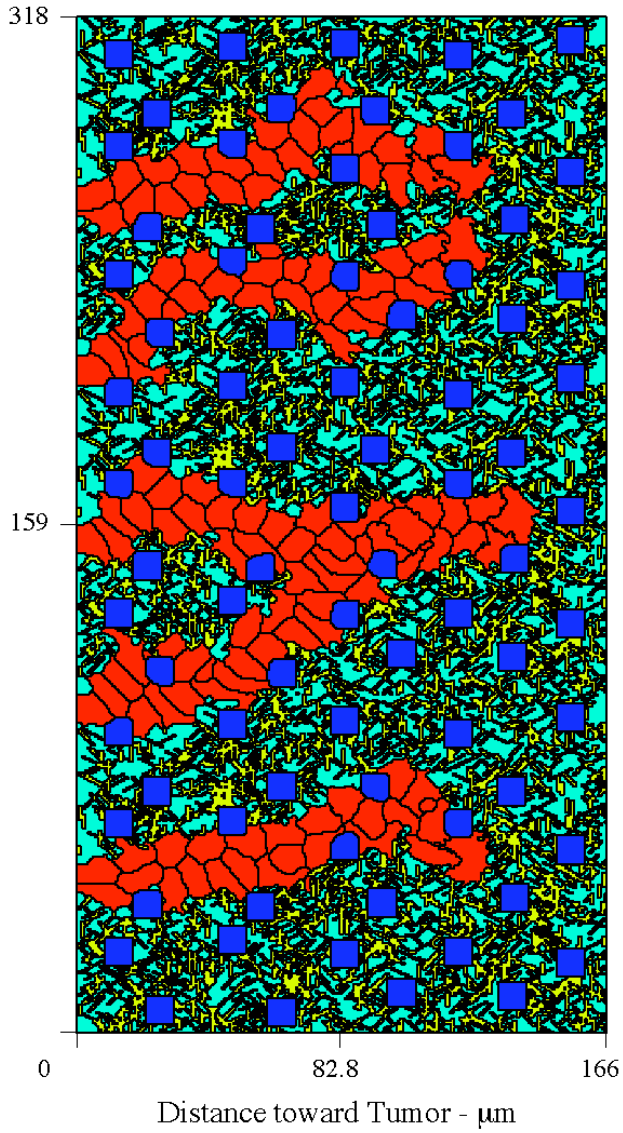

Figure 5.7: The development of capillary sprouts from five endothelial cell buds. Two neighboring sprouts merge to form a loop, a process known as anastomosis. In this simulation, anastomosis was a preferred lower energy state structure given the known physical dynamics at the cellular level. Parameters are given in Table 4.1. Snapshot at 16.6 days.

is influenced by positive adhesive gradients created by endothelial cell fibronectin uptake [9, 158] and by matrix heterogeneities [158]. In our model, the lateral motion of the sprouts similarly occurs as a result of local adhesive gradients that naturally exist due to matrix anisotropies, but also occurs as a result of the positive gradients created through endothelial cell matrix degradation. Sprout migration is further directed by endothelial cell surface binding to matrix fibers and by the resistance from extravascular tissue cells. When two neighboring sprouts encounter each other, they may or may not merge to form a loop. That is, whether or not anastomosis will occur depends on the dynamics of individual cell-cell and cell-matrix binding, coupled with chemotactic and haptotactic gradients. As with branching, loop formation emerges naturally as a collective result of single cell behaviors and is a preferred lower energy state structure. We would like to point out that as the sprouts that form loops mature, blood would begin to circulate and the forces associated with the flow of blood could cause side branching. Consistent with Bautch et al. [79], our simulations show that blood flow is not necessary for tip branching and anastomosis.

Our numerical studies indicate that the anisotropic structure of the matrix fibers strongly influences the direction and morphology of the migrating capillary sprout. During simulated endothelial cell migration, resistance from tissue cells and endothelial cell adhesion to matrix fibers, both alone and in concert, is sufficient to cause branching and anastomosis to occur. In addition, regions of either high density or very low density matrix alone can inhibit and redirect endothelial cell movement inducing capillary sprout branching. These results suggest that the anisotropy of the matrix fibers and the composition of the stroma may be important mechanisms leading to capillary sprout branching and anastomosis.

5.2.5 Sensitivity analysis

The sensitivity of the results to the particular parameter set chosen is studied by varying one parameter at a time. First, holding matrix fiber density constant, we randomly generate alternative ECM structures as described in Section 4.4 and find that our results do not qualitatively change. Further studies show that the results are insensitive to changes in $\gamma_{\mathrm{f}}, \gamma_{\mathrm{m}}$, and γ_{t}, but cell size depends on γ_{e} and cell shape depends on J_{em}. Larger values of γ_{e} (requires more energy to grow) yield smaller cells and the smaller the value for J_{em} (stronger bond), the more elongated the cell. Varying the chemical potential, μ_σ, affects both shape and size. As μ_σ is increased by an order of magnitude, the cells become much larger and more elongated and sprout extension is rapid and pervasive. Increasing μ_σ increases the ratio of chemotactic potential to growth and adhesion and causes the system energy changes to be dominated by the effects of chemotaxis. Very little difference is seen in cell size and shape until μ_σ is decreased three orders of magnitude, at which point cells become rounder and sprout extension is stunted. Significantly decreasing μ_σ is equivalent to having no chemotactic forces in the system. The results are not sensitive to the value of kT until this value is increased more than two orders of magnitude. At this point the cells break up because larger values of kT correspond to greater cell membrane fluctuations.

5.3 Discussion

Tumor angiogenesis is an important step in cancer development. Recent experimental advances highlight the increasingly complex and still largely unresolved mechanisms driving tumor angiogenesis. We formulate specific hypotheses relevant to the investigation of biomechanical and biochemical mechanisms. We present a cell-based

model of tumor angiogenesis incorporating endothelial cells, stroma tissue, ECM and interstitial fluid, as well as VEGF dynamics. This model reflects a realistic representation of the complex and dynamic nature of the tumor microenvironment with multiple cell types and reciprocal cellular and molecular interactions. We demonstrate its capacity to capture realistic dynamics and capillary sprout morphologies, such as preferential sprout migration along matrix fibers, cell elongation, and more complex events, such as branching and anastomosis, that occur during angiogenesis. Our model provides a framework for incorporating biochemistry and biophysics in investigations of mechanism.

We provide evidence that differences in the matrix binding affinity of VEGF isoforms could affect the VEGF profile and show that vastly different capillary morphologies result in the presence of steep versus shallow extracellular chemical gradients. Our model reproduces narrow sprouts in the presence of steep VEGF gradients and swollen sprout formation due to well distributed concentrations of VEGF; both morphologies and mechanisms are consistent with those observed empirically [91, 50]. Results from our model emphasize the importance of capturing not only the correct chemical profile, but also the correct mechanisms inducing the extracellular chemical profiles. Models of angiogenesis inducing steep gradients as a result of VEGF uptake by a large number of cells may be neglecting a vital mechanism responsible for the modulation of endothelial cell function and vascular form. To date, mathematical models have focused on the effects of tumor secreted VEGF in a freely diffusible form. If we hope to understand the mechanisms regulating capillary formation, models must incorporate other VEGF isoforms and allow for VEGF binding to and liberation from the ECM. Using this model as a starting point, we can examine the the role of different VEGF isoforms on the spatial profile of bio-available

VEGF and on cellular function regulation. In addition, this model can be used to test the hypothesis that the proteolytic release of matrix bound VEGF isoforms naturally defines a proliferating region of endothelial cells resulting in local growth differentials.

The underlying mechanisms by which a proliferating region is established during angiogenesis are still unknown. We identify experimental models of angiogenesis that report cell proliferation from distinctly different regions of a developing sprout. Using our model, we explore the effects of various proliferating regions on capillary sprout growth. Results from our numerical simulations show that as the proliferating region moves further from the sprout tip, sprout extension is more rapid due to diminishing competing intercellular forces. Results also show that the location of the proliferating region does not influence sprout morphology. We demostrate that capillary sprout extension is significantly more rapid when cellular functions (migration and proliferation) are not mutually exclusive. These results highlight just how tightly regulated the processes involved in angiogenesis are and indicate the need for studies of the relative importance of chemotaxis and proliferation on capillary development. Furthermore, in our numerical experiments, the proliferating region advances because it is a fixed distance from the sprout tip throughout the simulation. *In vivo*, however, it may be that as the sprout extends toward the tumor, the proliferating region remains fixed, that is, the region lags further and further behind the advancing tip [65]. Coupled with our finding that sprout extension speed is affected by the location of the proliferating region, this could possibly explain the increase in capillary migration speeds seen empirically as capillary networks approach the tumor.

The composition and structure of the stroma through which the new capillaries

must grow in order to reach the tumor is highly tissue dependent. We examine the role of tissue inhomogeneities by explicitly modeling the interactions between endothelial cells and the stroma, specifically the matrix fibers, resident tissue cells and interstitial fluid. Our studies reveal that local anisotropies in the stroma, such as variable matrix fiber density and the presence of other tissue cells, influence sprout migration and morphology during angiogenesis and may be mechanisms for sprout branching and anastomosis. Although the morphology of branching and anastomosis has been fully described [124, 79], little is understood of the cellular and molecular mechanisms inducing the formation of these sprout structures. In our model, anastomosis and branching occur because they are preferred lower energy state structures given the chemical and mechanical dynamics incorporated at the cellular level. These results underscore the importance of modeling cell-matrix and cell-cell dynamics, and demonstrate that a cell-based physical model can help provide insight into the processes controlling angiogenesis.

At present, quantifying our results and validating our model is not a straightforward task. Measurements of microvessel densities over time, branching points/mm/time, and capillary network expansion rates exist for vascular networks that form on larger spatial scales. However, our model focuses on cell-cell and cell-matrix interactions at the very onset of angiogenesis, when the newly formed sprouts consist of only a few cells. Over the spatial scale of our model, which is significantly smaller, we do not expect multiple branch points to form. Assays and quantitative measures of early single sprout morphology under conditions that mimic the early events that occur *in vivo* during tumor-induced angiogenesis have not been well developed. In particular, to our knowledge there has been no systematic study of collective cell or sprout migration and morphology that quantifies the effects of chemotaxis. In ad-

dition, experimental models that measure individual cell migration rates cannot be directly compared to the rate at which a capillary sprout travels or extends toward a tumor, because cell-cell dynamics are not considered in assays of single cell motility and during sprout extension migrating cells are adhered to other cells that may be anchored to the matrix or moving in different directions.

Average speeds of *in vivo* and *in vitro* vessel growth are reported at $0.1-0.3$ mm/day [79, 42]. The average rate of sprout extension in our model is considerably slower. This difference can be attributed to a combination of several factors. First, in our simulations, cell proliferation occurs for only one cell. Simulating multiple proliferating regions or proliferation in multiple cells does increase the rate of sprout extension in our model. Figure 5.3b shows an increased sprout extension rate when there are more proliferating cells. This sprout has migrated the same distance as the sprout in Figure 5.3d but in only 9.4 days versus 16.6 days. However, proliferation alone does not explain the difference in sprout migration rates. Other factors that contribute to sprout extension speeds are the ECM density, cell elongation, and blood flow. Endothelial cells can elongate up to 10 times their normal length [79] and the density and alignment of matrix fibers has a major effect on cell migration rates [44]. In Chapter VI we investigate the effects of cell elongation on sprout extension speeds, measure sprout velocity through matrices of varying densities and patterns, and predict an optimal density for maximum sprout migration speeds. Another dynamic that has a significant impact on simulated sprout extension speed is the ability to capture sheet or collective migration of a group of cells as is observed in vascular sprouting [85]. An important mechanism in both single cell and collective migration is the detachment from the ECM and subsequent retraction of the trailing edge of the cell [45]. Preliminary studies of simulated single cell migration and sprout forma-

tion incorporating these cellular motility mechanisms suggest that sprout migration speeds may more than double. Chapter VI presents a formal investigation of sprout formation using an extended model that incorporates cell detachment from the ECM and collective migration and our results confirm that sprout extension rates significantly increase. In fact, simulations of sprout development using the extended model reproduce sprout velocities consistent with empirical data.

CHAPTER VI

Topography of Extracellular Matrix Mediates Vascular Morphogenesis

The extracellular matrix plays a critical role in orchestrating the events necessary for wound healing, muscle repair, morphogenesis, new blood vessel growth, and cancer invasion. In this study, we investigate the influence of extracellular matrix topography on the coordination of multi-cellular interactions in the context of angiogenesis. To do this, we validate our spatio-temporal cellular model of angiogenesis against empirical data, and within this framework, focus on the effects of extracellular matrix topography on capillary sprout morphology and average extension speeds. We vary the density of the matrix fibers to simulate different tissue environments and to explore the possibility of manipulating the extracellular matrix to achieve pro- and anti-angiogenic effects. The model predicts specific ranges of matrix fiber densities that maximize sprout extension speed, induce branching, or that interrupt normal angiogenesis. We then explore matrix fiber alignment as a key factor contributing to peak sprout velocities, and in mediating cell shape and orientation. We also quantify the effects of proteolytic matrix degradation by the tip cell on sprout velocity and demonstrate that degradation promotes sprout growth at high densities, but has an inhibitory effect at lower densities. Our results are discussed in the context of ECM targeted pro- and anti-angiogenic therapies that can be tested empirically.

Experimental assays of angiogenesis are performed in a variety of *in vivo* animal models [11, 116] and *in vitro* matrix gels [164, 25, 100, 78]. The actual densities of these model extracellular matrices vary. Physiological values for the volume fraction of collagen fibers in healthy tissues range from 0.026 in the myocardium, 0.142 in skeletal muscle, 0.293 in the corneal stroma, to 0.661 in the dermis [94]. To aid our understanding of vessel growth in various tissues and to evaluate the efficacy of manipulating the extracellular matrix as a pro- and anti-angiogenic therapy, we focus our investigation on how the topography of the ECM influences, via cell-matrix adhesion, individual and collective cellular responses during early angiogenic sprout development.

In this chapter, we extend the cellular model of angiogenesis from chapter IV to investigate the effects of ECM topography on cell-matrix interactions during vascular morphogenesis. We show the dependence of sprout extension speed and morphology on matrix density, fiber network connectedness, and fiber orientation. Notably, we observe that varying matrix fiber density affects the likelihood of capillary sprout branching. As a result, the model predicts an optimal density for capillary network formation and suggests high fiber anisotropy as a mechanism for sprout branching. We also identify unique ranges of matrix density that promote sprout extension or that interrupt normal angiogenesis and show that maximal sprout extension speeds are achieved within a density range similar to the density of collagen found in the cornea. Finally, we quantify the effects of proteolytic matrix degradation by the tip cell on sprout velocity and demonstrate that degradation promotes sprout growth at high densities, but has an inhibitory effect at lower densities.

This chapter is organized in the following manner. First, we discuss several key improvements to our cellular model of angiogenesis and validate this extended model

against empirical measurements of sprout extension speeds *in vivo*. We then use our model to investigate the effect of ECM topography on vascular morphogenesis and focus on mechanisms controlling cell shape and orientation, sprout extension speeds, and sprout morphology. Based on our findings, we suggest and discuss several ECM targeted pro- and anti-angiogenesic therapies that can be tested empirically.

6.1 Extended Cellular Model of Angiogenesis

To more accurately capture the cell-cell and cell-matrix interactions that occur during vascular morphogenesis, we have implemented several additional features to the cell-based model of angiogenesis introduced in Chapter IV. We extend that model to incorporate endothelial cell recruitment from the parent vessel and stalk cell migration, mechanisms that facilitate sprout extension. We use this extended model as a framework to study how ECM topography influences intercellular and cell-matrix interactions.

The extended model uses a lattice-based cellular Potts model describing individual cellular interactions coupled with a partial differential equation to describe the spatio-temporal dynamics of vascular endothelial growth factor. At every time step, the discrete and continuous models feedback on each other and describe the time evolution of the extravascular tissue space and the developing sprout. The discrete model evolves by the Metropolis algorithm: the lattice updates are accepted probabilistically if the update reduces the total energy of the system. The system energy, E, includes a term describing cell-cell and cell-matrix adhesion, a constraint for cellular growth, and an effective chemotaxis potential that is proportional to the local

VEGF gradient, ΔV, and is given by:

$$E = \underbrace{\sum_{\text{sites}} J_{\tau,\tau'}\left(1-\delta_{\sigma,\sigma'}\right)}_{\text{adhesion}} + \underbrace{\sum_{\text{cells}} \gamma_{\tau}\ \left(a_{\sigma}-A_{\sigma}^{T}\right)^{2}}_{\text{growth}} + \underbrace{\sum_{\text{sites}} \chi_{\sigma}\Delta V}_{\text{chemotaxis}}\ . \tag{6.1}$$

In the first term of Eq. 6.1, $J_{\tau,\tau'}$ represents the binding energy between model constituents. For example, $J_{\mathrm{e,e}}$ describes the relative strength of cell-cell adhesion that occurs via transmembrane cadherin proteins. Similarly, $J_{\mathrm{e,f}}$ is a measure of the binding affinity between an endothelial cell and a matrix fiber through cell surface integrin receptors. Each cell is associated with a unique identifying number, σ; $\delta_{\sigma,\sigma'}$ is the Kronecker delta function. Thus $(1-\delta_{\sigma,\sigma'})$ ensures that the adhesive energy only accrues at cell surfaces. The second term describes the energy expenditure required for cell growth and deformation. a_{σ} denotes cell σ's current volume and A_{σ}^{T} is a specified "target" volume. For proliferating cells, the target volume is double the initial volume. In the third term, the parameter $\chi_{\sigma} < 0$ is the effective chemical potential and influences the strength of chemotaxis relative to other parameters in the model. $V = V(x,y,t)$ denotes the concentration of VEGF. A source of VEGF, S, is supplied to the stroma from the right hand boundary. A gradient of VEGF is established as VEGF diffuses through the stroma with diffusivity coefficient $D > 0$, decays at a constant rate $\lambda > 0$, and is taken up by endothelial cells, $B(x,y,V)$. The spatial profile of VEGF satisfies a partial differential equation of the form:

$$\frac{\partial V}{\partial t} = D\nabla^{2}V - \lambda V - B(x,y,V).$$

Initial and boundary conditions for VEGF are $V(x,y,0) = 0$ and $V(0,y,t) = 0, V(L_1,y,t) = S, V(x,0,t) = V(x,L_2,t)$. The physical meanings and values of the parameters used in this extended model are listed in Table 6.1.

Thusfar, the extended model is identical to the previous model and a complete

description of the model assumptions, including a biochemical derivation of the function for endothelial cell binding and uptake of VEGF, is given in Chapter IV. We implement several additional features to improve the biological realism of that model. One improvement is the implementation of stalk cell chemotaxis. Stalk cells are not inert, but actively respond to chemotactic signals [50]. As a consequence, cells migrate as a collective body, a phenomenon called collective or cohort migration [85]. This modification, however, also makes it possible for individual cells, as well as the entire sprout body, to migrate away from the parent vessel, making it necessary to consider cell recruitment from the parent vessel.

During the early stages of angiogenesis, cells are recruited from the parent vessel to facilitate sprout extension [124]. Bautch et al. [79] measured the number and location of cell divisions that occur over 3.6 hours in *in vitro* vessels 8 days old (see Section 6.2.1 herein for a detailed description of these experiments). They defined the sprout field as the area of the parent vessel wall that ultimately gives rise to the new sprout and the sprout itself. The sprout field was further broken down into regions based on distance from the parent vessel and was classified as distal, proximal, and nascent. Bautch et al. reported that 90% of all cell divisions occur in the parent vessel and the remaining 10% were located in the nascent area of the sprout field, at or near the base of the sprout. On average, total proliferation accounted for approximately 5 new cells in 3.6 hours, or 20 cells in 14 hours. This data suggests that there is significant and sufficient proliferation in the primary vessel to account for and facilitate *initial* sprout extension. This data does not suggest that proliferation in other areas of the sprout field does not occur at other times. Indeed, it has been established that a new sprout can migrate only a finite distance into the stroma without proliferation and that proliferation is necessary for continued sprout

extension [151]. We model sprout extension through a cell-cell adhesion dependent recruitment of additional endothelial cells from the parent vessel. As an endothelial cell at the base of the sprout moves into the stroma, cell-cell adhesion pulls a cell from the parent vessel along with it. We assume, based on the data presented in [79], that there is sufficient proliferation in the parent vessel to provide the additional cells required for initial sprout extension while maintaining the physical integrity of the parent vessel.

As in our previous model, once a cell senses a threshold concentration of VEGF, given by v_a, it becomes activated. We recognize that cells have distinct phenotypes that dictate their predominate behavior. We distinguish between tip cells, cells that are proliferating, and stalk cells. Tip cells are functionally specialized cells that concentrate their internal cellular machinery to promote motility [50]. Tip cells are highly migratory pathfinding cells and do not proliferate [50, 79]. The remainder of the cells are designated as stalk cells and use adhesive binding to and release from the matrix fibers for support and to facilitate cohort migration. Stalk cells also sense chemical gradients although these cells are not a highly motile phenotype as are the specialized tip cells. Proliferating cells are located behind the sprout tip [50, 79] and increase in size as they move through an 18 hour cell cycle clock in preparation for cell division [170]. Cells that are proliferating can still migrate [79]; it is only during the final stage of the cell cycle that endothelial cells stop moving and round up for mitosis [communication with C. Little]. Since we assume that the presence of VEGF increases cell survivability, we do not model endothelial cell apoptosis.

Cells must simultaneously integrate multiple forces, namely, intercellular adhesion, chemotactic forces, and tractional forces as cells adhere to matrix fibers. To do so, cells deform their shape and dynamically regulate adhesive bonds. In the model,

it is also possible that in concert these forces may cause a cell to be pulled or split in two. To balance these external forces, we introduce a continuity constraint that preserves the physical integrity of each individual cell. This constraint expresses that it is energetically expensive to compromise the physical integrity of a cell and is incorporated into the equation for total energy (Eq. 6.1) by including a term of the form

$$E_{\text{continuity}} = \sum_{\text{cells}} \alpha \left(1 - \delta_{a_\sigma, a'_\sigma}\right),$$

where α is an effective *intra*cellular adhesion energy related to the cytoskeletal matrix of a cell. a_σ represents the current size of the endothelial cell with unique identifying number σ, and a'_σ is a breadth first search count of the number of continuous lattice sites occupied by that endothelial cell. Thus, $a'_\sigma \neq a_\sigma$ signals that the physical integrity of the cell has been compromised and a penalty to total energy is incurred.

As described in detail in Chapter IV, we model the mesh-like anisotropic structure of the extracellular matrix by randomly distributing 1.1 μm thick bundles of individual collagen fibrils at random discrete orientations between -90 and 90 degrees. Model matrix fibers comprise approximately 40% of the total stroma and the distribution of the ECM is inhomogeneous with regions of varying densities. To relate the density of this model fibrillar matrix to physiological values, we measure matrix fiber density as the ratio of the interstitium occupied by matrix molecules to total tissue space, $0 \leq \rho \leq 1$, and compare it to measured values of the volume fraction of collagen fibers in healthy tissues [94].

6.1.1 Parameter calibration

A list of values for the model parameters is provided in Table 6.1, including references. Parameters are taken from experimental data whenever possible. If no

reference is given, the parameter is a relative value chosen to emulate the physical properties and behaviors of cells. The membrane elasticities, γ_τ, are chosen to reflect the relative compressibility of the cell, fiber, or of interstitial fluid. The chemotactic potential, χ_σ, is chosen so that its contribution to the change in total energy is the same order of magnitude as the contribution from adhesion or growth. The difference between the concentration of VEGF at two adjacent lattice sites is on the order of 10^{-4}. To balance adhesion and growth, χ_σ must be on the order of 10^6. We calibrated this parameter to maximize sprout extension speeds while maintaining the physical integrity of the cells. By equating the time it takes an endothelial cell to divide during the simulation with the endothelial cell cycle duration of 18 hours, we convert Monte Carlo steps to real time units. In the simulations reported in this chapter, 1 Monte Carlo step is equivalent to 1 minute.

6.2 Results

6.2.1 Model validation

The canonical benchmark for validating models of tumor-induced angiogenesis is the rabbit cornea assay [52, 11]. In this *in vivo* model, tumor implants are placed in a corneal pocket approximately $1-2$ mm from the limbus. New vessel growth is measured with an ocular micrometer at 10x, which has a measurement error of $\pm$ 0.1 mm or 100 μm. Initially, growth is linear and sprout extension speeds are estimated at a rate of 0.5 mm/day, or 20.8 $\pm$ 4.2 μm/hr. Sprouts then progress at average speeds estimated to be between $0.25-0.50$ mm/day, or $10.4-20.8 \pm 4.2$ μm/hr. More recent measurements of sprout extension speeds during angiogenesis are reported in Bautch et al. [79]. In this study, embryonic stem cells containing an enhanced green fluorescent protein are differentiated *in vitro* to form primitive vessels. Day 8 cell cultures are imaged within an $\sim$160 μm^2 area at 1 minute intervals

Table 6.1: Table of Parameters. Dimensions are given in terms of L=length, T=time, M=mass and E=energy. Unless otherwise noted, all simulations used the same parameter set and initial conditions. EC denotes endothelial cell.

Parameter	Symbol	Dimensions	Model Value
Length Scales	L_1, L_2	L	166μm, 106μm
VEGF Diffusion	D	L^2/T	3.6x10^{-4} cm^2/h [148]
VEGF Decay	λ	T^{-1}	.6498 h^{-1} [148]
VEGF Uptake	β	M/cell/T	.06 pg/EC/hr [20, 46, 168]
VEGF Source	S	M/L	.035 pg/pixel [93, 75]
Activation Threshold	v_a	M	.0001 pg
Adhesion			
EC−EC	J_{ee}	E/L	30
EC−Fluid	J_{ef}	E/L	76
EC−Matrix	J_{em}	E/L	66
Fluid−Fluid	J_{ff}	E/L	71
Fluid−Matrix	J_{fm}	E/L	85
Matrix−Matrix	J_{mm}	E/L	85
Membrane Elasticty			
EC	γ_e	E/L^4	0.8
Matrix	γ_m	E/L^4	0.5
Fluid	γ_f	E/L^4	0.5
Chemotactic Sensitivity	χ	E/conc	$1.11 \cdot 10^6$
Tip Cell		E/conc	$-1.45\,\chi$
Stalk Cell		E/conc	$-1.42\,\chi$
Proliferating Cell		E/conc	$-1.40\,\chi$
Intracellular Adhesion	α	E/L	300
Boltzmann Temperature	kT	E	2.5

for 10 hours and show sprouting angiogenesis over this period. The average extension speed for newly formed sprouts is 14 μm/hr and ranges from 5 to 27 μm/hr. For cell survival growth factor is present and is qualitatively characterized as providing a diffuse, or shallow, gradient. No quantitative data pertaining to growth factor gradients or the effect of chemotaxis during vessel growth are reported [79].

We use the above experimental models and reported extension speeds as a close approximation to our model of *in vivo* angiogenesis for quantitative comparison and validation. We simulate new sprout formation originating from a parent vessel in the presence of a diffusible VEGF field, which creates a shallow VEGF gradient. Average extension speeds are measured over a 14 hour period in a domain 100 μm by 160 μm. As was done in Bautch et al. [79], we calculate average sprout velocities

as total sprout displacement in time and measure sprout displacement as the distance from the base of the new sprout to the sprout tip. Figure 6.1 shows average sprout extension speed over time for our simulated sprouts. Reported speeds are an average of 10 independent simulations using the same initial VEGF profile and parameter set as given in Table 6.1. Error bars represent the standard error from the mean. The average extension speeds of our simulated sprouts are within the ranges of average sprout speeds measured by both Bautch et al. [79] and Gimbrone et al. [52]. Figure 6.1 indicates that average sprout extension speed changes as a function of time. Within the first two hours, speeds average $\sim 30\mu$m/hr and the new sprout consists of only $1-2$ endothelial cells. At two hours, sprouts contain an average of 3 cells and at 4 hours, there are a total of $5-6$ cells. Over time, as cells are added to the sprout, cell-cell adhesion and cumulative cellular adhesion to the extracelluar matrix start to play a role and sprout extension speeds slow. The inset in Figure 6.1 shows the geometry of the computational domain and simulated sprout development at 7.8 hours. Endothelial cells (red) migrate into the domain from a parent blood vessel (left boundary); a source of growth factor is available and diffuses from the right boundary. The space between represents the stroma and is composed of extracellular matrix fibers (green) and interstitial fluid (blue). As shown, simulated sprouts are approximately one cell diameter wide, which compares quantitatively well to reported VEGF induced vessel diameters [91, 101]. A natural result of the cell-based model is that cells exhibit rear retraction, which refers to the ability of a cell to release its trailing adhesive bonds with the extracellular matrix during migration. In moving multicellular clusters, rear retraction is a collective process that involves many cells simultaneously [45]. Collective migration, another characteristic dynamic observed during sprout growth, is also evident during the simulations.

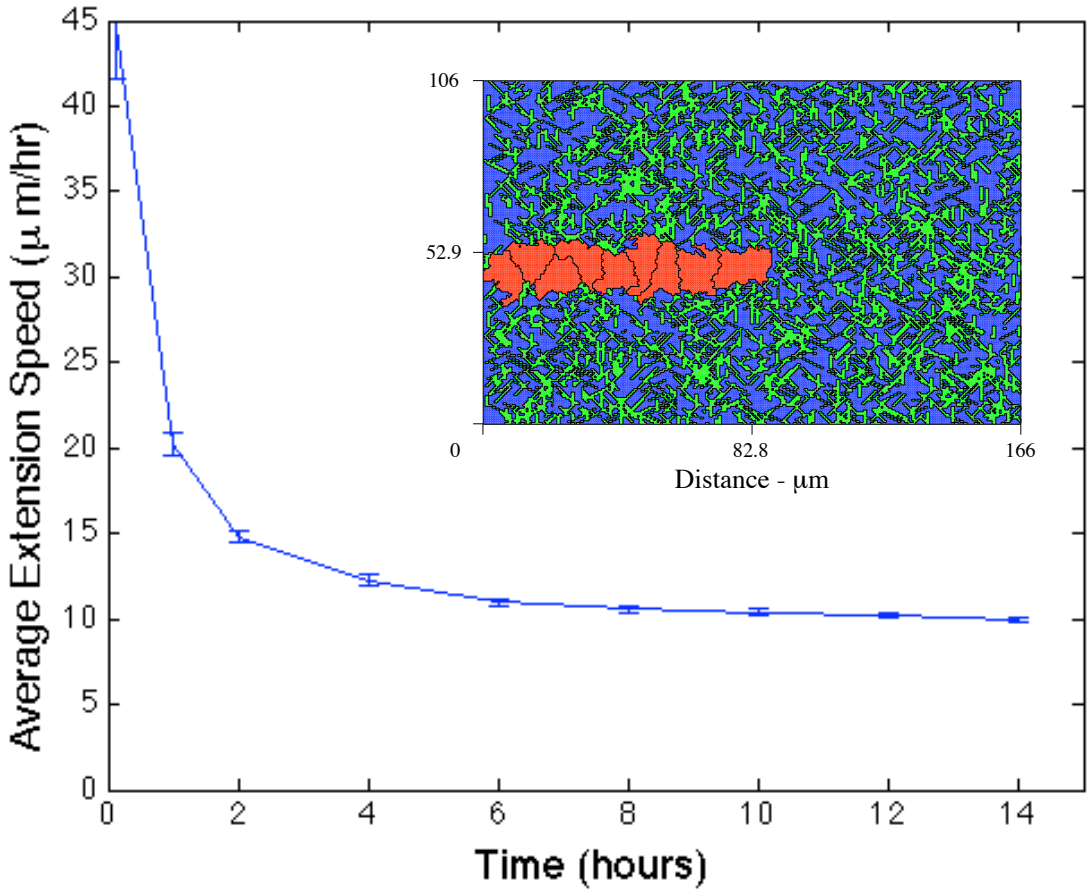

Figure 6.1: Average extension speeds of the simulated sprouts agree with empirical measurements [79, 52]. Parameters are chosen to maximize extension speeds. Reported speeds are an average of 10 independent simulations using the same parameter set. Error bars represent the standard error from the mean. (Inset) Geometry of the 2D computational domain and simulated sprout development at 7.8 hours. Endothelial cells (red) migrate into the domain from a parent blood vessel (left boundary); a source of growth factor is available and diffuses from the right boundary. The space between represents the stroma and is composed of extracellular matrix fibers (green) and interstitial fluid (blue).

On average, our simulated sprouts migrate 160 μm and reach the domain boundary in approximately 15.6 hours, before any cells in the sprout complete their cell cycle and proliferate. We do not expect to see proliferation in the new sprout because the simulation duration is less than the 18 hour cell cycle and we set the cell cycle clock to zero for newly recruited cells to simulate the very onset of angiogenesis. In our simulations, sprout extension is facilitated by cell recruitment from the parent vessel. Between 15 and 20 cells are typically recruited, which agrees with the number of cells we estimate would be available for recruitment based on parent vessel cell proliferation reported by Bautch et al. [79]. In those experiments [79], proliferation in the parent vessel is measured for day 8 sprouts, which likely has cells at various stages in their cell cycles. Proliferation in the new sprout is another mechanism for sprout extension. Thus, we consider the possibility that cells recruited from the parent vessel may be in different stages of their cell cycles by initializing the cell cycle clock of each recruited cell at randomly generated times. We observe no differences in extension speeds, sprout morphology, or the number of cells recruited as a result of the assumption made for cell cycle initialization ($t = 0$ or t random). This suggests that, in our model, stalk cell proliferation and cell recruitment from the parent vessel are complementary mechanisms for sprout extension.

By adjusting key model parameters, we are able to simulate various morphogenic phenomena. For example, by increasing the chemotactic sensitivity of cells in the sprout stalk and decreasing the parameter controlling cellular adhesion to the matrix, J_{em}, we are able to capture stalk cell migration and translocation along the side of a developing sprout. This phenomena, where stalk cells weaken their adhesive bonds to the extracellular matrix and instead use cell-cell adhesion to facilitate rapid migration, frequently occurs in embryogenesis [communication with C. Little] and

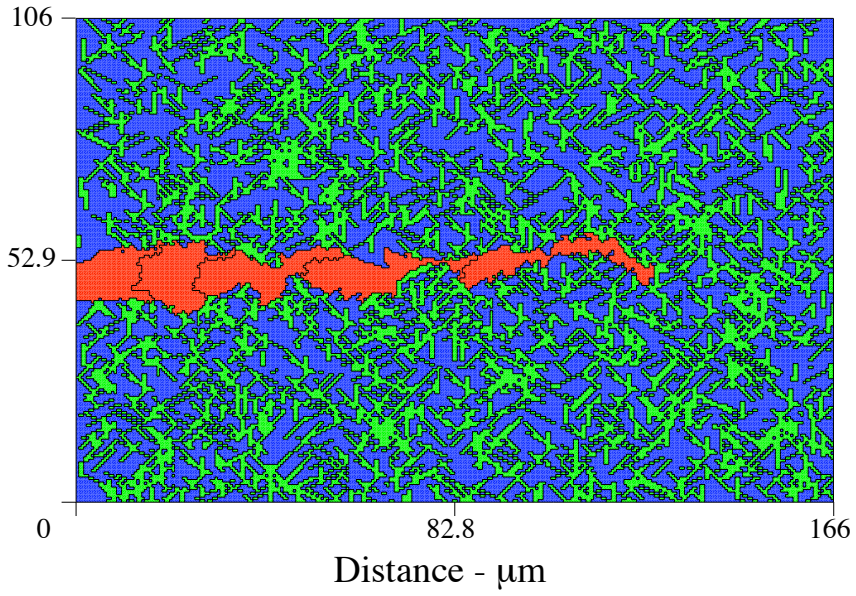

Figure 6.2: For a different parameter set, fewer cells are recruited from the parent vessel and cells elongate. Here cells are approximately 40 μm in length and the average extension speed at 14 hours is 6.8 μm/hr. $J_{\{ee,em,ef\}}$=$\{42,76,66\}$, $\chi_{tip} = 1.55\,\chi$, $\chi_{\{migr,prolif\}} = 1.45\,\chi$.

is described as preferential migration to stretched cells [28]. Figure 6.2 shows the morphology for one particular set of parameter values corresponding to weaker cell-cell and cell-matrix adhesion and stronger chemotaxis. Here the average extension speed at 14 hours is 6.8 μm/hr, fewer cells are recruited from the parent vessel, and cells elongate to approximately 40 μm in length. This length scale is consistent with experimental measurements of endothelial cell elongation [158].

Figure 6.3a shows images from experiments using human fibroblasts stained for actin (e) and tubulin (f) on micro-machined grooved substratum [121]. These experiments demonstrate that cells alter their shape, orientation, and polarity to align with the direction of the grooves (double-headed arrow), exhibiting topographic, or contact, guidance. Figure 6.3b is a simulation designed to mimic these experiments by isolating the cellular response to topographical guidance on similarly patterned substratum. In this simulation, there is no chemotaxis and no cell-cell contact; cells

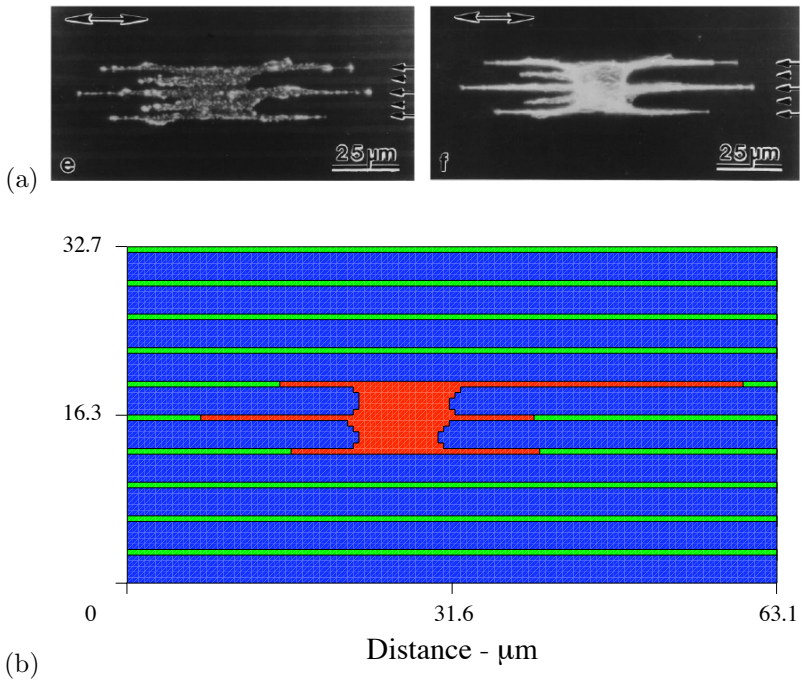

Figure 6.3: Panel (a): Fibroblasts stained for actin (e) and tubulin (f) showing that cells alter their shape, orientation, and polarity to align with the direction of the grooves (double-headed arrow). Images reprinted from Oakley et al. [121] with permission from Elsevier. Compare with panel (b), which is a simulation of the cellular response to topographical guidance on similarly patterned substratum and demonstrates the flexibility of the model to capture a variety of different morphological phenomena.

respond only to topographical cues in the extracellular matrix. Simulated cells alter their shape and orient in the direction of the matrix fibers. Figure 6.3b bears a striking resemblance to the cell shapes captured in Figure 6.3a. We are also able to simulate interstitial invasion/migration by a single cell by turning off proliferation and cell recruitment but leaving all other parameters unchanged. This is especially relevant in the context of fibroblast recruitment during wound healing and tumor cell invasion (e.g., glioblastoma, the most malignant form of brain cancer [35]), where understanding cell-matrix interactions and directed motility are critical mechanisms for highly motile or invasive cell phenotypes.

6.2.2 Model predicts ranges of matrix fiber density that may inhibit angiogenesis

We design a set of numerical experiments allowing us to observe the onset of angiogenesis in extravascular environments of varying matrix fiber density. We consider matrix fiber densities given as a fraction of the total interstitial area, ρ. As a measure of matrix orientation equivalency, the total fiber orientation in both the x and the y direction is calculated as we increase the matrix density. The total x and total y fiber orientation do not vary with changes in total matrix density. Besides varying the matrix density, all other parameters are held fixed. All simulations last the same duration corresponding to approximately 14 hours.

The average rate at which the sprout grows and migrates, or its average extension speed, is calculated as the total tip cell displacement in time. Average extension speeds in microns per hour (μm/hr) versus matrix fiber density are graphed in Figure 6.4a at various times (2, 5, 10, 14 hours) during sprout development. We identify qualitative measures to describe and differentiate between various capillary sprout morphologies, such as the thickness of the sprout, its tortuosity, and whether sprout branching or anastomosis occur. Following Bautch et al., we define a sprout branch as one or more cells that extend, or bud, from the primary sprout body at least 10 μm [79]. We report capillary sprout thickness and the incidence of branching versus the fraction of matrix fibers present in the stroma in Figure 6.4b.

Figure 6.4 demonstrates that the density of the matrix impacts the average rate at which a capillary sprout extends and the resulting sprout morphology. At very low ratios (< 0.10), the matrix fibers are sparse, disconnected filaments (Figure 6.5a). In a study of vasculogenesis using endothelial cells plated on varying densities of collagen or fibronectin, cell attachment, spreading, and tube formation were maximal on dishes of intermediate density, reported to be $100-500$ ng/cm^2 [68]. Whereas, at

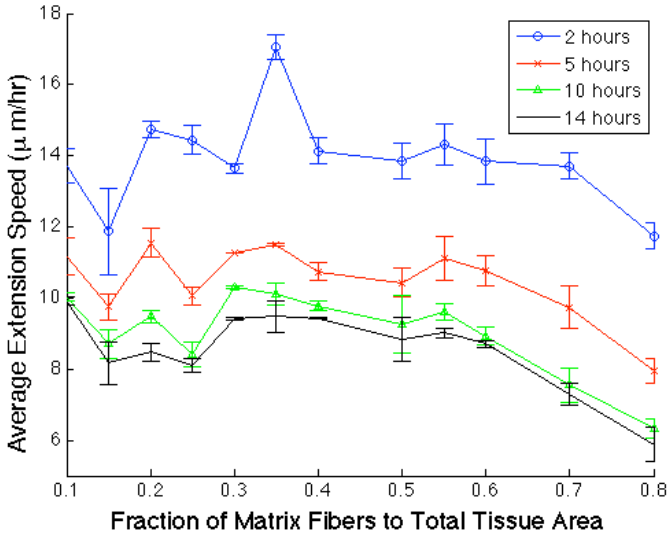

(a)

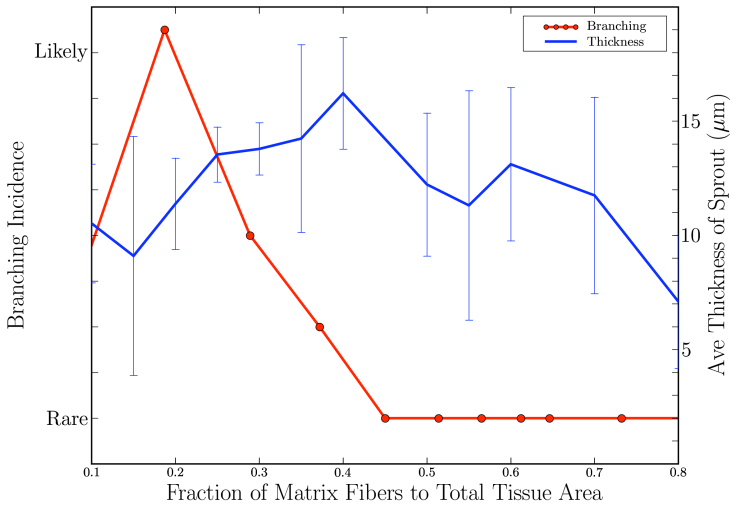

(b)

Figure 6.4: Panel (a) shows the dependence of average sprout extension speed on the density of the extracellular matrix. The model predicts that average extension speeds are maximal in the fiber fraction range $\rho = 0.3 - 0.4$. Above $\rho = 0.6$, extension speeds are significantly reduced and for $\rho < 0.1$ and $\rho > 0.8$ normal angiogenesis is interrupted suggesting that modulating matrix density may be an effective anti-angiogenesis therapy. Panel (b) quantifies morphological properties of the sprout showing sprout thicknesses in normal physiological ranges and a distinct range of fiber density conductive to branching.

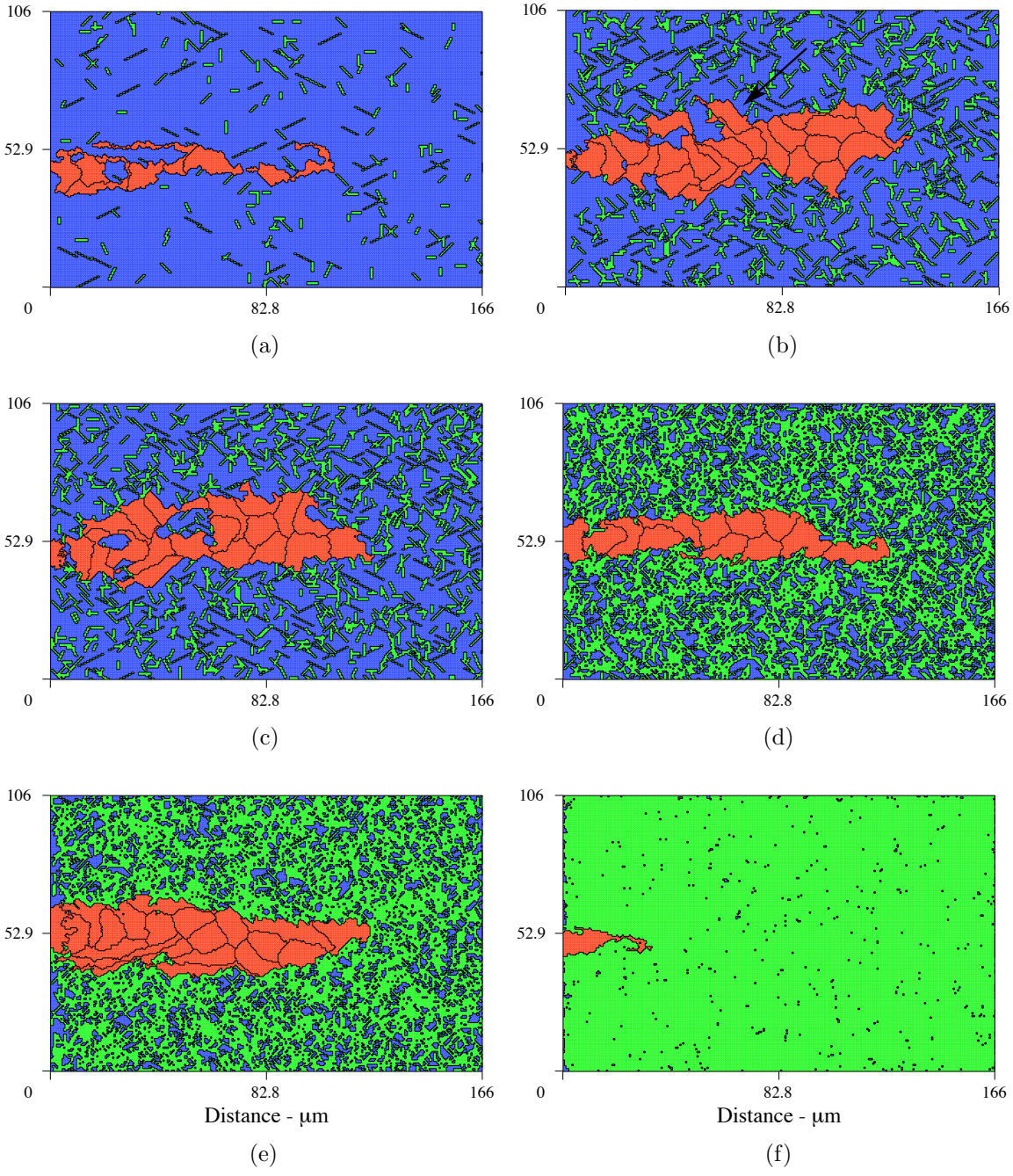

Figure 6.5: Plots showing the effect of the mechanical properties and heterogeneity of the ECM on sprout morphology and viability. Snapshots at 14 hours. From top left to bottom right: (a) $\rho = 0.05$, interruption of normal angiogenesis and loss of sprout viability; (b) $\rho = 0.2$, high matrix heterogeneity induces branching (arrow points to new branch); (c) $\rho = 0.25$, anastomosis/lumen formation; (d) $\rho = 0.6$, more homogeneous matrix fiber network produces linear sprouts; (e) $\rho = 0.7$, higher matrix homogeneity causes loss of strong guidance cues resulting in wider and slower sprout formation; and (f) $\rho = 0.99$, complete inhibition of angiogenesis at high matrix density.

matrix densities below 100 ng/cm^2, cells detached from the substrate and lost their viability [68]. Our model predicts a coincident interruption of normal angiogenesis and loss of sprout viability at very low matrix fiber densities (< 0.10). Matrices with lower fibril density transfer more strain to the cell [130]. Effects of the high transfer of strain can be seen in Figure 6.5a, which shows severe cell elongation at $\rho = 0.05$. Compare with the inset in Figure 6.1, which is an identical simulation except for an increase in the ECM density ($\rho = 0.4$). This higher density matrix transfers less strain to the cells and consequently cells are rounder. Additionally, because there are more focal adhesion sites in this denser matrix, cells are able to maintain their cell-cell contacts and develop as a cohesive body. We do not report migration speeds for $\rho < 0.1$ or $\rho > 0.8$ because sprouts show developmental defects, that is, cells are severely elongated or detach from each other and do not form a cohesive sprout body.

For $0.15 \leq \rho \leq 0.25$, the fiber network is highly inhomogeneous, and a large amount of strain gets transferred to the cells. As a result we see an increase in cell spreading and a thickening of the new sprout as compared to those morphologies seen for $\rho < 0.15$ (compare Figures 6.5a and 6.5b). These values of ρ correspond to the same fraction of collagen present in subcutaneous tissue ($\rho = 0.212$) and some skeletal muscle ($\rho = 0.09-0.189$) [94]. Remarkably, we see a distinct range of densities, $0.20-0.30$, where new buds develop from the main sprout body and branches begin to form (see arrow in Figure 6.5b). This observation suggests that mechanical mechanisms, such as a high degree of fiber heterogeneity and ECM tension transfer to cells, may promote branching and is consistent with reports that collagen matrix tension induces directional sprouting in endothelial cells [85]. Figure 6.4b quantifies the incidence of branching for and the average thickness of sprouts developing in different matrix

densities. At all densities, sprout thickness is within the normal physiological range of 1−2 cells wide. Figure 6.5c shows sprout development on a matrix where $\rho = 0.25$. Morphologies that could be interpreted as lumen formation or anastomosis (loop formation) are evident and are only seen at this density. Figure 6.4a shows (i) a clear range of matrix density that encourages sprout migration and results in faster average speeds and (ii) density ranges that present a physical barrier to migration and inhibit sprout growth and results in slower extension speeds. The peak in the graph at $\rho = 0.35$ indicates that sprout extension speeds are fastest at intermediate densities between $0.3 \leq \rho \leq 0.4$ and suggests an optimal matrix density for promoting angiogenesis. For comparison, this range of matrix density is near the physiological fraction of collagen fibers found in the cornea [94]. A possible mechanistic explanation for the existence of a peak extension velocity is that the mechanical properties of the ECM around $\rho = 0.35$ provide contact guidance cues that are aligned with chemotactic forces. Referring again to Figure 6.4a, we see that peak migration speeds are prominent at 2 hours, but are still evident, although to a lesser extent, at 10 and 14 hours. Thus, these results do not depend on time. Our finding that maximum migration speeds depend on matrix density is supported by empirical measurements of endothelial cell migration speeds on various fibronectin concentrations (0.5, 1, 5, 20, 40 μg/cm^2) demonstrating peak migration speeds at intermediate concentrations (5 μg/cm^2) [149].

As matrix density increases, the network of connected fibers is extensive. Higher fiber density translates into greater matrix homogeneity and a loss of strong guidance cues from ECM heterogeneity. Chemotaxis then plays a stronger role in sprout guidance thereby producing linear sprouts (Figure 6.5d). Consequently, we do not observe any branching at densities above $\rho = 0.35$. At a fiber density of $\rho = 0.70$,

less tension is transferred to the cells. Cells experiencing less tension are rounder. Wider and slower sprouts form at this matrix density (Figure 6.5e). Above $\rho = 0.75$, very high matrix densities actually establish a physical barrier to migration and we see a corresponding reduction in sprout extension speed due to increased focal adhesion contacts and strong tractional forces. Figure 6.5f shows complete inhibition of angiogenesis at $\rho = 0.99$ as tractional forces dominate chemotactic incentives.

6.2.3 Network connectedness and matrix fiber alignment influence sprout extension speeds

Based on our earlier observations, the density of ECM fibers affects capillary sprout migration speeds. As matrix density is increased, a connected fibrous network develops which could be a mechanism for differences in observed average speeds. We hypothesized that peak extension speeds occur when the mechanical properties of the ECM provide contact guidance cues that are aligned with the chemotactic forces. To examine the effects of matrix fiber alignment on average rates of capillary sprout elongation, we devise another set of numerical experiments. If matrix fiber alignment plays a prominent role in sprout migration, we would expect more rapid rates of sprout elongation when matrix fibers are aligned parallel to VEGF gradients than when fibers are aligned perpendicular to the gradient. We look at three specific cases: matrix fibers aligned perpendicular to VEGF gradients, matrix fibers aligned parallel to the VEGF gradient, and a combination of horizontal and vertical fibers only. We compare these test cases with the baseline simulations of sprout development on matrices of random fiber orientation. We distinguish and refer to these three cases by the angle that is formed between the fiber axis and the axis of the VEGF gradient, that is, 0° denotes a matrix with fibers aligned with the gradient and 90° identifies a matrix of fibers perpendicular to the VEGF gradient. These numerical experiments

represent a simplified replica of the matrix fiber restructuring and fiber alignment that occurs as a result of the tractional forces exerted by endothelial cells during migration [164, 85]. All matrices have the same matrix fiber density.

As matrix fiber density increases, both the number of focal adhesion binding sites available in the ECM and the connectivity of the fiber network increase. As a measure of connectivity, we consider the network connected if there exists a continuous path along matrix fibers from the parent vessel to the source of chemoattractant. As the density of matrix fibers increases, there will be a density that guarantees network connectedness. This threshold density is known as a percolation threshold. Our model fiber networks are constructed by randomly placing fibers at randomly selected but discrete orientations: $0°$, $\pm 30°$, $\pm 45°$, $\pm 60°$, and $90°$. Consequently, our fiber network most closely approximates a triangular lattice. We estimate that the percolation threshold in our fiber networks occurs between $\rho = 0.30 - 0.35$. Recall that we define matrix density, ρ, as the fraction of total tissue space occupied by collagen fibers. This can be interpreted as the probability that a matrix fiber occupies, that is, a bond exists between, two neighboring lattice sites. The bond percolation thresholds depend on lattice geometry and is 0.35 for a two-dimensional triangular lattice [43]. The matrix percolation threshold observed in our random matrices corresponds to the bond percolation threshold for a two dimensional triangular lattice. Interestingly, this percolation threshold is coincident with the density at which our model predicts maximum sprout elongation rates. We believe that this is because, at the percolation threshold, "tracks" of matrix form and provide strong contact guidance cues to the developing sprout. This finding suggests that capillary sprout extension rates are positively related to the connectedness of the network.

Figure 6.6a−c reports the average extension speed of new sprouts forming on

these restructured matrices for $\rho = \{0.2, 0.4, 0.6\}$ respectively. The baseline for comparison is the average extension speed for sprouts formed on matrices with random fiber alignment and is plotted as a solid black line in each plot. At $\rho = 0.2$, there are fewer focal adhesion sites in the ECM and the matrix fibers do not form a well connected network. Consequently, at this density, matrix fiber alignment does not have a strong effect on sprout extension speeds. At $\rho = 0.4$ and $\rho = 0.6$, sprouts achieve statistically significant higher average extension speeds when the fibers are aligned parallel to the VEGF gradient ($0°$) than when fibers are aligned perpendicular to the chemogradient ($90°$). The slowest speeds occur on matrices with fibers aligned perpendicular to the VEGF gradient. Interestingly, sprout extension speeds on a matrix composed of randomly oriented fibers are almost as fast as those observed on matrices aligned parallel to the gradient ($0°$). The reason for this is clear if we consider the vector describing the net force, or resultant force, due to fiber orientation. For $0°$ and $90°$ matrices, the resultant forces are in the $0°$ and $90°$ directions respectively. For matrices composed of fibers aligned in both $0°$ and $\pm 90°$, the resultant force is at $\pm 45°$ angles. This explains why $0°$ matrices facilitate the fastest extension speeds and $90°$ matrices the slowest. For matrices with a random fiber orientation, the resultant force is at a $\pm 11°$ angle. Since the resultant force for random matrices is approximately aligned with the gradient ($\pm 11°$), this accounts for our observation that the corresponding extension speeds are close to those speeds recorded on $0°$ matrices. In these computer generated matrices, the fibers are oriented at discrete angles and thus have a net orientation. Biologically, we are not limited to these discrete angles. Depending on the tissue type, fibers may already be aligned, for instance in muscle, or the tissue may be isotropic and lack any structural orientation. Compared to $\rho = \{0.2, 0.6\}$, the effect of matrix fiber alignment is greatest at

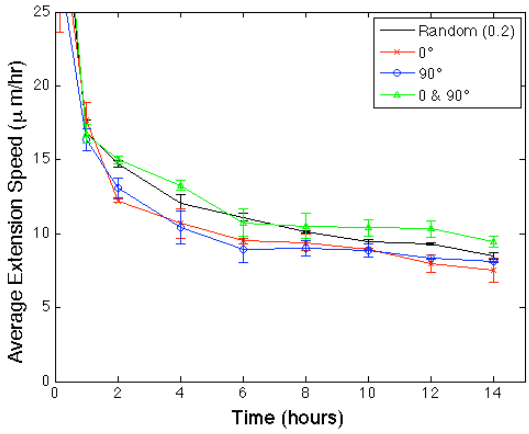

(a)

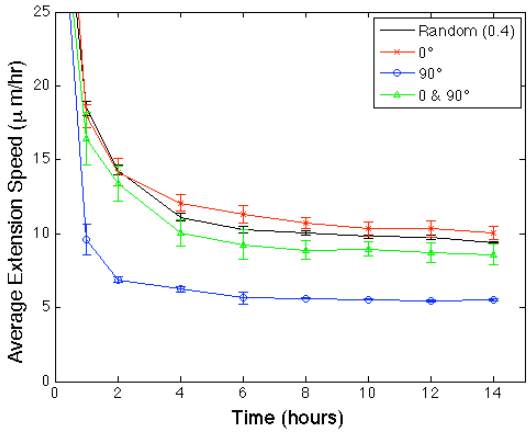

(b)

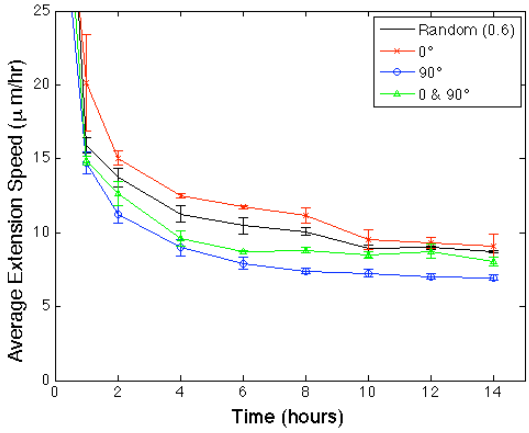

(c)

Figure 6.6: Evidence that mechanical cues, or contact guidance, from the ECM affects sprout extension. At $\rho = \{0.4, 0.6\}$, rates of sprout extension are more rapid when matrix fibers are aligned parallel to VEGF gradients (0°) than when matrix fibers are aligned perpendicular to the gradient (90°).

$\rho = 0.4$. This is because at $\rho = 0.4$ the fiber network is well connected and provides adequate focal adhesion sites, but still retains sufficient anisotropy such that strong guidance cues are transferred through fiber orientation. At higher densities ($\rho = 0.6$), even though there are ample focal adhesion binding sites, the matrix is more homogeneous, matrix "tracks" become less evident, and strong migratory cues from matrix anisotropies are lost. Consequently, the effect of matrix alignment on average extension speed decreases. These results support our hypothesis that when mechanical or contact guidance cues from the ECM are aligned with the direction of chemotaxis, these forces cooperate and promote sprout extension.

6.2.4 Cell shape and orientation are linked to matrix fiber alignment

In light of the above results, we construct patterned matrix topographies to look at the effect of unambiguous contact guidance cues on cell shape, orientation, and sprout morphology. In these numerical experiments, instead of distributing fiber bundles, we engineer matrix cord patterns that vary in width and orientation. As a baseline, we augment a matrix of randomly distributed fibers with horizontal cords 7.2 μm thick (Figure 6.7a). Figure 6.7b−e shows sprout development on matrix cords 7.2 μm thick aligned horizontally, horizontal cords 2.2 μm thick, vertical cords 2.2 μm thick, and crosshatched cords. Horizontal cords are aligned parallel to the VEGF gradient (0°); vertical cords are perpendicular to the gradient (90°); crosshatched cords form a $\pm 45°$ angle with the gradient. Except for the topography of the ECM, all other model parameters are unchanged.

We find a strong correspondence between fiber alignment and cell shape and orientation. We define cell orientation as the axis of elongation. In Figure 6.7a, the density of ambient fibers is great enough to form a well connected mesh and facilitate migration, whereas the higher density matrix cords present a physical barrier

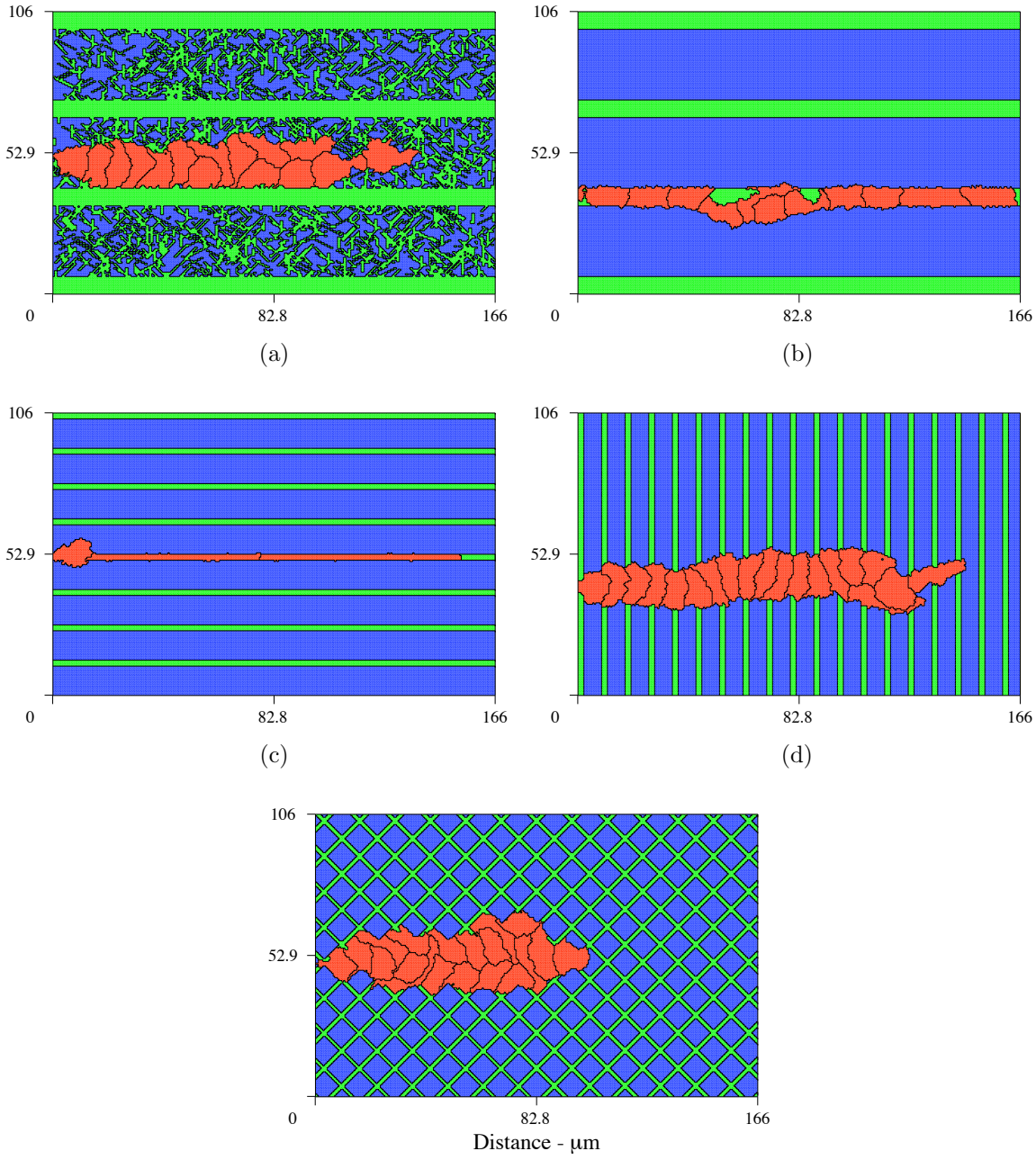

Figure 6.7: Sprouts developing on patterned matrices reveal a strong correspondence between fiber alignment and cell shape and orientation. The sprouts migrate toward higher concentrations of VEGF, however, cells elongate and are clearly oriented in the direction of the matrix cords. These results demonstrate the important role of contact guidance and tissue structure in determining cell shape and orientation. Snapshots at 12.5 hours.

that requires more energy to overcome. The anisotropy of the fiber mesh promotes variable cell shapes with no obvious cell orientation. In contrast, in the absence of an ambient fiber mesh, cells quickly adhere to the matrix cords (Figure 6.7b). Cells orient and elongate in the direction of the horizontal cords. Figure 6.7c shows the result of reducing cord thickness from 7.2 to 2.2 μm (roughly 1/2 cell diameter). Cells dramatically elongate and orient in the direction of the VEGF gradient. Compare these two cases to Figure 6.7a and notice that thinner more linear sprouts develop when strong and unambiguous contact guidance cues are aligned in the direction of chemotaxis. Next we examine the effects of matrix cords aligned perpendicular to the gradient. The results are shown in Figure 6.7d. In this case, although the sprout migrates toward higher concentrations of VEGF, cells elongate and are clearly oriented in the direction of the matrix cords, perpendicular to the gradient. Figure 6.7e depicts sprout formation on crosshatched matrix topography. Again, cells orient in the direction of the matrix cords, here at $\pm 45^\circ$ angles with respect to the gradient. The resulting morphology is a sprout approximately 2 cell diameters thick, notably thicker than the sprouts that develop with strong contact guidance cues aligned in the direction of chemotaxis (Figure 6.7b,c). Fiber orientation also modulates cell recruitment. When cells elongate and orient in the direction of the VEGF gradient, fewer cells are required from the parent vessel and sprout extension is largely due to cell elongation. Compare Figure 6.7: (a) with no obvious cell orientation 15 cells are recruited, (b) 11 cells are recruited when cells are oriented in the direction of the VEGF gradient, (c) only 3 cells are recruited when cells dramatically elongate, (d) 19 cells are needed when cell orientation is perpendicular to the chemoattractant gradient, and (e) 19 cells are recruited when cells orient at $\pm 45^\circ$ with respect to the gradient. These results demonstrate the important role of contact guidance and

tissue structure in determining cell shape and orientation.

6.2.5 Changes in average extension rates due to tip cell matrix degradation varies as a function of ECM density

During angiogenesis, endothelial cells not only realign matrix fibers, but they also secrete matrix degrading proteases that break down extracellular matrix proteins and facilitate sprout migration through the stroma [124]. To study the effect of matrix degradation on sprout development, we implement matrix degradation by allowing the tip cell to degrade $\sim 0.3\ \mu\text{m}^2$ of matrix each minute. We choose this rate of degradation based on the fact that focal adhesions are estimated to be 0.25 μm^2 [152]. Average sprout extension speeds are recorded and compared with the average extension speeds without matrix degradation for different matrix densities. Figure 6.8 graphically represents average extension rate pairs for sprouts forming with and without matrix fiber degradation at $\rho = \{0.2, 0.4, 0.7, 0.975\}$ and shows that the effect of matrix degradation depends on matrix density. At $\rho = 0.7$ and $\rho = 0.975$, matrix degradation results in approximately a 37% increase in average sprout extension speeds at hour 14. As matrix fibers are degraded, fewer cell-matrix adhesion sites are bound and therefore cellular attachment is reduced resulting in increased motility. At a matrix density of $\rho = 0.4$, tip cell matrix degradation only seems to have a significant influence on extension speed at earlier times (0−5 hours). This suggests that the increase in motility due to a loss of bound focal adhesion sites is limited. On more sparse matrices, $\rho = 0.2$, matrix degradation actually slows sprout extension. While this may seem counterintuitive, at lower densities, further reducing fiber density reduces the effectiveness of the ECM to provide a cellular support system that is necessary for normal sprout migration and formation. Thus, depending on the density of the matrix, matrix degradation may result in faster or

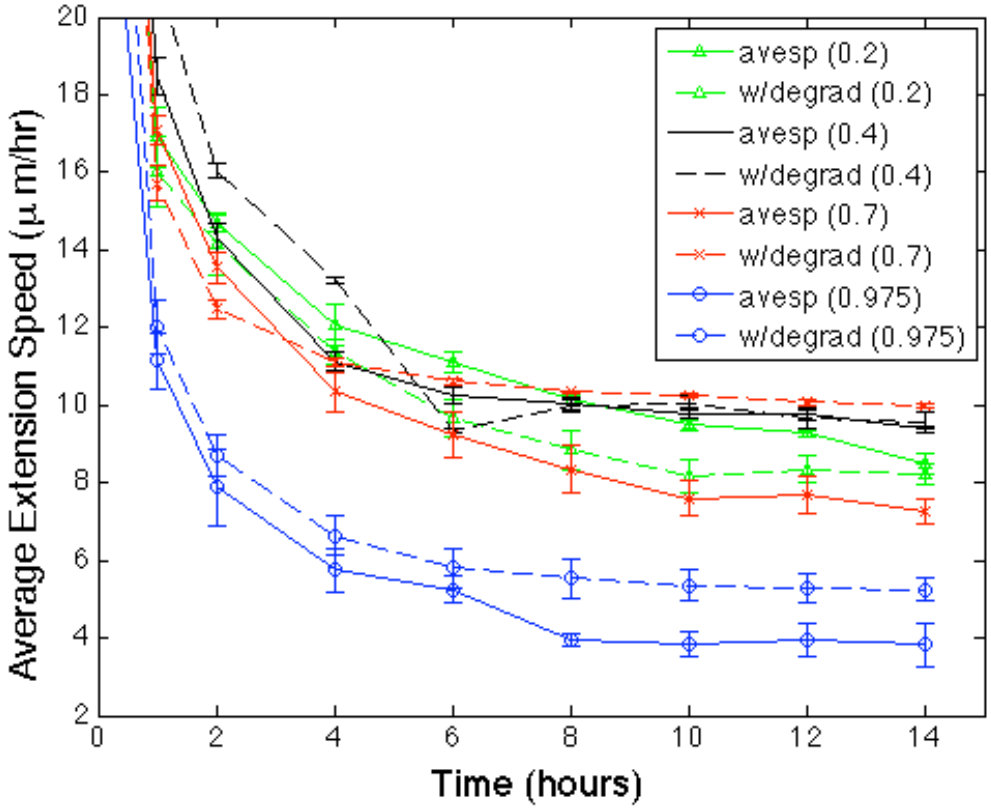

Figure 6.8: This plot shows that the effect of matrix degradation on average sprout extension speeds depends on the density of the ECM. Solid lines represent average extension speeds without matrix degradation and the corresponding colored dashed lines show average speeds with tip cell matrix degradation. For $\rho \leq 0.25$, matrix degradation has anti-angiogenic effects. Above $\rho = 0.4$, degradation facilitates sprout progression.

slower extension speeds. This is consistent with our finding that sprout extension speeds vary as a function of matrix density (Figure 6.4a). Indeed, at $\rho = 0.975$, the initial cell is not able to penetrate the stroma and angiogenesis is completely inhibited. In otherwise identical simulations, however, when the tip cell actively degrades the matrix fibers, the tip cell carves out a path through the ECM and a sprout is able to form (Figure 6.9a). This result is empirically validated by very recent experiments by Davis et al. showing that human endothelial cells in extracellular collagen matrices degrade a path through the ECM. This path is referred to as a vascular guidance tunnel [33]. Figure 6.8 also shows that for $\rho = 0.7$, tip cell matrix degradation has the greatest effect after 10 hours.

In our model, without degradation we observe no branching at matrix fiber densities above $\rho = 0.35$. Figure 6.9b shows the progress of sprout development at 14 hours with ECM degradation at $\rho = 0.4$. A new sprout branches from the primary sprout body, an event that emerges only as a result of featured cellular and molecular level dynamics; no rule specifically incorporating branching is imposed. Tip cell degradation reduces ECM density and sets up very high local anisotropies in the matrix fiber structure, providing strong contact guidance cues to the developing sprout. This result provides additional support for our hypothesis that high matrix anisotropies created by tip cell degradation may be a mechanism for sprout branching.

6.2.6 Sensitivity analysis

To ascertain the variability or sensitivity of our results to the choice of parameters, we vary one parameter at a time (holding fixed all other Table 6.1 parameters) and record our observations. We look at sprout development for various J_{ee}. Decreasing J_{ee} is equivalent to increasing the strength of the bond between endothelial cells and

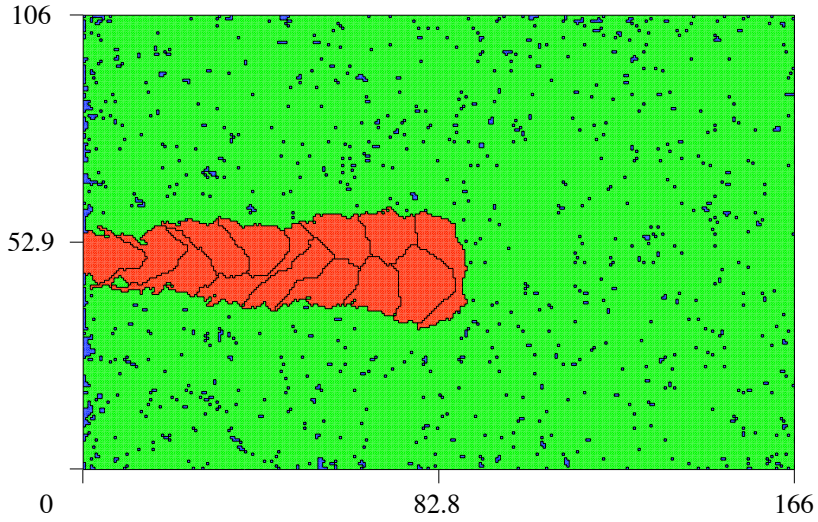

(a)

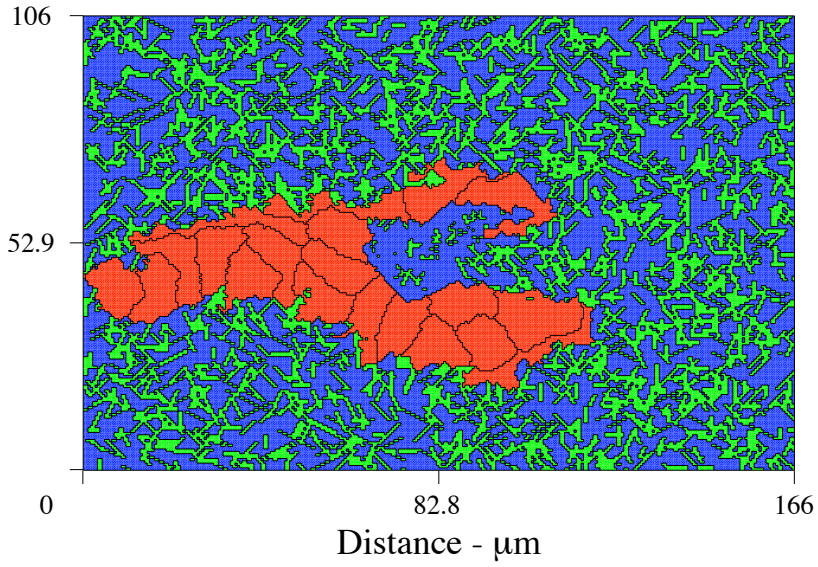

(b)

Figure 6.9: Without degradation, angiogenesis is inhibited at $\rho = 0.99$ (Figure 6.5f). Panel (a) shows that tip cell matrix degradation promotes sprout development at $\rho = 0.99$ by carving out a path for migration. Panel (b) depicts sprout formation with ECM degradation at $\rho = 0.4$ and suggests that high matrix anisotropy created by tip cell degradation may be a mechanism for branching. Snapshot at 14 hours.

the cells move to increase their cell-cell contact area. For $J_{ee} \leq 10$, cell shapes are grossly contorted and unrealistic. As J_{ee} increases, cell-cell adhesion weakens. Cells move to reduce their surface area contact with each other and are generally rounder. For $J_{ee} \geq 50$, cell-cell adhesion becomes too weak relative to the chemotactic forces acting on the cell and the tip cell migrates away from the main sprout. Similarly, lower values of J_{em} correspond to stronger cell-matrix binding energies. For $J_{em} \leq 46$, cell shapes are abnormally distorted to increase the contact area between the matrix fibers and the cell membrane. At $J_{em} = 56$, a relatively strong cell-matrix adhesion bond, sprout morphology is noticeably thicker and more tortuous. Intermediate values ($66 \leq J_{em} \leq 76$) provide a good balance between contact guidance and release of focal adhesion bonds and sprout morphologies and extension speeds are relatively insensitive to parameter variability within this range. Above $J_{em} = 76$, contact guidance is weak. A value of $J_{em} = 200$ is equivalent to inhibiting cell-matrix adhesion, for example by blocking integrin receptors. Consequently, at $J_{em} = 200$, endothelial cells do not adhere to matrix fibers at all and are unable to migrate, even in the presence of chemotatic incentives. In this case, chemotaxis is the dominant force governing sprout guidance and more linear sprouts develop. There is no statistically significant change in average extension speeds as J_{em} varies within these ranges. The results are insensitive to the binding energies between matrix fibers, J_{mm}, or between interstitial fluid molecules, J_{ss}. The results also do not depend on the compressibility properties of the matrix fibers or interstitial fluid, $\gamma_{m,f}$, since the total mass of these ECM components are conserved. We vary γ_e between 0.3 and 3. Decreasing γ_e makes it easier for the cells to deviate from their target volume. Therefore at $\gamma_e = 0.3$, the cells are larger overall and consequently fewer cells are recruited from the parent vessel. Average extension speeds are not affected. This highlights that cell growth

is another mechanism for sprout extension. Increasing γ_e produces smaller cells, and consequently, more are recruited. At $\gamma_e = 3$, the tip cell migrates away from the main body of the sprout. This is because of the chemotactic sensitivity differential between the tip cell and the stalk cells. The relative pressure on a cell to maintain its target volume is greater than the chemotactic forces acting on the stalk cells, but not greater than the chemotactic incentives for the tip cell. Thus the tip cell detaches.

Figure 6.10 shows how the average extension speed of a sprout varies with increasing χ. Average speeds are calculated at 14 hours. Above $\chi = 1.6 \cdot 10^6$, the physical integrity of individual endothelial cells is compromised and the cells dissociate due to the relatively strong chemotactic forces. Below $\chi = 1 \cdot 10^4$, chemotactic forces provide insufficient migratory cues relative to the adhesion energies and growth constraint and the initial cell does not migrate into the stroma. At intermediate values, sprouts migrate faster with increasing χ, but sprout morphologies are unaffected. To determine the effect of change in the probability that energetically unfavorable events occur, we vary the parameter kT, where k is the Boltzmann constant and T is the effective temperature that corresponds to the amplitude of cell membrane fluctuations. Increasing kT effects faster average sprout extension speeds, but no noticeable changes in cell shape, the number of cells recruited, or sprout morphology.

6.3 Discussion

The extracellular matrix has attracted a great deal of attention from researchers and experimentalists because of its vital role as a modulator of morphogenic processes. Identifying and elucidating the mechanisms through which the ECM contributes to changes in cell shape and function is of critical importance to many

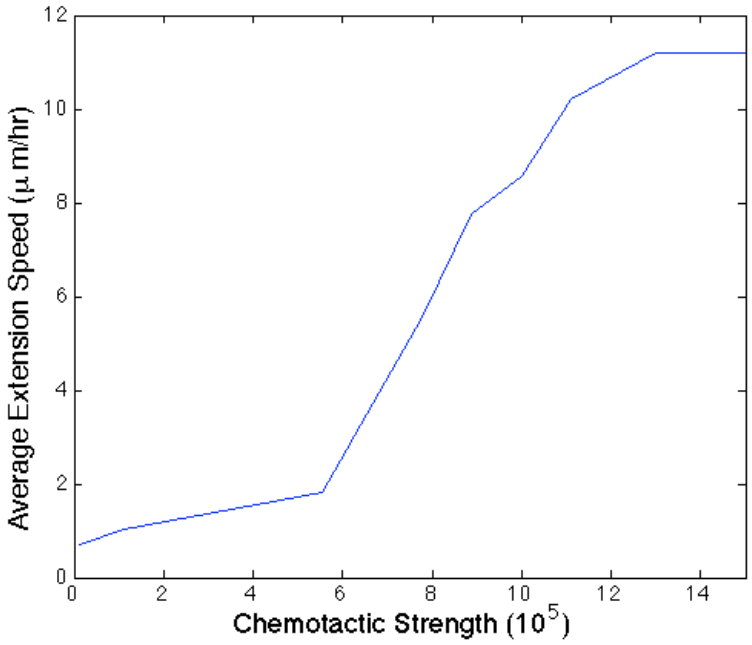

Figure 6.10: Plot showing the effect of varying the chemotactic sensitivity parameter, χ, on average sprout extension speed at 14 hours. Below $\chi = 1 \cdot 10^4$ chemotactic forces are not strong enough relative to the energies associated with adhesion and growth to induce motility. Above $\chi = 1.6 \cdot 10^6$, chemotactic forces are strong enough relative to adhesion and growth that the cells dissociate.

morphogenic events, including angiogenesis, wound healing, embryogenesis, and tumor invasion. We use a cell-based model of angiogenesis as a framework to explore the effects of ECM topography on cell-cell and cell-matrix dynamics. This type of modeling approach captures the precise morphology of the cells and of emergent multi-cellular structures and allows a quantitative description of physical characteristics, such as cell shape and orientation and sprout thickness. By adjusting key parameters, the model captures (i) a frequent observation in embryogenesis whereby cells use cell-cell adhesion to rapidly traverse along the sprout, (ii) single cell migration as seen in fibroblasts during wound healing, and (iii) different cell shapes. Our results indicate that the density or connectedness of the matrix, local proteolytic matrix degradation, and fiber alignment affect extension speeds. We record peak migration speeds in tissues that have a similar collagen content to that seen in the cornea. We observe density dependent pro- and anti-angiogenic effects and propose that high matrix fiber anisotropy provides strong contact guidance cues and is a mechanism for initiating sprout branching. Finally, we provide strong evidence that contact guidance influences cell orientation by examining sprout development on engineered matrix patterns.

During morphogenesis, cells actively restructure and condition the extracellular matrix for migration through proteolytic degradation and fiber reorganization and alignment [160]. Our studies suggest that contact guidance cues are mediated by changes in matrix fiber density and isotropy, network connectedness, and fiber orientation. These findings collectively support the hypothesis that contact guidance cues play a major role in determining sprout morphology and the average rate of capillary sprout extension. Our results strongly suggest that the contact guidance cues established through high matrix fiber inhomogeneity in the stroma may be a mech-

anism for sprout branching. Applying our results in the context of tumor-induced angiogenesis, local changes in ECM density that create matrix anisotropies in concert with fiber alignment may contribute to the accelerated extension speeds reported as sprouts approach the tumor. In addition, fiber density is not constant in the extratumoral environment. The density of the extracellular matrix is lower near the tumor due to the secretion of matrix degrading proteases by tumor cells. If these lower regions of matrix density are within the range we predict to be conducive to branching, this could help explain why an increase in branching, known as the brush border effect, is seen *in vivo* as sprouts get close to the tumor. It is worth pointing out that at a distance of 100 μm from a tumor 1mm in diameter, we specify a linear source of VEGF. This choice ensures little or no gradient in the transverse or y−direction and allows us to attribute lateral cell and sprout movement to the mechanical effects of the matrix. Different spatial profiles of VEGF, for example a parabolic source or local sinks and sources of VEGF in the ECM, could also contribute to branching and varied morphological patterns. The effect of different VEGF profiles on angiogenesis has been theoretically modeled by Anderson and Chaplain [9].

6.3.1 Clinical implications: ECM targeted angiogenic therapies

Increased understanding leading to the ability to control angiogenesis *in vivo* has significant clinical implications. Angiogenesis is a crucial event to many physiological processes. Embryonic development and endometrium vascularization, arteriogenesis resulting from ischemia and vessel occlusion, wound healing and tissue repair are all homeostatic processes that require new vessel growth for normal function. Angiogenesis can also lead to pathological conditions. Tumor angiogenesis, proliferative diabetic retinopathy and macular degeneration, psoriasis and rheumatoid arthritis occur when angiogenesis is unhalted [47]. On the other hand, insufficient vessel

growth can lead to heart attack, stroke, and impaired ulcer and wound healing. Existing angiogenic therapies can be broadly categorized as those that (1) target growth factors or growth factor cell receptors that stimulate vessel growth, (2) block cell invasion into the stroma, and (3) directly induce endothelial cell apoptosis. Because of its established prominence in both homeostatic and aberrant angiogenesis, VEGF and its receptors are prime therapeutic targets. There is overwhelming experimental evidence that in order to form functional vessels, the various VEGF isoforms must be precisely regulated and that the blockage of even a single growth factor might limit tumor-induced vascular growth [124, 20, 50]. The most promising approaches to anti-angiogenesis therapies are those based on blocking VEGF or VEGF receptors [171]. VEGF neutralizing antibodies, soluble VEGF receptors, and receptor tyrosine kinase inhibitors are examples of therapies currently being utilized or that are undergoing clinical trials [81]. One problem associated with targeting growth factors as therapeutic agents is that they are often constitutively expressed *in vivo* and can be proteolytically released. Thus tight control is, in practice, hard to maintain. For example, it is known that connective tissue, which contains some of the same fibrous proteins that are found in the ECM, can significantly inhibit cell migration and prevent the formation of sprouts [124].

The ECM and cell-matrix associations also provide promising possibilities for angiotherapy, but have only more recently received attention as targets and are in less advanced stages of clinical development. Consequently, modeling and simulation have the potential to contribute to and propel further advancement. Current therapeutic interventions aimed at cell-matrix interactions during angiogenesis focus on tissue inhibitors of metalloproteinases and on integrin-mediated cellular adhesion [47]. Blocking proteolysis is intended to inhibit cellular migration into the stroma and

to prohibit MMP-dependent release and activation of ECM sequestered angiogenic factors. The $\alpha v\beta 3$ integrin receptor is significantly upregulated in angiogenic vessels when compared to mature vessels [47], making this receptor a logical therapeutic choice.

Using our model, we regulate cell-matrix binding affinity (J_{em}) and control the number of focal adhesion binding sites available in the ECM (density modulation) to test the efficacy of integrin specific anti-angiogenic therapies. Setting $J_{\text{em}} = 200$ is equivalent to blocking integrin receptors. Our simulations show that decreasing the binding affinity of integrin receptors prevents endothelial cells from adhering to matrix fibers and cells are unable to migrate even in the presence of chemotatic incentives. We also show that cellular motility is inhibited at high matrix densities due to the greater number of focal adhesion binding sites available. Our simulations suggest that regulating the affinity or number of cell-matrix focal adhesion sites either biochemically or mechanically produces anti-angiogenic effects. In addition, our results indicate that regulating the cellular production of matrix degrading proteases can shift sprout velocity curves for the purpose of promoting or inhibiting angiogenesis. We show that at low matrix densities ($\rho \leq 0.25$), matrix degradation has anti-angiogenic effects, whereas above $\rho \leq 0.4$, degradation facilitates sprout progression.

In these studies, we isolate and examine variations in fiber density and structure, and proteolytic matrix degradation as independent mechanisms that control vascular morphogenesis. Nonetheless, the integrin, protease, and growth factors systems are highly connected and provide regulatory feedback for each other [47]. Thus, there is still a need for more in depth investigations on the relationship between extracelluar stimuli and cellular function. In particular, studies focusing on intracellular

signaling and cross-talk between the integrin and growth factor receptors are of key importance.

CHAPTER VII

Intracellular Signal Transduction and Its Role in Controlling Cellular Behavior During Angiogenesis

7.1 Introduction

Another step towards understanding and controlling the processes that occur during angiogenesis is to understand how individual cells respond to the biochemical signals that come from their external environment, including chemo-activation and messages from other cells and the extracellular matrix, to make decisions. Creating a model framework to study the cellular response during angiogenesis is a major goal of this dissertation. This investigation would be incomplete without consideration of the intracellular signal transduction pathways that regulate how and when a cell responds to key external biochemical signals involved in angiogenesis, and the influence of these environmental signals on cellular function. To do this, we construct a Boolean network model that focuses on those pathways and molecular targets affected by growth factor binding to receptor tyrosine kinases (RTK), ligation of integrin receptors (ITG), and cell-cell communication via vascular endothelial (VE) cadherins. To date, there is no mathematical model, Boolean or otherwise, designed to investigate the cross-talk between the VEGF, integrin, and cadherin receptors in deciding cellular behavior during angiogenesis. With this model we can investigate questions such as: what are the critical pathways involved in how a cell decides

whether its going to grow, move, or die once environmental signals are received; and how does a cell's external environment influence these decisions? These questions will be explored in Chapter VIII where we couple this intracellular signaling network model with the cellular model of angiogenesis from Chapter VI in a multi-scale model of tumor-induced angiogenesis.

7.2 Review of Boolean Network Models

Boolean networks (BN) have a long standing tradition as idealized models of genetic regulatory dynamics in cells. Random Boolean networks (RBN) are Boolean networks with randomly assigned interactions and logical functions. Given the fragmented knowledge of gene regulation circuits at the transcription level in the 1960's, Stuart Kauffman originally introduced the notion of RBN to study the dynamical properties of gene regulation networks from a global perspective [76, 77]. In general, a BN model consists of N binary state variables $s_1, s_2, \ldots, s_N$, or nodes. Each can take the values 1 and 0, corresponding to an "on-off" idealization of regulatory dynamics, for example whether or not particular genes are expressed or the presence or absence of signaling molecules in the cell cytoplasm. The state of each node s_i, where $i = \{1, \ldots, N\}$, is regulated by k other regulatory elements (node inputs), with $0 \leq k \leq N$, and s_i can influence $0 \leq j \leq N$ other elements (node outputs). Once each node has been assigned a set of inputs, $(s_{i_1}, s_{i_2}, \ldots, s_{i_k})$, network dynamics are typically given by synchronous updating of all network elements according to

$$s_i(t+1) = f_i\left(s_{i_1}(t), s_{i_2}(t), \ldots, s_{i_k}(t)\right), \tag{7.1}$$

where f_i is the Boolean function for node s_i. In RBN, f_i is chosen at random from the ensemble of all possible 2^k Boolean functions of k inputs. For any initial configuration of the N state variables, it takes the network a maximum of $2^N - 1$ time steps to

settle to a periodic attractor of self-repeating states [77]. Two distinct dynamical phases exist in RBN: an *ordered* phase, characterized by a small number of attractors with short periods and a vanishing sensitivity to perturbations, and a *chaotic* phase with both the number and average period of attractors growing exponentially with N and perturbations (damage) propagating over the whole network [77, 36]. Of special interest are *critical* RBN, which lie at the boundary between the two phases [77, 36], as they exhibit the most realistic dynamical properties as models of biological networks with respect to robustness and adaptive flexibility [77, 5].

RBN with either a constant number of inputs per node (homogeneous topology) or with the number of inputs and outputs per node distributed according to a Poisson distribution, and equal probability for each possible Boolean function to occur, exhibit a percolation transition at a critical (average) connectivity $K_c = 2$ [36, 153, 103]. Random networks of discrete neural threshold gates exhibit a similar percolation transition behavior [88, 87, 132, 131]. If Boolean functions are biased, such that output states $s_i = 1$ occur with probability p and $s_i = 0$ with probability $1-p$, the critical value for connectivity generalizes to $K_c = 1/\{2p(1-p)\}$ [36]. Beyond this mean field theory, recent research has revealed very complex scaling phenomena at K_c [140, 162, 114, 141, 159]. In most studies, RBN dynamics are modeled using synchronous deterministic updates. Since in real biological networks stochastic events at the molecular scale are ubiquitous, asynchronous and stochastic updating schemes attract considerable attention from researchers. In randomly generated networks, dynamical attractors are often destroyed by asynchronous updates [51]. However, in models of biological networks treated as Boolean systems, attractors are often insensitive to these perturbations. This indicates that evolution might have selected network topologies such that the dynamics are robust against both noise

and different time scales of regulatory events [3, 17]. Furthermore, there is evidence that delays in information propagation contribute significantly to synchronization and thereby stabilize dynamical attractors [83, 84].

RBN have been applied in a number of theoretical studies to gain insight into the shaping of biological regulation networks by evolutionary processes, with emphasis on robustness of expression patterns against mutations of regulatory wiring [16], evolution of homeostatic regulation near percolation criticality [15], and application to problems in morphogenesis [71, 133]. BN models have also been successfully applied to model and predict the regulatory dynamics of several biological organisms, integrating known exerimental data about the topology of the corresponding cellular networks. Albert and Othmer [3] studied the segment polarity network of *Drososphila melanogaster* and showed that the topology of regulatory interactions alone predicts the observed gene expression pattern at a late developmental stage. Confirming earlier results about the extreme robustness of this developmental module against variations of kinetic constants over orders of magnitude [166], dynamical attractors in this system are insensitive to large variations of time scales in the Boolean update scheme (e.g. synchronous deterministic vs. asynchronous stochastic updates) [24]. Similar results were established in BN models of the yeast cell cycle network in the presence of biochemical stochasticity [17, 31].

Most interesting for the study presented in this chapter is the recent work of Li, Assmann, and Albert on Boolean models of signal transduction networks [97]. In most signal transduction systems, quantitative information on the speed and duration of biochemical reactions, the initial or resting state of internal nodes, and signal transduction noise is scarce. This work presents and validates a Boolean network model of signal transduction in plant guard cells as a theoretical tool that can be

useful when more quantitative information does not exist. The authors analyze the robustness of the network and show that the topology of the signaling network determines the dynamic behavior of the system. This model is used to examine the relationship between signal and cell function and to make predictions about unknown or incompletely understood biochemical relationships in the network. This type of model can be employed to describe signal transduction networks in other biological systems where mostly qualitative data are available. We use this Boolean network approach to model and analyze the signaling pathways believed to be critical to cellular regulation and function during angiogenesis.

7.3 VEGF-Integrin-Cadherin Receptor Cross-Talk: A Boolean Network Model

This study is the first to propose a network model that highlights the cross-talk between growth factor, integrin, and cadherin receptors in angiogenesis. Figure 7.1 graphically represents the signal transduction network we have implemented for this study. Arrows indicate an activating effect, whereas bars designate inhibition. Since reaction rates for most of the kinetic interactions are not available in the experimental literature, we employ a Boolean network model approach and later, in the section on dynamical analysis, investigate whether a Boolean approach provides a reasonable description of the dynamics. This network was developed with the aim of synthesizing the empirical data available for endothelial cell signal transduction during critical angiogenic processes using the sparsest graph consistent with all experimental observations. This model allows us, for the first time, to explicitly derive an input/output table linking key environmental cues to cell phenotype during angiogenesis. Using this model, we also study the effect of different feedback schemes between Rac1 and Rho, key mediators of cell migration whose relationship is not

yet well understood. We systematically analyze the dynamical stability of this network and find that the output states (i.e., cell phenotypes) are insensitive to initial configurations and perturbations of internal nodes. At the same time, this network exhibits a fast and flexible response to external signals. Further, network response is stable under stochastic desynchronization of updates and moderate internal noise, indicating that the network architecture is selected for high reliability of response in a fluctuating environment.

The assignment of appropiate Boolean functions is relatively straight-forward and the dependence relation for each node is given in Table 7.1 with references. Numbers refer to nodes and s_i denotes the state (0 or 1) of node $i = \{0, \ldots, 22\}$ at time $(t-1)$. A zero indicates the signal is off and a one indicates the signal is on. The internal nodes are initialized to $s = 1$ with probability $p = 0.5$ otherwise the node assumes $s = 0$. The current state of the network is stored in a one-dimesional array s_{curr}. As time advances, new states for each node are calculated in parallel according to the Boolean dependence on its inputs (synchronous update) and are stored in a one-dimesional array s_{new}. Then, $s_{\text{curr}} = s_{\text{new}}$ for all $i = \{0, \ldots, 22\}$.

In the graphical screenshots of the simulations (for example Figure 7.3), time runs from top to bottom and the columns represent the states of network nodes, with black = off (0), and colored = on (1). The colors correspond to the color coding of the nodes in Figure 7.1, which were chosen to highlight the signaling cascades that lead from each receptor to the different cellular phenotypes. In Figure 7.1, green nodes designate a signal that originated from activation of the VEGF receptor and the red nodes identify a signal cascade from the integrin receptor. Yellow designates nodes that can be activated from either receptor. The input signals are shown in the three leftmost columns, from left to right: the input from cell-cell adhesion

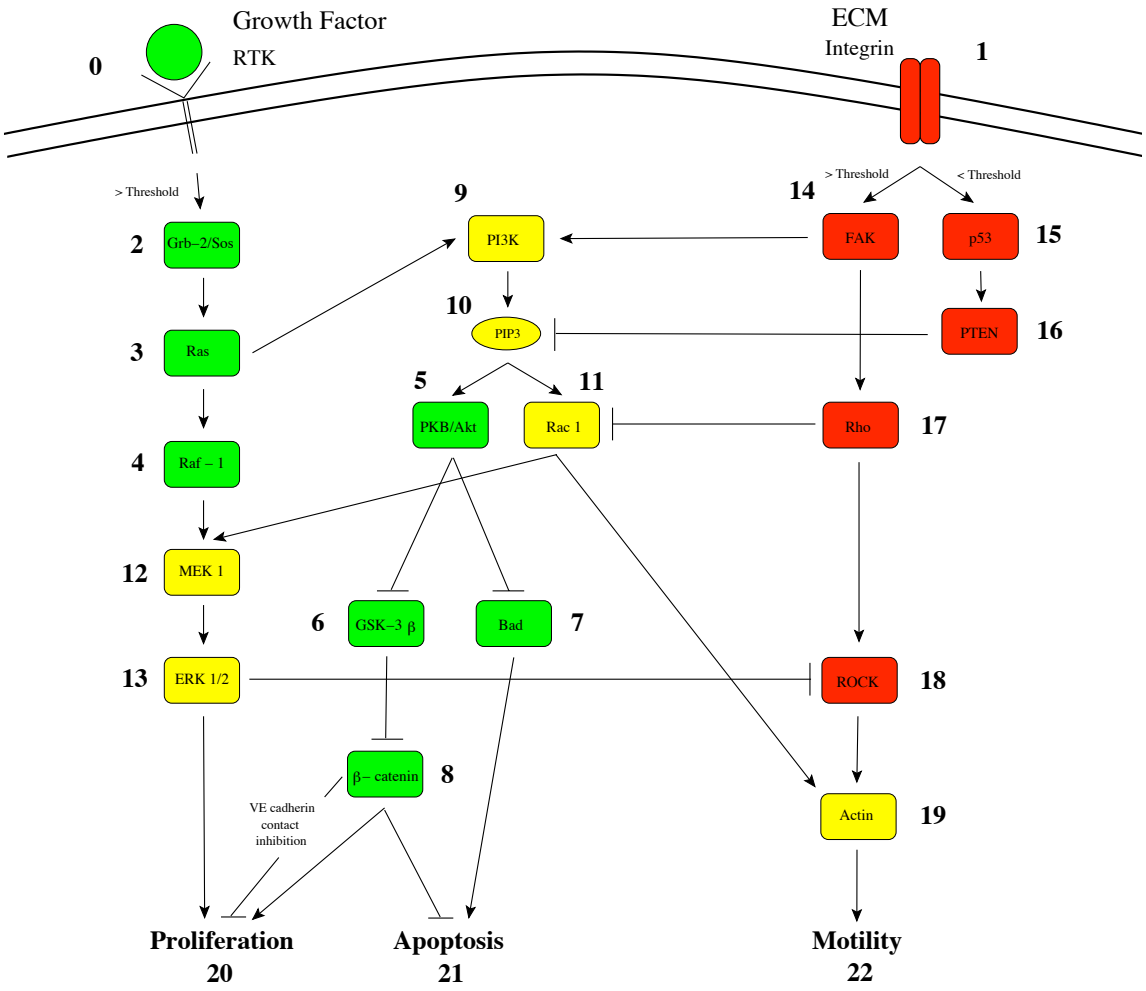

Figure 7.1: Simplified signal transduction network linking external stimuli to a cell's internal decision making machinery. This network highlights the relationship between VEGF, integrin, and cadherin receptors, allowing for cross-talk between the three to ultimately decide the cell's fate. In this network, an arrow between nodes signifies activation and a bar shows an inhibitory effect.

Table 7.1: Table of Boolean Network Interactions. Numbers correspond to nodes in Figure 7.1 and the node's Boolean dependence on other nodes is given. For instance, node #2 is turned on if node #0 is on and node #8 is turned off if node #6 is on. Nodal relationships are determined based on the current scientific literature and references are given. Most of this information is derived for endothelial cells, but data from other cells lines are included where information on the endothelial cell line is lacking.

Node #	Dependence Function	Reference
-1	external signal (VE-cadherin contact inhibition)	
0	external signal (VEGF binding)	
1	external signal (integrin binding)	
2	s0	
3	s2	[173]
4	s3	[27]
5	s10	[30]
6	NOT s5	[30]
7	NOT s5	[27]
8	NOT s6	[30]
9	s3 OR s14	[30, 136, 27]
10	s9 AND NOT s16	[123, 92]
11	s10 AND NOT s17 (< threshold) / OR if (> threshold)	[143, 92, 119]
12	s4 OR s11	[38]
13	s12	[27]
14	s1	[1]
15	NOT s1	[70]
16	s15	[157]
17	s14	[122]
18	s17 AND NOT s13	[70]
19	s18 OR s11	[6, 80]
20	s8 OR s13	[89]
21	s7 AND NOT s8	[30]
22	s19	[127]

that signals contact inhibition is depicted in gray, followed by the VEGF receptor signal (green) and the integrin receptor signal (red). The resulting phenotypes, or attractors, appear in the three rightmost columns (20-22), from left to right: proliferation, apoptosis, and migration, and are colored yellow.

7.4 Results

7.4.1 Cellular phenotype linked to external cues

This model allows us, for the first time, to explicitly derive an input/output (IO) table linking key external cues to cell phenotype. Figure 7.2 shows the model prediction of cell phenotype for various input signals. The input configuration is labeled across the top and the net signal to Rac1 (above or below some threshold amount) is given on the left. The bottom two rows show the effect of contact inhibition on cell phenotype regulation. For example, if the cell only receives a signal from its growth factor receptor (10), and the signal to Rac1 is above (>) the threshold amount needed to activate Rac1, row 2 column 3 of Figure 7.2 tells us that the cell will initiate apoptosis. The network output is (011), which indicates that, under these conditions, intracellular signaling cascades result in apoptosis and motility. We assume, however, that in the absence of any signal inhibiting apoptosis (promoting cell survival), the signal for apoptosis dominates and overrides the signal for a cell to move [49].

We verify three control cases: no external signal, VEGF signal only, and integrin signal only. From column 1 of Figure 7.2, we see that in the absence of any growth factor or integrin receptor signal, apoptosis is triggered and the cell dies. With a signal from the growth factor receptor only (column 2), again, the cell initiates apoptosis. This says that growth factor is not enough to sustain cell viability; attachment to the ECM is necessary. This result is known as anoikis, which is cell death triggered

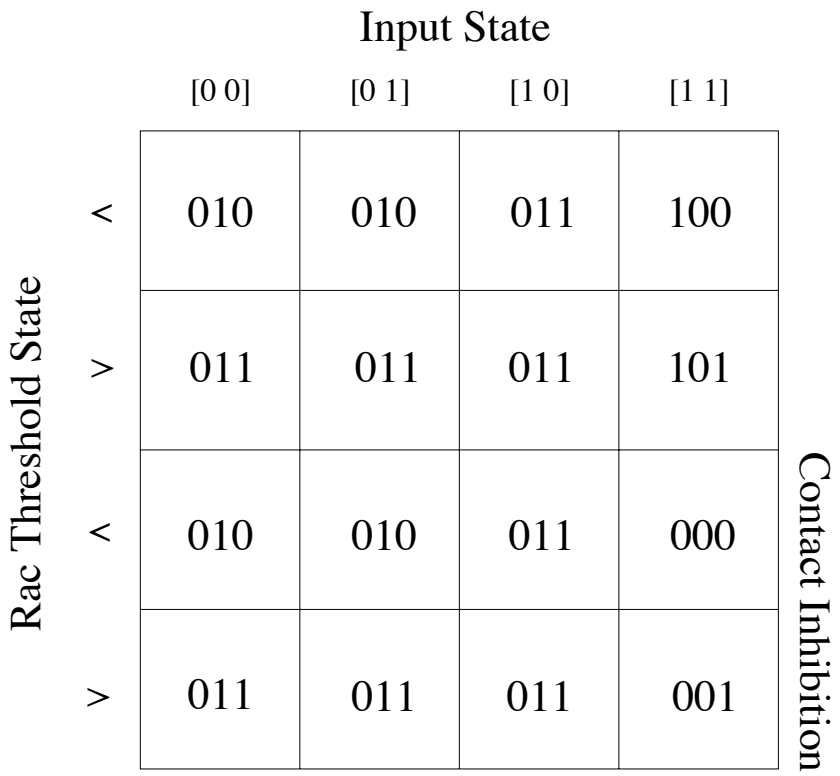

Figure 7.2: Table showing cell phenotype predicted by the baseline Boolean network for various input configurations. This Boolean network model exhibits five distinct cell phenotypes: apoptotic, proliferating, migrating, quiescent, and both proliferating and migrating.

by the cell losing contact with the ECM. Column 3 shows the phenotypes that result when a cell only receives a signal from the ECM. In the absence of any growth factor, as expected, we see apoptosis. The fourth column shows the predicted phenotype when both the VEGF and integrin receptors are activated. When Rac1 is below threshold and therefore not activated, cell proliferation is triggered; when Rac1 is above threshold, the model predicts that the cell will both begin to grow and engage its motility machinery. Contact inhibition has the effect of blocking cell proliferation. Thus, when there is contact inhibition and Rac1 is below threshold, there is no signal at all and the cell becomes quiescent. Whereas when Rac1 is activated and there is contact inhibition, the result is cell migration. Figure 7.3 shows a simulation screenshot for each outcome.

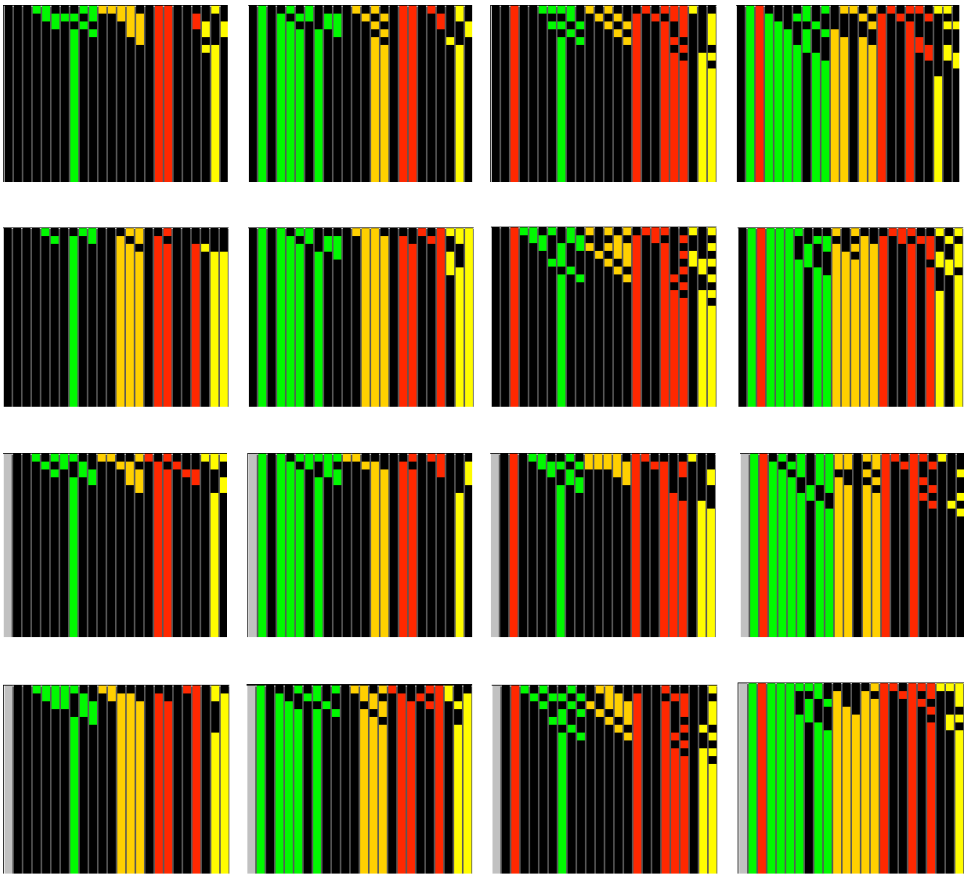

Figure 7.3: Screenshots of baseline network dynamics. Time runs from top to bottom. Input signals are shown in the first three rows and the resulting phenotypes are shown in the last three rows. Internal signals correspond in both number and color to Figure 7.1. Each figure above corresponds with the rows and columns of Figure 7.2. The first three columns show the results from our control cases: no external signal, VEGF signal only, and integrin signal only respectively. As expected, apoptosis results in each case. The fourth column shows the predicted phenotypes given that both the VEGF and the integrin receptors are activated. From top to bottom: proliferation, proliferation and migration, quiescence, and motility.

7.4.2 Investigating the relationship between Rac1 and Rho

Cdc42, Rac1, and Rho are key mediators of cell migration. Experiments agree that Cdc42 activates Rac1. How Rac1 and Rho interact and regulate migration, however, is not yet well understood. Different experimental groups report different relationships and feedback schemes between these three signaling molecules. Since the relationship between Cdc42 and Rac1 is known, without any loss of information we couple Cdc42 and Rac1 into a single node and refer to it as Rac. Reported interactions include: Rac inhibits Rho [142, 104], Rac activates Rho [118], Rac and Rho negatively feedback on each other [163], and Rac activates Rho, but Rho provides negative feedback to Rac [139]. Using this network model, we study the effect of different feedback schemes between Rac and Rho.

Figure 7.4 shows the predicted phenotypes for different Rac/Rho feedback schemes. Panels (a)−(d) are the results when (a) Rac and Rho negatively feedback on each other, (b) Rac provides positive feedback to Rho and Rho inhibits Rac, (c) Rac activates Rho, and (d) Rac inhibits Rho. When there is a negative feedback loop between Rac and Rho (Figure 7.4a), the network dynamics are identical to the baseline dynamics except for the case with both VEGF and integrin input signals activated and Rac is below threshold (row 1, column 4). We now see two different attractors: one that signals the proliferative phenotype and one that predicts proliferation (100) and oscillations in motility (10ω). The oscillatory state is designated by ω. We ran 50,000 simulations and found that 85% of the time the system converges to the fixed point attractor (100) and 15% of the time it converges to the periodic attractor (10ω). Thus, the effect of introducing negative feedback into the system between Rac and Rho is that a weak migratory signal emerges under very specific conditions: VEGF and integrin receptors activated, Rac inactive, and no contact

inhibition signal. When Rac provides positive feedback to Rho (Rho still inhibits Rac), we see different phenotypes predicted only for the dual input signal cases when Rac is activated (see Figure 7.4b). Here we see that the periodic attractor in row 1 column 4 is stable, meaning an oscillating signal for motility emerges with probability 1 compared to the 15% occurrence we observe with negative feedback. The presence of oscillations in the migratory signal may indicate a weak migratory signal or a reduction in the frequency of the migratory cell phenotype. When Rac strictly activates Rho (Rho does not influence Rac), the phenotypes predicted match those predicted by the baseline network, except that we see a strong signal for motility in all dual input cases (Figure 7.4c column 4). Notice that the oscillations no longer occur compared to the network results with positive feedback. Similar results are seen when Rac inhibits Rho (Figure 7.4d column 4). These networks are unable to generate quiescent cells or cells that are proliferating only.

7.4.3 Dynamical stability analysis

Network exhibits high robustness of signal transduction

One measure of network robustness is whether signal transduction depends on the choice of initial conditions. To test this, the initial condition for each internal node (2-19) is set to $s = 1$ with probability $p = 0.5$, otherwise it is set to $s = 0$. Thus the number of 1's in the initial conditions follows a binomial distribution. Of the 2^{17} (131,072) possible initial condition configurations, 50,000 were tested at random for each input state. We perform this analysis for each network, that is, the baseline network and the networks corresponding to the different feedback schemes between Rac and Rho. In all cases, dynamics converge to the final attractor states (i.e., the corresponding output configurations) with probability $p = 1$ with one exception. For the case in which both the VEGF and integrin receptors are activated, Rac is below

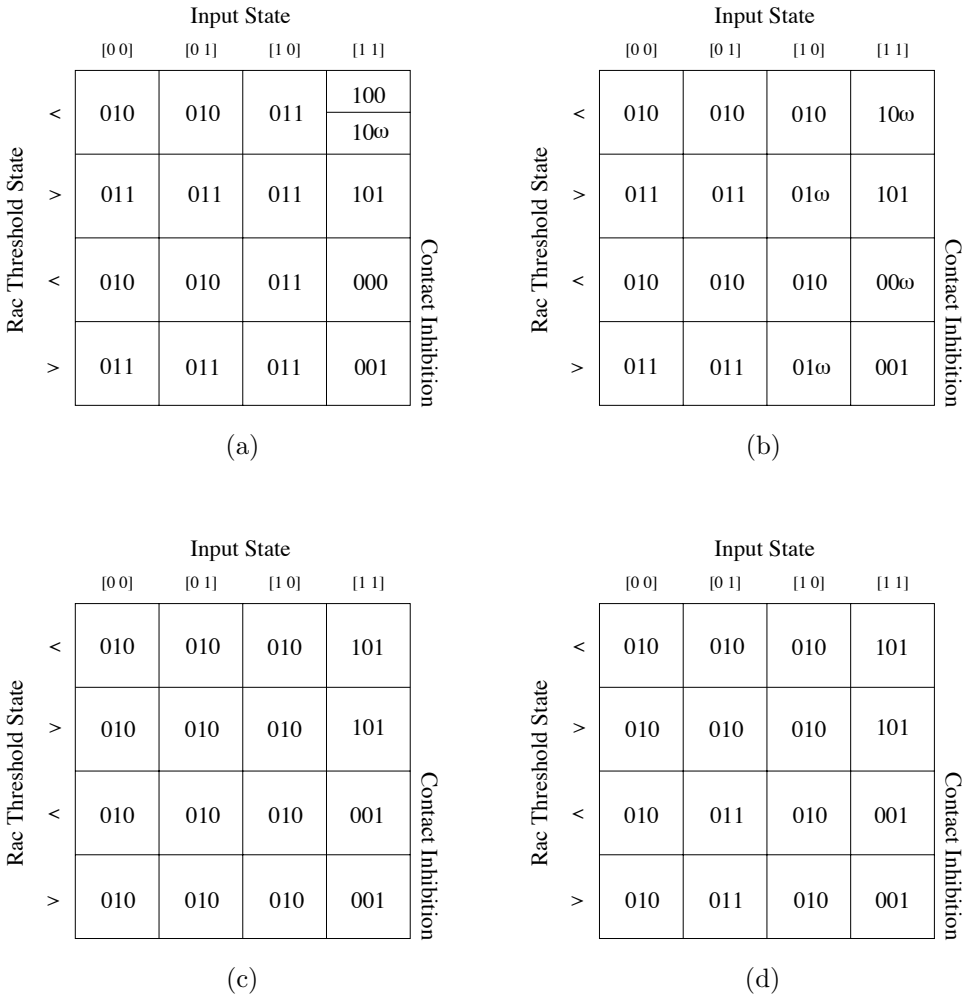

Figure 7.4: IO table showing cell phenotype predicted for various Rac/Rho feedback configurations. (a) negative feedback, (b) positive feedback, (c) Rac activates Rho, (d) Rac inhibits Rho.

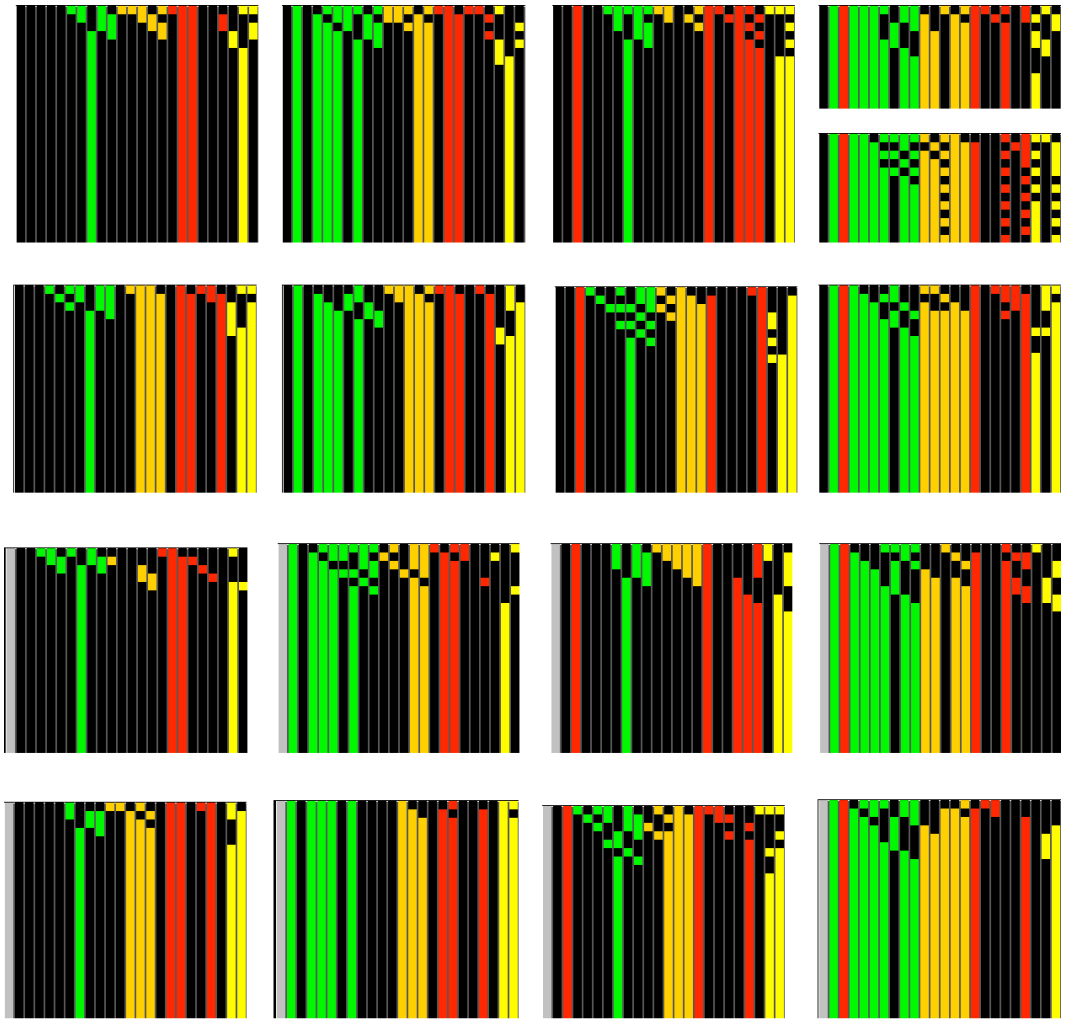

Figure 7.5: Screenshots of network dynamics when Rac provides negative feedback to Rho. Dynamics are identical to the baseline dynamics except for the case when both VEGF and integrin receptors are activated and Rac is inactive (row 1, column 4). We now see two different attractors: one that signals the proliferative phenotype (top), and another that predicts proliferation and oscillations in motility (bottom).

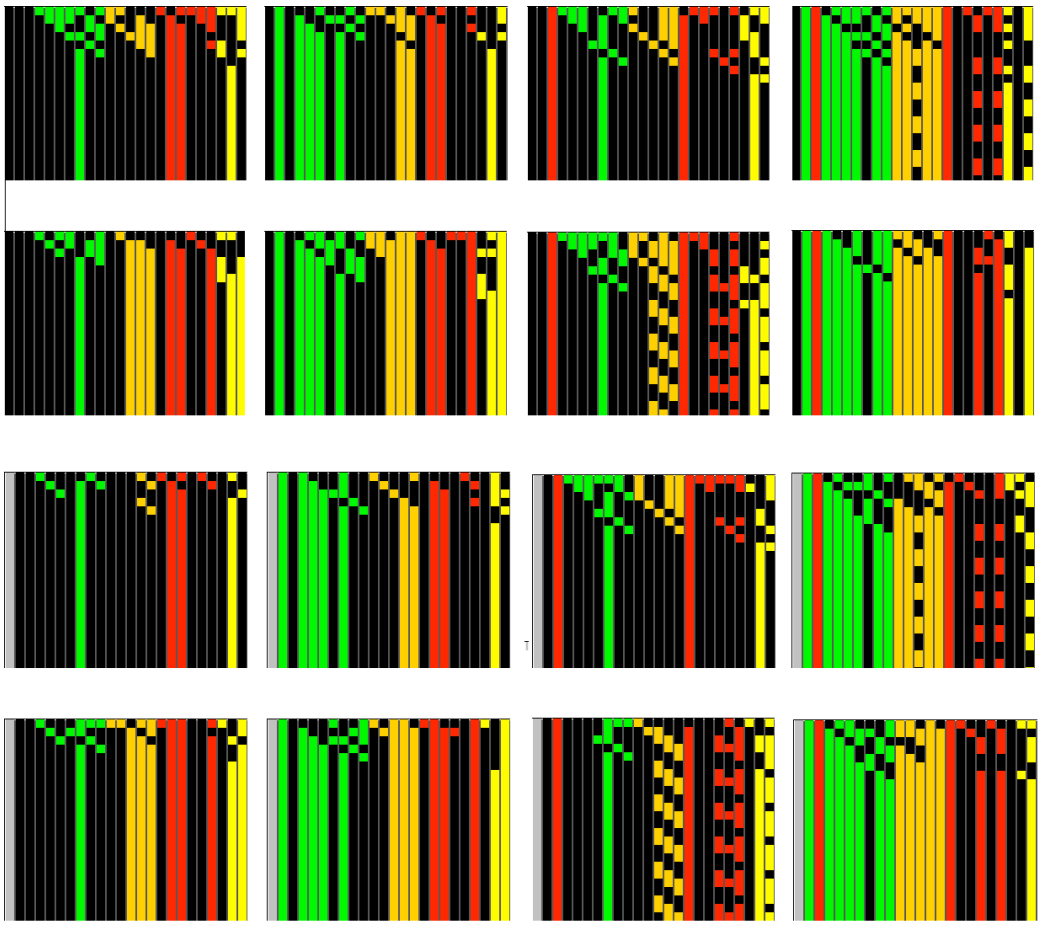

Figure 7.6: Screenshots of network dynamics when Rac provides positive feedback to Rho. Compared to the baseline network, different phenotypes are predicted only for the dual input signal cases when Rac is activated. The periodic attractor in row 1 column 4 is stable, meaning an oscillating signal for motility emerges with probability 1 compared to the 15% occurrence we observe with negative feedback.

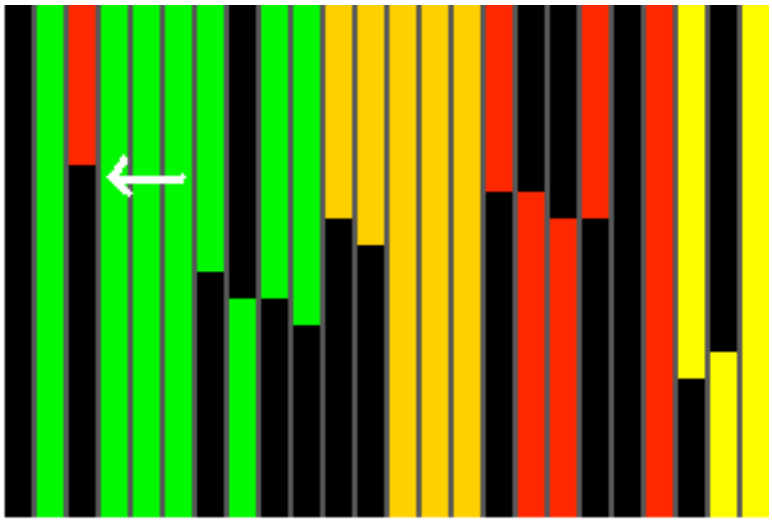

Figure 7.7: Network exhibits a fast and stable response to changes in external stimuli. Screenshot of the baseline network with Rac above threshold during a transient switch from simultaneous VEGF and integrin signals to a VEGF signal only (white arrow). After only 8 updates, the system has converged to a new attractor and the cell undergoes apoptosis.

threshold, and Rac and Rho negatively feedback on each other (row 1 column 4 of Figure 7.4a), 85% of the initial configurations converge to the fixed point attractor (100), while 15% converge to the periodic attractor (10ω). These findings imply that the output states are a function of input signals only, that is, the network response does not depend on the initial internal state of the nodes.

This network also exhibits a fast and flexible response to changes in external cues. Figure 7.7 is a screenshot showing the results of a runtime change in the external signal received during a simulation. These simulations use the baseline network with Rac above the activation threshold and input signals from both the VEGF and integrin receptors. After the system converges, in this case to growth and migration (101), we obstruct the integrin receptor signal (see arrow in Figure 7.7). The network converges to a new attractor commensurate with the input signal of (10) and signals a change in phenotype from growth and migration to apoptosis. We find that if, after convergence for a given input configuration, one input is changed,

the dynamics converge after only a few updates to the attractor(s) that correspond to the new input signal. Therefore, we conclude that the network demonstrates a high sensitivity to transient temporal switching of, or perturbations to, external signals. The insensitivity of the network dynamics to the initial conditions of the internal states coupled with the ability to quickly and accurately respond to perturbations in the input signals demonstrates that the network exhibits extremely high signal transduction robustness.

Network response is stable under asynchronous updates

Whether and how the results depend on the updating scheme employed is another measure of the dynamical robustness of a network. We test this by implementing asynchronous, stochastic updates instead of in parallel (synchronous) updating. For asynchronous updates, the state, s, of each network node is updated independently according to the following rule:

$$s_i(t) = \begin{cases} f_i(\vec{\xi}_i(t-1)) & \text{with probability } p, \\ s_i(t-1) & \text{with probability } 1-p, \end{cases}$$

where f_i denotes the Boolean function for node i given input vector $\vec{\xi}_i$. This says that with probability p, the state at time t is switched according to the Boolean function of the inputs at time $t-1$, and with probability $1-p$, its state remains unchanged.

Figure 7.8 shows an example of the dynamics using an asynchronous, stochastic updating scheme with $p = 0.4$. Both the VEGF and the integrin receptors are activated, Rac is above the threshold needed for activation, and there is a negative feedback loop between Rac and Rho. After approximately 30 updates, the system converges to its stationary state. Using asynchronous updating, we find deterministic

Figure 7.8: Screenshot from a simulation using an asynchronous, stochastic updating scheme with $p = 0.4$. We find that network dynamics are governed by the topography of the network, not the updating scheme used.

($p = 1$) convergence to the same attractors as for parallel (synchronous) updates. Figure 7.9 shows that the convergence times scale linearly with the average update frequency $1/p$. That is to say that the interaction probabilities, $p < 1$, determine only the time-scale for convergence, but do not affect the final output states. Thus, the final states (attractors) depend on network topology only, not on the details of the order of updates. These results suggest that signal transduction is very reliable even when only small concentrations of signaling molecules are present, and interactions of signal molecules are relatively rare, stochastic events.

Sensitivity to Noise

Another robustness test for network dynamics is to make the Boolean functions themselves stochastic, but otherwise update nodes synchronously (in parallel). Thus,

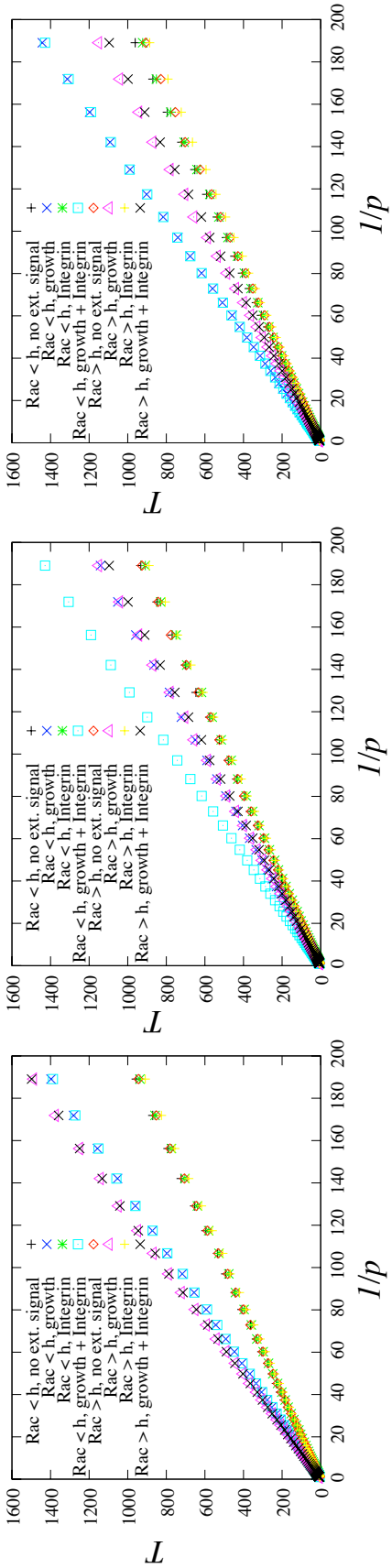

Figure 7.9: Convergence times T to attractors as a function of the update frequency $1/p$ for different external signal combinations and asynchronous updates. Left: baseline network; middle: negative feedback between Rac and Rho; right: positive feedback between Rac and Rho.

each node changes its state according to:

$$s_i = \begin{cases} f_i(\vec{\xi_i}) & \text{with probability } 1-p, \\ 1 - f_i(\vec{\xi_i}) & \text{with probability } p, \end{cases}$$

This says that the node takes the "wrong" state (i.e., error in signal transduction) with probability p. This can be interpreted as internal noise, for example, due to the spontaneous production or decay of a signaling molecule. Typically, for a biological cell, p will be very small, since all reactions rely on catalysis, with spontaneous reaction rates being orders of magnitude smaller than those of catalyzed reactions. Note that $p = 0$ corresponds to deterministic updates and $p = 1/2$ to completely randomized updates.

Figure 7.10 shows the probabilities or rates, r, that a 1 appears in the output table for each of the phenotypes. Plots (a)−(d) correspond to the 4 inputs states: $\{(00), (10), (01), (11)\}$. For all input configurations, we find that growth and motility cell phenotypes are less sensitive to an increase in p, compared with apoptosis, where r crosses the line $r = 0.5$ for values between $p = 0.05$ and $p = 0.1$. Interestingly, this indicates that the apoptotic response is highly sensitive to noise, suggesting that the probability of programmed cell death increases in response to conflicting or confusing signals. In a biological setting, we can interpret this result to mean it is highly unlikely that a cell will undergo apoptosis erroneously. These sensitivity results also signify that the apoptotic signal is a hypersensitive switch, which is consistent with the findings of Wee and Aguda [169]. On the other hand, Figure 7.10 shows the insensitivity of growth and motility to noise and thus the switching functions for growth and motility may be best described by a smooth function (e.g., tanh(x)).

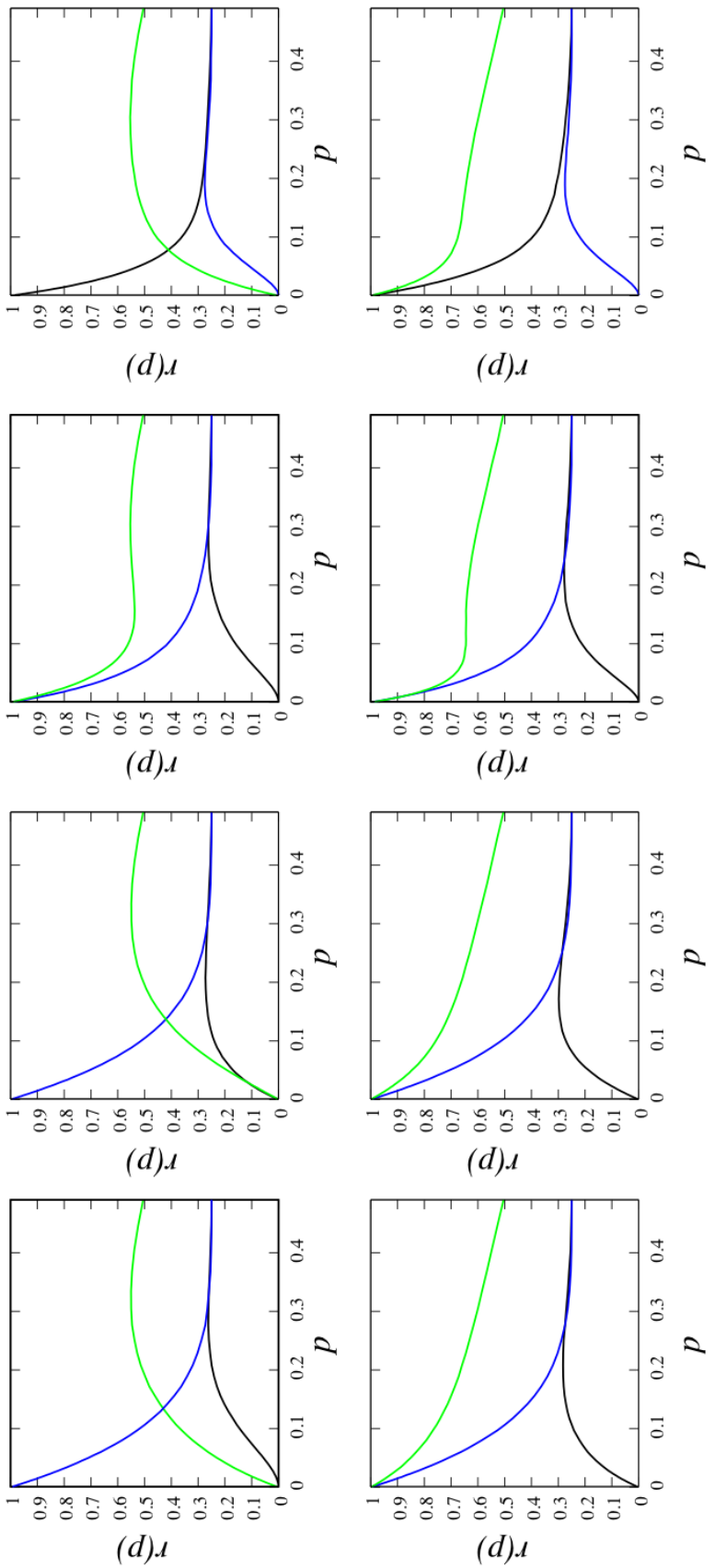

Figure 7.10: Plots showing the network response to noise (p). The top row corresponds to the 4 inputs states: $\{(00), (10), (01), (11)\}$ when Rac is below threshold. The bottom row shows our results for Rac above threshold. Apoptosis is shown in blue, motility in green, and growth in black.

7.5 Discussion

Due to the scarcity of quantitative data on the kinetics of the intracellular biochemical reactions involved in key signal transduction pathways during angiogenesis, we develop a simplified Boolean signaling network to describe the signaling pathways critical to cellular regulation and function during angiogenesis. This model is the first to couple VEGF, integrin, and cadherin signaling cascades and cross-talk and is consistent with experimental observations. Using this model, we construct a state table showing the one to one correspondence between receptor activation (inputs) and cellular function (outputs) for this network and study the effect of different feedback configurations between Rho and Rac. We analyze the dynamical stability of the network and find that the system is highly robust. The insensitivity of the network dynamics to the initial conditions of the internal states coupled with the ability of the network to quickly and accurately respond to perturbations in the input signals demonstrates that the network exhibits extremely high signal transduction robustness. We find that the final output state, or phenotype, is completely determined by the input state and not affected by transient or accidental internal variations. In addition, we determine that network response is stable under stochastic desynchronization of updates and moderate internal noise (that is, errors in signaling cascades), indicating that the network architecture is selected for high reliability of response in a fluctuating environment.

CHAPTER VIII

Multi-Scale Model of Angiogenesis

8.1 Incorporating Intracellular Signaling

Introducing intracellular regulation into the cellular model provides another level of biological realism to the system and creates a framework within which we can investigate how the external environment guides critical cellular decisions, including whether the cell is going to proliferate, migrate, or initiate apoptosis, and how these decisions influence sprout morphology. Intracellular signaling is an important consideration for more in depth investigations of the biochemical mechanisms controlling angiogenesis. In Chapter VII, we develop and analyze a simplified Boolean signal transduction network of the cross-talk between the VEGF, integrin, and cadherin receptors. In this chapter, we interface the partial differential equation model for VEGF dynamics, the lattice-based stochastic model describing cellular behaviors, and this Boolean model of intracellular signaling pathways critical to angiogenesis. With this integrated multi-scale model, we are able to capture processes occurring across multiple time scales. Signal transduction occurs on the order of $10^{-2} - 10^{2}$ seconds, whereas cell growth and division take place over tens of hours. Table 8.1 lists the different angiogenic processes that we model and their corresponding time scales.

Table 8.1: This table shows the different time scales (in seconds, s) of biological processes that occur during angiogenesis and the type of model we use to describe each process.

Process	Time Scale	Model Type
Signal transduction	$10^{-2} - 10^{2}$ s	Boolean
VEGF diffusion	$10^{1} - 10^{2}$ s	continuous
Motility	$10^{2} - 10^{4}$ s	discrete, stochastic
Proliferation	$10^{4} - 10^{5}$ s	discrete, stochastic

In the model we present in Chapter VI, cell phenotype is prescribed phenomenologically based on empirical data. In that model, we define a tip cell as the cell leading the sprout, a proliferating cell as the cell(s) immediately behind the tip cell, and all other cells as stalk cells. Each cell phenotype embodies a phenotype-dependent behavior that is consistent with what is observed experimentally. Tip cells are highly specialized motile cells that respond to chemoattractant gradients and secrete ECM degrading proteases; proliferating cells grow to twice their initial size according to an 18 hour cell cycle clock and then divide into two daughter cells; and stalk cells exhibit chemotactic migration, but not as sensitively as a tip cell. In the multi-scale model of angiogenesis, we remove these phenomenological rules prescribing cellular phenotype by incorporating the results from the intracellular signaling network analysis. Now cell function is determined based on the cell's immediate external environment. Moreover, with the introduction of intracellular signaling, the multi-scale model additionally captures apoptosis, cell quiescence, multiple proliferating regions, and multiple branch points. Consequently, the multi-scale model provides a more biologically realistic representation of cellular dynamics and events during angiogenesis. Cell quiescence and apoptosis have received very little attention in previous models of angiogenesis. Very recently, a continuum model of tumor growth and vascular development was developed to explore the effect of blocking the VEGF−Bcl-2−CXCL8 signaling pathway [72]. Although apoptosis has been con-

sidered in models of vessel occlusion, the model by Jain et al. [72] is the first to incorporate endothelial cell apoptosis at the cellular level during tumor angiogenesis. The fact that our multi-scale model captures cellular quiescence and apoptosis opens up a whole new area of investigation relevant to pro- and anti-angiogenic treatment strategies.

Figure 8.1 is a flowchart representation of the multi-scale model architecture showing the feedback mechanisms between the extracellular, intracellular, and intercellular environments and the coupling of multiple time scales. We now remove the phenomenologically based rules that determine whether a cell is a tip, proliferating, or migrating cell. Instead, at every time step, each cell surveys its local landscape and gathers information on the VEGF concentration, the availability of matrix molecules, and the extent of its contact with neighbor cells. These environmental signals are interpreted by the cell, via the signal transduction network, to determine cell phenotype. Because intracellular signal transduction happens on a faster time scale than the other model dynamics, we assume cell signaling happens on the order of one minute and incorporate the results of the signaling network analysis into this model using a look-up table function. Given environmental cues that trigger the VEGF, integrin, and cadherin cell surface receptors, cell phenotype is determined using the table in Figure 7.2. To incorporate the signal transduction network presented in Chapter VII, we must make some assumptions about how to measure receptor signal strength. We have empirical data for the number of endothelial cell VEGF receptors and have already derived how much VEGF an endothelial cell can bind during one Monte Carlo step [Chapter IV]. However, during angiogenesis, the number of integrin and cadherin receptors is dynamically regulated and widely varies, depending sensitively on the cell's environment and on time. In the absence of more

detailed empirical data for receptor number, timing, and mechanism, we estimate the strength of the signal from integrin and cadherin receptors by measuring the matrix molecules immediately available to the cell and cell-cell contact respectively and normalize these amounts by the cell's size. These input signals are values that range from 0 to 1. In addition, the node representing Rac1 in our signal transduction network 7.1 can receive both an activating signal and an inhibitory signal. There is no evidence indicating whether the molecular interactions of Rac1 are inhibition or activation dominant. We model this uncertainty by randomly assigning the strength of the inhibitory signal to Rac1 from Rho and assume that Rac1 is regulated by the net signal. For instance, a net activating signal (> 0) will result in Rac1 activation.

After the phenotype of each cell is determined, cells respond in a phenotype-dependent fashion. The phenotypes that we model include apoptotic (A), quiescent (Q), migrating (M), proliferating (P), and cells that are able to proliferate and migrate (MP). We model apoptosis by setting the cell's target volume to zero and removing any chemotactic incentives ($\chi = 0$). Consequently, apoptotic cells will decrease in size and disappear. When a cell becomes quiescent, it ceases growing or moving in response to chemotactic signals, and will maintain its current volume. Migrating and proliferating cells are treated as previously described in Chapter VI. After a proliferating cell has doubled its size and completed a full cell cycle, it will divide. Migrating cells move in response to VEGF but do not grow or divide. Experiments of *in vitro* angiogenesis by Bautch et al. show cell proliferation can occur in the leading sprout cells [79]. In Chapter V, we study cell motility and find that in our model, cells that can both migrate and proliferate, exhibit the fastest migration speeds. These cells are the most flexible cells in terms of cellular mobility. We use our result to calibrate the chemotactic sensitivity of the MP phenotype so that

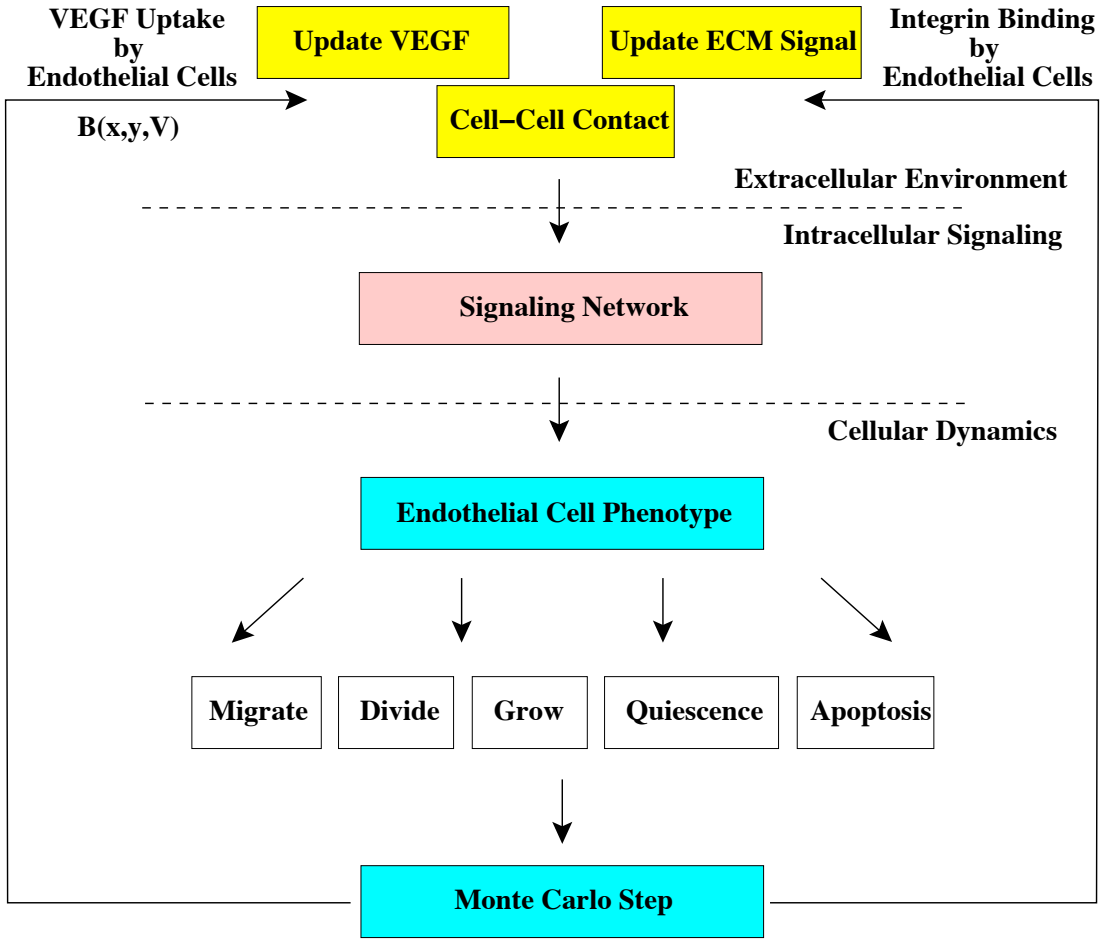

Figure 8.1: Flowchart showing how signals from a cell's extracellular environment generate intracellular signal transduction and determine cell phenotype. Depending on its phenotype, endothelial cells exhibit different behaviors, which lead to changes in the extracellular space. The extracellular, intracellular, and intercellular environments feedback on each other coupling multiple timescales.

it is consistent with the chemotactic sensitivity of the tip cell phenotype of Chapter VI. We examine the effect of assuming a higher chemotactic sensitivity for the MP phenotype in our discussion of model validation (Section 8.2.1).

The stroma then evolves in time through one Monte Carlo step and the new spatial profiles for the cells, VEGF, and ECM are used as inputs for the next iteration. As this process repeats, cells respond to a dynamic environment and vascular sprouts develop as the biological system evolves toward energy minimization.

8.1.1 Parameter calibration

A list of values for the model parameters is provided in Table 8.2, including references. Parameters are taken from experimental data or other published sources whenever possible. If no reference is given, the parameter is a relative value chosen to emulate the physical properties and behaviors of cells. The thresholds for signal activation are a ratio of signal strength to current volume of the cell. The VEGF receptor signal threshold, T_R, is chosen in order to activate the initial endothelial cell and is the amount of VEGF in picograms normalized by the size of the initial endothelial cell. The integrin receptor threshold, T_I, and the threshold for the strength of the VE cadherin signal necessary to trigger contact inhibition, T_{CI}, are chosen to reproduce reasonable sprout morphologies. By equating the time it takes an endothelial cell to divide during the simulation with the endothelial cell cycle duration of 18 hours [170], we convert Monte Carlo steps to real time units. In the simulations reported in this chapter, 1 Monte Carlo step is equivalent to 1 minute.

8.2 Results

8.2.1 Cell phenotype distribution in time predicted by multi-scale cell-based model

The multi-scale model reproduces biologically realistic sprout morphologies and sprout extension speeds. We validate this model by showing that average simulated sprout extension speeds and sprout morphologies are consistent with those measured experimentally [52, 79] (Figures 8.2 and 8.3). We measure average extension speed as the total sprout displacement in time and report it in microns per hour (μm/hr). See Section 6.2.1 for a detailed description of these experiments and our validation method.

Figure 8.3 shows a simulated sprout developing at (a) 3.1, (b) 9.5, and (c) 14

Table 8.2: Table of Parameters. Dimensions are given in terms of L=length, T=time, M=mass and E=energy. Unless otherwise noted, all simulations used the same parameter set and initial conditions. EC denotes endothelial cell and VI indicates parameter values that were estimated in Chapter VI.

Parameter	Symbol	Dimensions	Model Value	
Length Scales	L_1, L_2	L	166μm, 106μm	
VEGF Diffusion	D	L^2/T	3.6x10^{-4} cm^2/h	[148]
VEGF Decay	λ	T^{-1}	0.6498 h^{-1}	[148]
VEGF Uptake	β	M/cell/T	0.06 pg/EC/hr	[20, 46, 168]
VEGF Source	S	M/L	0.035 pg/pixel	[93, 75]
RTK Signal Threshold	T_R	M/L	0.00095 pg/pixel	
ITG Signal Threshold	T_I	non-dim	0.20	
VE Cadherin Threshold	T_{CI}	non-dim	0.20	
Adhesion				
EC−EC	J_{ee}	E/L	30	[VI]
EC−Fluid	J_{ef}	E/L	76	[VI]
EC−Matrix	J_{em}	E/L	66	[VI]
Fluid−Fluid	J_{ff}	E/L	71	[VI]
Fluid−Matrix	J_{fm}	E/L	85	[VI]
Matrix−Matrix	J_{mm}	E/L	85	[VI]
Membrane Elasticty				
EC	γ_{e}	E/L^4	0.8	[VI]
Matrix	γ_{m}	E/L^4	0.5	[VI]
Fluid	γ_{f}	E/L^4	0.5	[VI]
Chemotactic Sensitivity	χ	E/conc	$1.11 \cdot 10^6$	
MP Cell	χ_{MP}	E/conc	$-1.45\,\chi$	[VI]
Migrating Cell	χ_{M}	E/conc	$-1.42\,\chi$	[VI]
Proliferating Cell	χ_{P}	E/conc	$-1.40\,\chi$	[VI]
Quiescent Cell	χ_{Q}	E/conc	0	
Apoptotic Cell	χ_{A}	E/conc	0	
Intracellular Adhesion	α	E/L	300	[VI]
Boltzmann Temperature	kT	E	2.5	[VI]

hours. In panel (c), the sprout extension speed is 11.19 μm/hr and a new bud, or branch point, develops from the main sprout (arrow). One major advantage of this cell-based model is that we are able to track the different cell phenotypes in time. Thus, we can determine whether the spatial distribution of different cell phenotypes is correlated to sprout morphology or branching patterns. Let {MP, P, M, Q, A} denote the migrating and proliferating, proliferating, migrating, quiescent, and apoptotic cell phenotypes respectively. The distribution of cell phenotypes in time for the simulation shown in Figure 8.3 given from the head of the sprout is (a)={P, MP, P, M}, (b)={MP, MP, MP, MP, Q, M, P, P, MP, Q, M}, and (c)={MP,

MP, MP, MP, MP, P, P, P, Q, P, M, M, Q, P, M}. The highly mobile MP cells cluster at the head of the sprout. Naturally the question arises whether our choice of chemotactic sensitivity for the MP cell type prescribes this clustering. Using the chemotactic sensitivities calibrated in Chapter VI for tip and migrating (therein referred to as stalk) cells, we consider the following cases: $\chi_{\mathrm{MP}} > \chi_{\mathrm{M}}$, $\chi_{\mathrm{MP}} = \chi_{\mathrm{M}} = 1.45$, $\chi_{\mathrm{MP}} = \chi_{\mathrm{M}} = 1.55$, and $\chi_{\mathrm{MP}} < \chi_{\mathrm{M}}$. We find that in all cases the MP phenotype emerges at the sprout tips. Sprout morphology is not affected; all sprouts appear very linear and there is no observable difference in cell shape, except for the case $\chi_{\mathrm{MP}} = \chi_{\mathrm{M}} = 1.45$ in which cells are generally rounder and less elongated in appearance. We attribute rounder cell shapes to the weaker chemotactic coefficient. There are, however, differences in sprout extension speeds between these four cases. The results are shown in Table 8.3. The fastest velocities ($10.87 \pm 0.198\mu$m/h) occur when $\chi_{\mathrm{MP}} = \chi_{\mathrm{M}} = 1.55$ and the slowest ($10.145 \pm 0.18\mu$m/h) occur when $\chi_{\mathrm{MP}} = \chi_{\mathrm{M}} = 1.45$. Thus, χ is one regulator of sprout extension speed, but changes in χ of this magnitude do not otherwise play a material role. This corroborates the finding from our sensitivity analysis results for χ from Chapter VI. However, sprout migration speeds are not significantly different between $\chi_{\mathrm{MP}} > \chi_{\mathrm{M}}$ and $\chi_{\mathrm{MP}} < \chi_{\mathrm{M}}$ indicating that our choice of chemotactic sensitivity does not influence the fact that the MP phenotype appears at the sprout's tip. Thus, we conclude that MP cell clustering at the head of the sprout occurs as a result of each cell's local landscape and that the environmental conditions near the sprout tip are conducive to cell migration and proliferation. In addition, we observe that the MP cell phenotype is frequently followed by a proliferating cell or region. Both of these phenomena are emergent.

In agreement with experimental findings that highly motile, often called "tip" cells, lead the sprout and new branch formation [39], our model is further validated by the

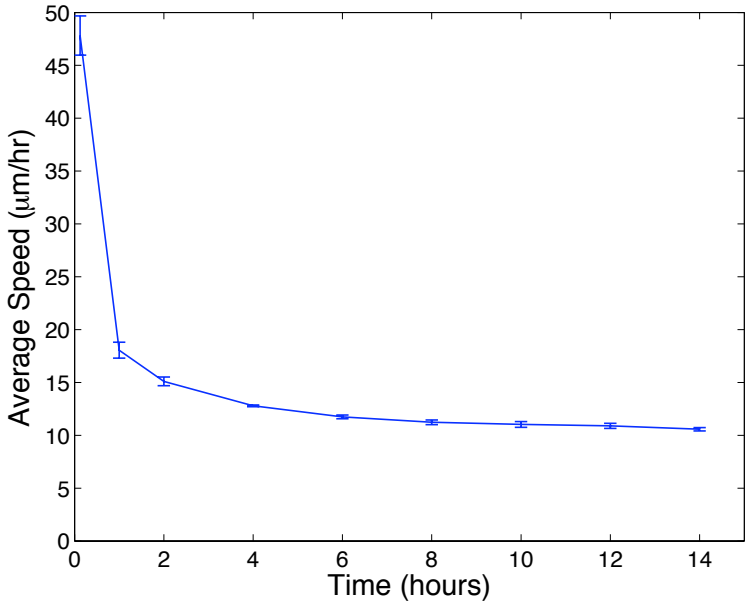

Figure 8.2: Multi-scale model validation: simulated sprout extension speeds agree with those experimentally measured [52, 79].

phenotype distributions we observe during simulations. Specifically, the patterns of highly mobile MP cells clustered at the head of the sprout and are generally followed by a region of proliferating cells (see Figure 8.3). Interestingly, the budding cell at the branch point in Figure 8.3 is a proliferating cell. In one of the few experimental studies to observe where proliferation occurs during new sprout development, Bautch et al. shows that cell division occurs at the base of new sprout branches [79].

8.2.2 Model reveals link between matrix density, cell phenotype, and sprout branching

In Chapters V and VI, we showed that the structure and composition of the stroma have a significant impact on vascular sprout development. We continue this investigation using the multi-scale model and are able to consider now how ECM topography, cell phenotype, and sprout morphology influence each other. As was done in Chapter VI, we simulate angiogenesis for varying extracellular matrix fiber

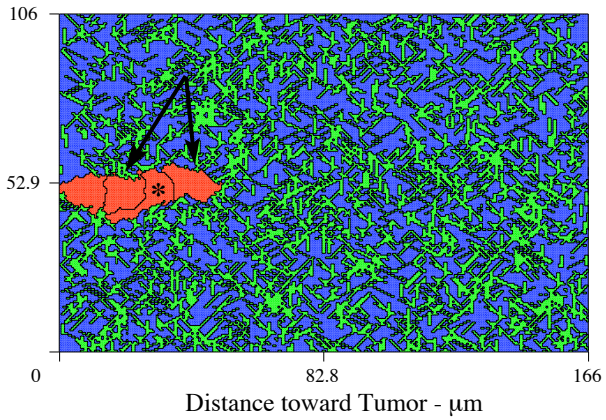

(a)

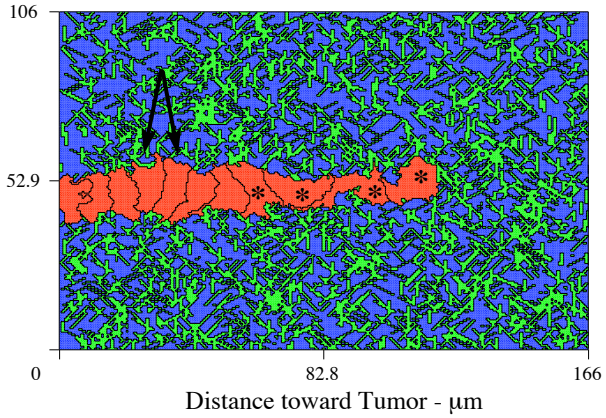

(b)

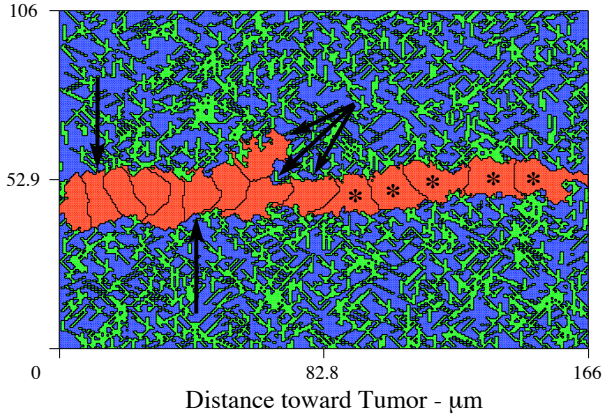

(c)

Figure 8.3: The multi-scale model reproduces biologically realistic sprout morphologies and sprout extension speeds consistent with those measured experimentally. Snapshots at a) 3.1, b) 9.5, and c) 14 hours. At 14 hours, the sprout extension speed is 11.19 μm/hr and a new bud branches from the main sprout. The budding cell is a proliferating cell (arrow). Asterisks mark the MP phenotype.

Table 8.3: Table comparing average sprout extension speeds as a function of phenotype dependent chemotactic sensitivity. Results show that chemotactic sensitivity does not influence the fact that the MP phenotype appears at the sprout's tip. MP cell clustering at the head of the sprout occurs as a result of each cell's local landscape and is an emergent phenomenon.

Chemotactic Sensitivity	mean $\pm$ std error
$\chi_{\mathrm{MP}} = \chi_{\mathrm{M}} = 1.55$	10.87 ± 0.198
$1.55 = \chi_{\mathrm{MP}} > \chi_{\mathrm{M}} = 1.45$	10.54 ± 0.156
$1.45 = \chi_{\mathrm{MP}} < \chi_{\mathrm{M}} = 1.55$	10.40 ± 0.166
$\chi_{\mathrm{MP}} = \chi_{\mathrm{M}} = 1.45$	10.15 ± 0.18

densities. Fiber density is given as the fraction of interstitial tissue occupied by matrix fibers, ρ, and corresponds to physiological quantities of collagen ranging from $0.0 - 0.53$ g/ml. For these simulations, all parameters except matrix density are held fixed. Simulations capture the first 14 hours of new sprout development.

We compare the average rates of sprout extension at different densities. The results are shown in Figure 8.4. Average extension speeds are given in microns per hour (μm/hr) at various times (2, 5, 10, 14 hours) during sprout formation. Sprouts developing on matrix densities $\rho < 0.1$ and $\rho > 0.8$ exhibit developmental defects, such as severe cellular elongation or cell-cell contacts that cannot be maintained. Consequently, no cohesive sprout body forms and we do not report extension speeds for these density ranges. Sprouts extension speeds increase as matrix density increases up to $\rho < 0.3$. This supports our finding in Chapter VI that the guidance cues and fiber network connectivity provided as the density increases are instrumental in sprout development. We confirm our previous finding that sprout velocities peak within an intermediate fiber density range. Multi-scale simulations show that sprouts attain a maximum speed on densities between $\rho = 0.35 - 0.45$. This is slightly different from our results from Section 6.2.2 that predicted peak velocities between $\rho = 0.3 - 0.4$. These two results, however, are generally compatible and strongly suggest there exists an optimal matrix density for promoting angiogenesis.

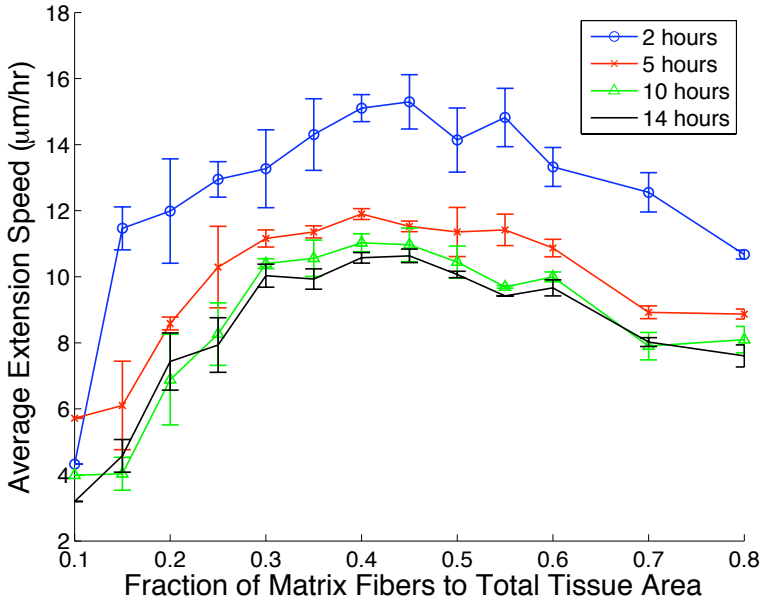

Figure 8.4: Plot showing the dependence of sprout extension speeds on matrix fiber density. Multi-scale simulations show that sprouts attain a maximum speed on densities between $\rho = 0.35 - 0.45$.

Experimental verification is needed. Figure 8.4 indicates that peak migration speeds are prominent at 2 hours, although still evident to a lesser extent at 10 and 14 hours. Thus, these results do not depend on time. Empirical measurements of endothelial cell migration speeds on various fibronectin concentrations (0.5, 1, 5, 20, 40 μg/cm^2) demonstrate peak migration speeds at intermediate concentrations (5 μg/cm^2) [149] and support our findings that maximum migration speeds depend on matrix density. Above $\rho = 0.6$, higher matrix densities start to present a physical barrier to migration and we see a corresponding decline in sprout extension speed.

Next, we turn our attention to the relationship between fiber density and sprout morphology. Confirming our finding in Chapter VI, developmental defects result on matrices of density $\rho \leq 0.1$ or $\rho > 0.8$. Figure 8.5 (a) and (f) are two examples. At $\rho = 0.1$, most cells receive insufficient survival signals from the ECM and undergo apoptosis. Apoptosis is first evident at fiber density $\rho = 0.3$ but does not occur with

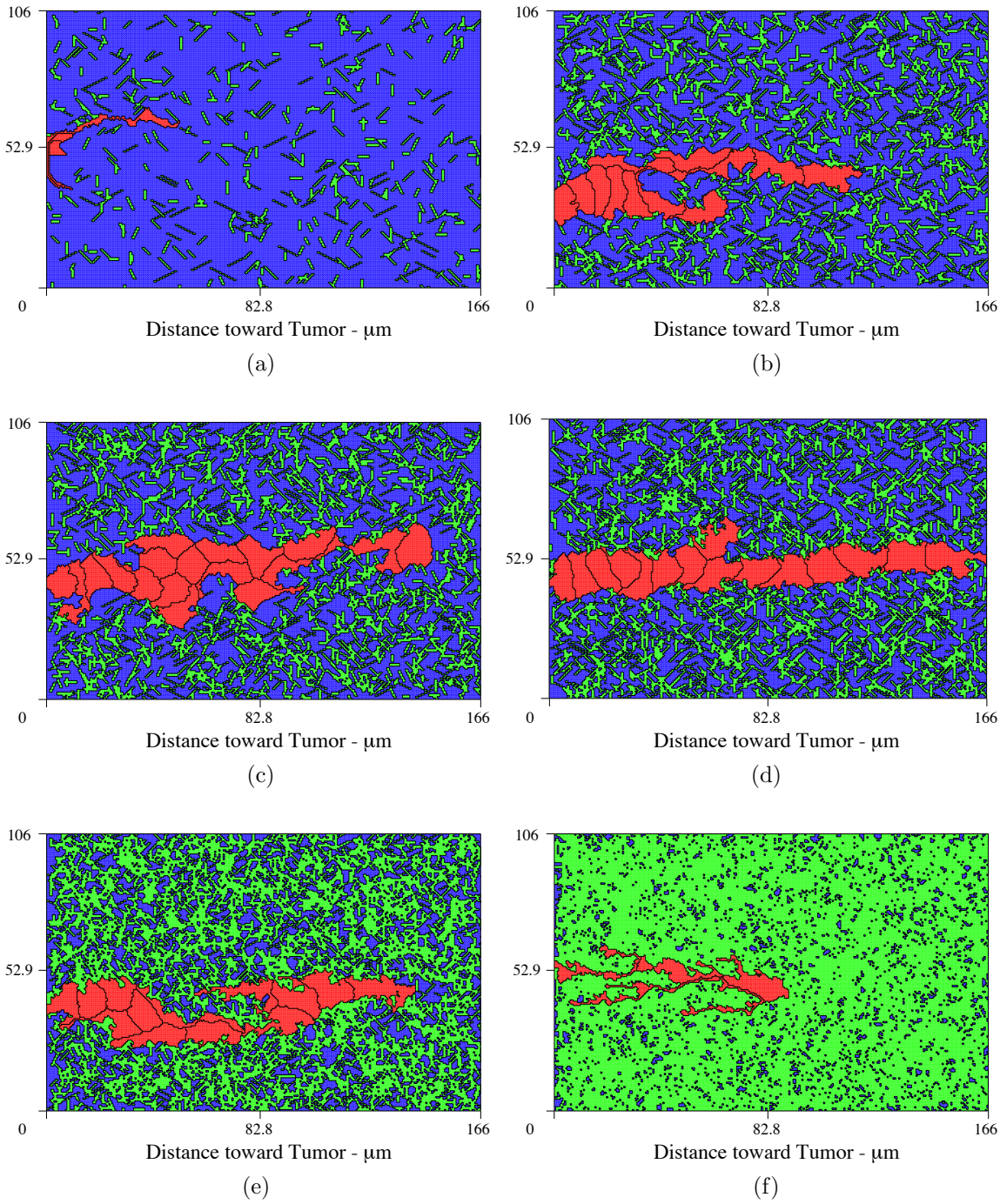

Figure 8.5: Plots showing the relationship between matrix density and sprout morphology. From top left to bottom right: (a) $\rho = 0.10$, insufficient integrin signal from the ECM results in apoptosis and inhibition of angiogenesis; (b) $\rho = 0.3$, high matrix anisotropy contributes to branching; (d) $\rho = 0.4$, cells coordinate chemotaxis and cell-matrix adhesion yielding linear sprouts and maximum velocities; (e) $\rho = 0.6$, cells deform to navigate the denser matrix; and (f) $\rho = 0.9$, complete inhibition of angiogenesis at high matrix density. Snapshots around 14 hours.

any frequency that would disrupt or alter sprout development. As matrix density decreases from $\rho = 0.3$, the number of cells that receive apoptosis signals increases until at $\rho = 0.1$, angiogenesis is completely inhibited. At the other extreme, high fiber density, such as that shown for $\rho = 0.9$ (Figure 8.5f), presents a barrier to cell migration causing cells to severely distort to make any headway. Our findings continue to suggest that manipulating matrix fiber density may be a reasonable target for pro- and anti-angiogenesis therapies.

Remarkably, we again find that sprout branching is highly correlated with a specific fiber density range. We define a new branch as one or more cells that extend, or bud, at least 10 μm from the main sprout body [79]. The multi-scale model predicts matrix densities $0.25 \leq \rho \leq 0.35$ are highly conducive to sprout branching. This is closely correlated to our prediction from Chapter VI where branching was restricted to fiber densities between $0.2 \leq \rho \leq 0.3$. Figure 8.5b shows sprout branching on matrix density $\rho = 0.3$. Figure 8.6 is a time series of snapshots revealing the emergence of new branches during simulated sprout development on a matrix density $\rho = 0.35$ at (a) 4.7, (b) 7.8, (c) 9.4, and (d) 13.3 hours. At 9.4 hours, several new buds have formed branch points and at 13.3 hours new branches are more fully developed. Whereas in Chapter VI we did not observe any branching above $\rho = 0.35$, the multi-scale model predicts branching can occur on matrix densities as high as $\rho = 0.55$. However, the incidence of branching above $\rho = 0.3$ in the multi-scale model is considerably less frequent (35% compared to 80%) and absolutely no branching is seen above $\rho = 0.55$ or below $\rho = 0.3$. In Chapter VI we proposed the possibility that sprout branching is induced by high matrix anisotropy. This mechanical explanation also applies to these results. On matrices with density $\rho = 0.25 - 0.35$, high matrix anisotropy contributes to sprout branching and tortuosity (Figure 8.5b, c).

However, this explanation does not explain why branching occurs at higher densities, albeit rare. The main difference between the model developed in Chapter VI and this multi-scale model is the distribution of cell phenotypes, namely the presence of multiple proliferating regions and multiple branch points. Thus, we may be able to infer that the differences in their respective predictions are due to differences in phenotype distribution. The hypothesis that sprout morphology is correlated to cell phenotype is explored in greater detail in the next paragraph.

In contrast to tortuous and branching sprouts, as matrix density increases to $\rho = 0.4$, sprout formation becomes much more linear (Figure 8.5d). Incidentally, linear sprout formation occurs in the fiber density regime that gives rise to maximum sprout extension speeds. This may suggest that at $\rho = 0.4$, the cellular motility mechanisms, chemotaxis and adhesion to matrix fibers, are well-coordinated by the cells, that is, at $\rho = 0.4$, chemotactic and adhesive forces are present in a combination that promotes motility. In addition, variations in the availability of adhesive binding sites in the ECM that occur as fiber density is altered, combined with VEGF availability, may elicit different molecular signals and therefore different cellular phenotypes. Different phenotype distributions may yield different morphology. At densities $\rho \geq 0.6$, cells begin to alter their shape, elongating to navigate the denser matrix. Compare cell shapes from Figures 8.5d, e, and f. Cell elongation increases with increases in fiber density. At extremely high densities $\rho = 0.9$, sprout extension is stunted.

Recall that sprout branching and tortuosity is evident at $\rho = 0.3 - 0.35$, whereas $\rho = 0.4$ effects very linear sprout morphologies (Figure 8.5b-d). Matrix fiber heterogeneity is one factor contributing to these variations in morphology (linear versus tortuous sprouts), however, morphological differences could also be a consequence of changes in the distribution of cell phenotypes in the sprout. Because our multi-scale

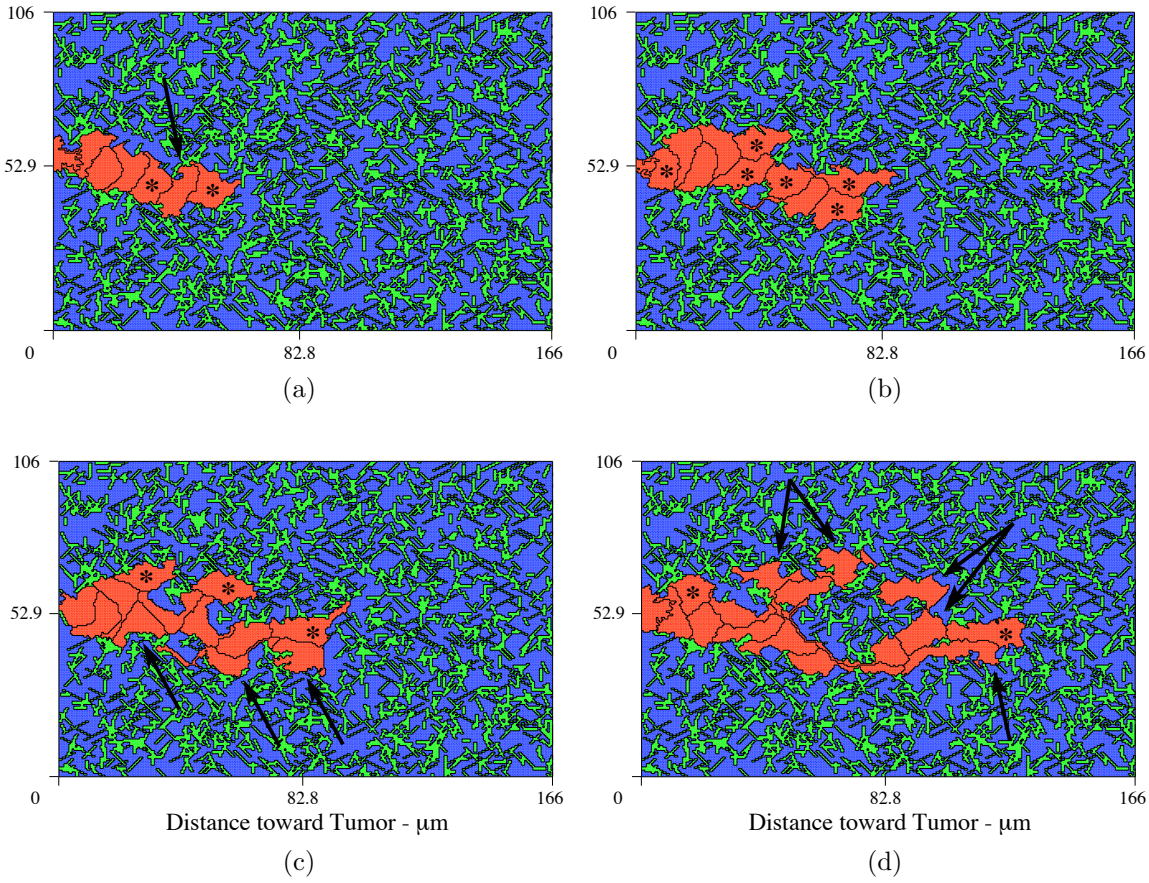

Figure 8.6: Time series of simulated sprout development on a matrix with density $\rho = 0.35$ at a) 4.7, b) 7.8, c) 9.4, and d) 13.3 hours. At 9.4 hours, several new buds have formed branch points and at 13.3 hours new branches are pronounced. Phenotype distribution from right to left is (a)={MP, P, MP, M, Q, M, M}, (b)={MP, MP, Q, MP, MP, MP, M, Q, M, MP, M}, (c)={MP, P, Q, MP, P, Q, M, MP, P, M, Q, M}, and (d)={MP, P, P, P, M, P, M, M, M, P, M, Q, M, MP, Q, M}. Arrows point to proliferating cells; asterisks identify the MP phenotype.

cell-based model captures both changes in cell shape and function sprout development, it allows us to examine how, if at all, vascular morphology is related to cell phenotype. In Figure 8.6a-d, the spatio-temporal phenotype distribution given from right to left is (a)={MP, P, MP, M, Q, M, M}, (b)={MP, MP, Q, MP, MP, MP, M, Q, M, MP, M}, (c)={MP, P, Q, MP, P, Q, M, MP, P, M, Q, M}, and (d)={MP, P, P, P, M, P, M, M, M, P, M, Q, M, MP, Q, M}. Asterisks identify the highly mobile MP cells and arrows point to proliferating cells. In this simulation, after 4 hours (a), the leading cell is an MP cell followed by a single proliferating cell. Another MP cell has developed behind this pair followed by several migrating cells suggesting that early sprout extension is largely powered by motility. That migration facilitates initial sprout extension is supported by experimental observations [151, 124]. Around 8 hours (b), there are six MP cells in the sprout, of which two have developed into new buds. Again, the cells near the parent vessel are predominantly motile phenotypes. Sprout extension is still driven by cellular migration. At 9.4 hours, several of the MP cell phenotypes have received signals stimulating proliferation. Interestingly, the mechanism for sprout extension shifts from a strictly motility driven extension to cooperation between proliferation and migration. Again, this is generally consistent with what is believed to occur *in vivo* where experiments show that cellular proliferation is necessary for continued sprout extension [151, 124]. That being said, exactly when and why sprout formation shifts from motility to proliferation driven remains a conundrum. The buds develop and form several new branch points on the sprout. Tip cell phenotypes lead these branch points, each followed by a proliferating cell. Finally, after 13 hours (d), several new branches emerge. At this stage, both the number of migrating and proliferating cells have increased, however, the sprout consists of proportionately more migrating cells. Viewing each branch as a

new sprout in the early stages of extension, a shift back to motility is consistent with our observations from (a) and (b). There is a distinct region of 3 proliferating cells behind the MP cell, which leads the sprout. Another distinctive proliferating region emerges in the posterior branch.

Figure 8.7 shows five sprouts developing simultaneously. The simulation on the left is identical to the baseline simulations used to validate this model, except that instead of one initial endothelial cell bud, there are five. At 14 hours, the new sprouts are linear and only one has branched showing a 20% (low) branching incidence at $\rho = 0.4$. In addition, no anastomosis occurs. In comparison, the simulations shown in the center and right panels of Figure 8.7 capture sprout development at different stages on matrices of density $\rho = 0.3$, where we typically observe branching. At this matrix density, sprouts are observably more tortuous and the incidence of branching is considerably greater. At 11 hours (center), new branch points are evident on 4 out of 5 sprouts (80%). In another simulation (right), two neighboring sprouts merge forming a loop in a process called anastomosis. Again, multiple branch points emerge. Except for a matrix density of $\rho = 0.3$, all parameters are identical to the baseline parameters and are given in Table 8.2.

8.2.3 "Brush border" effect captured by multi-scale cell-based model

Our simulation domain is designed to model microvessel growth at the diffusion limit for oxygen ($\sim 100\mu$m). Hence, in our simulations, even though proliferating cells are growing and progressing towards mitosis, they reach the boundary of the simulation domain prior to cell division. We now extend the stromal domain to 300 μm. This provides the space and time for sprout cells to complete division. Except for the length of the domain (L_1) and the duration of the simulation, these simulations use a parameter set identical to those given in Table 8.2. Figure 8.8 is a

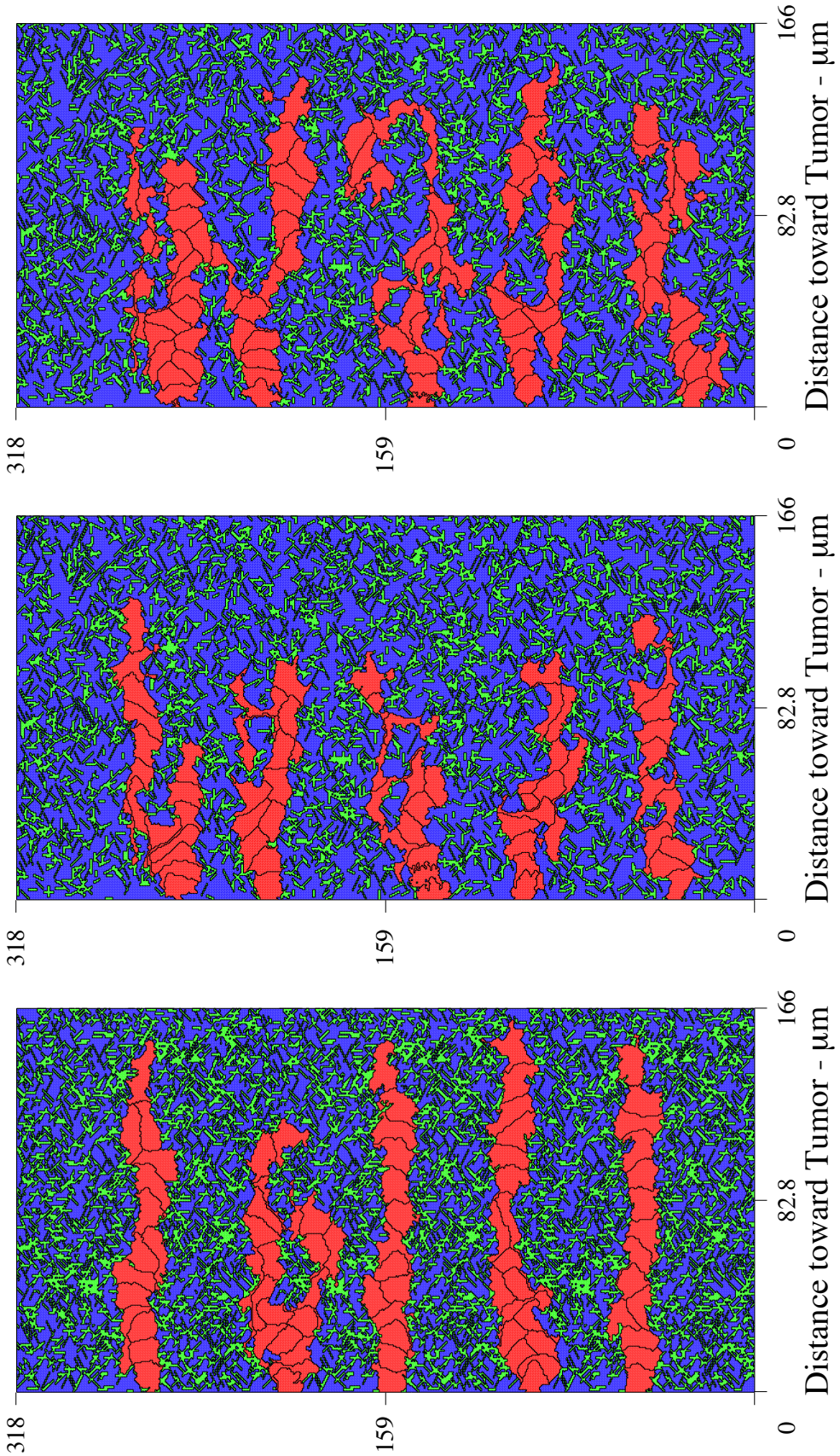

Figure 8.7: Five sprout simulations. (Left) On matrix density $\rho = 0.4$, generally linear sprouts develop; only one has branched, (Center) On $\rho = 0.3$ at 11 hours: Higher branching incidence apparent (80%), (Right) On $\rho = 0.3$ at 13 hours: Neighboring sprouts merge forming a loop, a process called anastomosis. Parameter values are given in Table 8.2.

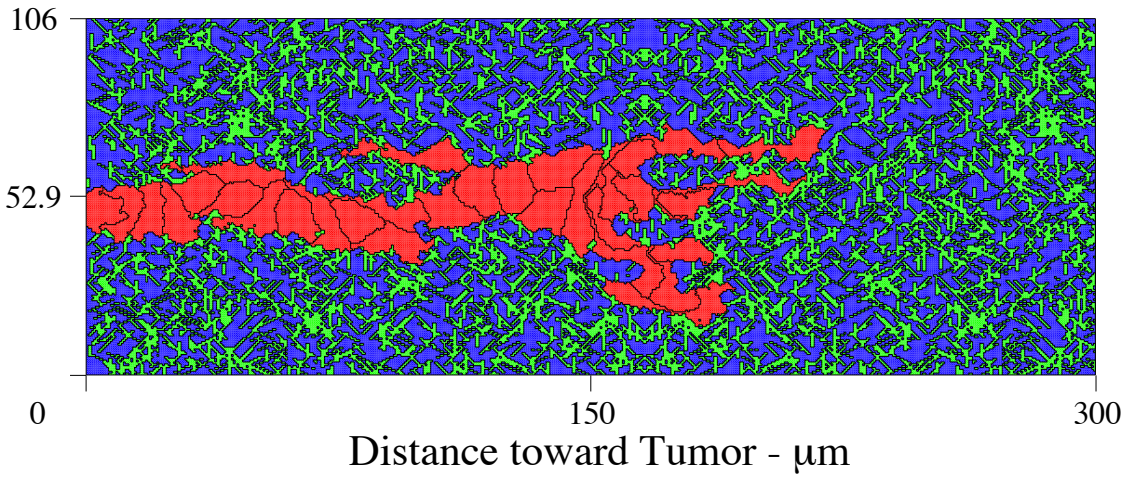

Figure 8.8: Brush border effect (increased branching) evident during sprout simulation on 300 μm domain with $\rho = 0.4$. Snapshot taken at 26.5 hours after some cells have completed mitosis. Parameters and matrix density are identical to the parameters used for multi-scale model validation.

snapshot of sprout growth at 26.5 hours, after several cells have completed mitosis. We observe cell division concentrated near the tip of the sprout and a subsequent increase in sprout branching. The phenomenon of increased incidence of branching as the sprout approaches the tumor is referred to as the "brush border" effect [124, 9]. Of special note is that the matrix fiber density in this simulation is $\rho = 0.4$, a density not typically conducive to branching. The observation that proliferation actually occurs near the sprout tip on a matrix density that induces branching less than 20% of the time (see left panel in Figure 8.7) implies that the observed increase in branching frequency could be correlated to cell proliferation. The "brush border" effect is another emergent behavior of our cell-based model. To date, no other model of tumor-induced angiogenesis has simulated the "brush border" effect except as a consequence of the phenomenologically prescribed rules attendant to branching [9, 158].

8.2.4 Sensitivity analysis

The sensitivity of these results to parameter variability follows the analysis reported in Section 6.2.6. We additionally investigate the sensitivity of these results to the choice of signaling thresholds, T_R, T_I, and T_{CI}. Lowering the value of the VEGF and integrin receptor thresholds can be interpreted as increasing the potency of these receptors, for example, a lower threshold value for T_I means that it requires fewer bound integrin receptors to trigger the integrin signaling pathways. For comparison, we count the number of cells in each phenotype class at 14 hours. When we vary the integrin receptor activation threshold, T_I, we find that the choice of T_I affects both the number of MP cells and the number of cells that undergo apoptosis. The number of MP cells increases with increases in T_I up to a maximum at intermediate values $0.30 \leq T_I \leq 0.35$. For $0.10 \leq T_I < 0.40$, although the distribution of cell phenotypes in the sprout vary, sprout extension speed and sprout morphology do not. At $T_I = 0.3$, we see the first apoptotic cell. As T_I increases, so does the number of apoptotic cells. There is a corresponding decrease in the number of proliferating cells as T_I increases. For $T_I \geq 0.45$, the increase in apoptotic cells and interruption of cell growth halts angiogenesis completely (see Figure 8.9a).

While apoptosis and cell migration are regulated by the choice of T_I, the threshold for contact inhibition, T_{CI}, specifically regulates the number of proliferating cells in the sprout. A small value for T_{CI} indicates that cells are very sensitive to contact with other cells and this contact will inhibit proliferation. For $T_{CI} \leq 0.1$, proliferation is completely inhibited. The sprouts are entirely composed of migrating and quiescent cells. Sprout speeds are suppressed ($\sim 4.7\mu$m/hr) and the sprout is several cells thick. As T_{CI} increases above 0.1, the number of proliferating cells increases. The sprouts are consistently two cells wide, except for $0.1 < T_{CI} \leq 0.2$, the sprout is only 1 cell

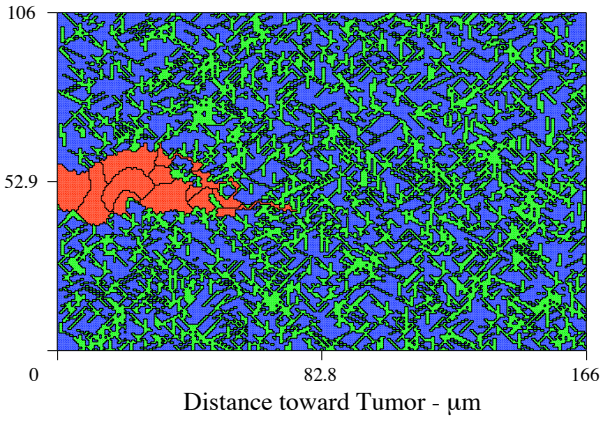

(a)

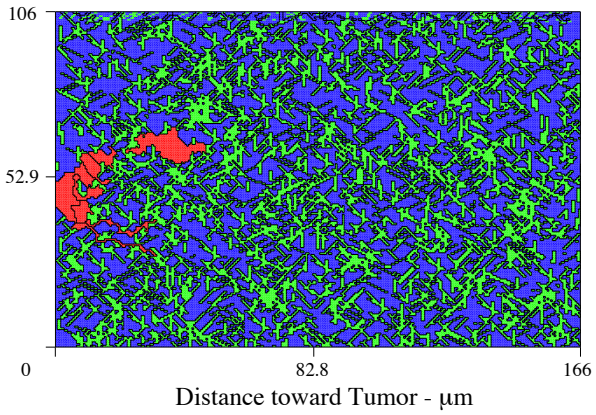

(b)

Figure 8.9: Apoptosis has not received much attention in previous models of angiogenesis. (a) As T_I is increased above 0.45, there is a corresponding increase in apoptotic cells and interruption of cell growth that halts angiogenesis. (b) Apoptosis is also regulated by T_R. In this simulation, at $T_R = 0.005$ cells receive insufficient survival signals and become apoptotic causing sprout regression. Snapshots at 14 hours.

thick. In addition, the number of proliferating cells increases as T_{CI} increases up to $T_{CI} \geq 0.3$. Above 0.3, there is no additional increase in the number of proliferating cells. We do not observe any differences in extension speed with changes in T_{CI} above 0.1.

As we vary the threshold for VEGF receptor activation, T_R, we find that below $T_R = 0.002$, the extension speed and morphology are insensitive to changes in this parameter. For $T_R \geq 0.002$ however, there is an increase in the number of apoptotic cells and vessel growth is halted. Figure 8.9b shows a simulation snapshot at 14 hours using $T_R = 0.005$. As cells receive inadequate survival signals, they enter apoptosis and the developing sprout regresses. There does not appear to be any other recognizable pattern or correlation with cell phenotype. We conclude that in our model T_R is a regulator of cell survival.

8.3 Discussion

We introduce an additional level of cellular regulation and biological realism into our model by integrating the intracellular signal transduction network developed in Chapter VII with the cell-based model of angiogenesis we extended in Chapter VI. The result is a multi-scale cell-based model of tumor-induced angiogenesis. The intracellular signaling network synthesizes what is known about the molecular pathways critical to angiognesis and provides a mechanism for cellular decision making. Consequently, the distribution of cell phenotypes in the sprout are no longer phenomenologically defined; cells regulate their behavior according to the signals they receive from their external environment. Apoptotic and quiescence cell phenotypes are incorporated into our model as a result of the intracellular signaling network. These two cellular functions are rarely considered in other models of angiogenesis

and yet are important dynamics to capture for a model to be useful in testing anti-angiogenesis therapies.

We employ this multi-scale model for a more in-depth exploration of the mechanisms mediating capillary sprout formation. In particular, our studies reveal a correspondence between cell phenotype, sprout morphology, and matrix fiber density. Our model predicts that sprout branching occurs more frequently on matrix densities exhibiting a high degree of anisotropy. In contrast, we find that linear sprouts develop in a density regime coincident with that which elicits maximum sprout velocities. We conjecture that morphological variations are not only due to the mechanical forces arising from ECM anisotropy, but also to the differences in cell phenotype distributions in the sprout that are created as matrix fiber density is altered. A major question experimentalists are fervently pursuing is how the same cellular receptors elicit very different cellular responses. Experiments show that the same VEGF receptor (VEGFR2) is responsible for mediating very different cellular behaviors, including endothelial cell growth, mitogenesis, migration, the production of enzymes and angiogenic factors, and increased cell survival [40, 19, 39]. By varying matrix density and examining cell phenotype and sprout morphology, we show how the availability of adhesive binding sites in the ECM combined with VEGF availability may elicit different molecular signals and therefore different cellular phenotypes. Our findings implicate VEGF-integrin-cadherin receptor crosstalk and variations in a cell's immediate external environment as a potential explanation.

In Chapter V, we point out that proliferation is reported to occur in widely different parts of the sprout, and we use our model to examine the effect of varied proliferating regions on sprout development. Our findings suggest that sprout extension is enhanced as the proliferating region migrates away from the specialized

and exclusively motile tip cells. The multi-scale model naturally allows for different regions of proliferation in the sprout and the possibility that the proliferating region may change and move around. Contact inhibition, which mediates proliferation cues, is also considered in the signal transduction network and is yet another mechanism by which growth differentials may arise within a developing sprout. Because the distribution of cell phenotypes in the sprout is determined by individual cellular response to local external stimuli, multiple branch points and regions of cell proliferation emerge and induce more complex vascular structures. We find that cell proliferation is frequently concentrated toward the sprout tip and new branches, and, therefore, may contribute to multiple branch formation. Simulations of sprout development on longer domains (300 μm) allow cells to complete mitosis. We observe cell division concentrated near the tip of the sprout and increased sprout branching, known as the brush border effect. No model of angiogenesis has simulated the brush border effect without it being a prescribed consequence of the rules for branching. Our findings suggest that cell proliferation plays an important role in the increase in branching frequency as sprouts progress.

The sensitivity analysis reveals some interesting observations about how signal transduction thresholds mediate cell phenotype. A higher receptor activation threshold means that it is more difficult to initiate the signaling cascades associated with that receptor. Biological interventions that act as mechanisms for threshold signal transduction regulation include moderating the up/down regulation of total receptors, the presence of other molecules that competitively bind the receptor, or mediating the binding affinity of the receptor or ligand. We find that the threshold for VEGF receptor activation, T_R, is a regulator of cell survival. At $T_R = 0.002$, blood vessel growth is completely inhibited and the new sprout begins to regress after 20

minutes. This finding suggests that reducing the binding affinity, introducing competitive binding, or blocking the VEGF receptors, will interrupt normal angiogenesis. In fact, targeting the VEGF receptors in these ways forms the basis for many anti-angiogenic therapeutic strategies presently in use or in clinical trials. When we vary the threshold that triggers contact inhibition, T_{CI}, we find that for $T_{CI} \leq 0.1$, there are no proliferating cells in the sprout and sprout extension speed is significantly depressed. As T_{CI} increases and the number of proliferating cells in the stalk increases, sprout extension speeds also increase. This finding provides support that proliferation is necessary for continued sprout extension. Although they did not measure sprout extension speeds, results from Sholley et al. [151] indicate a new sprout can migrate only a finite distance into the stroma and that proliferation is necessary for continued sprout extension. Our finding is generally consistent with this empirical result. An interesting observation is that for $T_{CI} \geq 0.3$, we do not see any additional increase in the number of proliferating cells. This suggests that the effects of further decreases in cell sensitivity to contact inhibition (i.e., T_{CI} increasing) saturate above 0.3.

T_I represents the threshold for integrin receptor signal propagation. Our model predicts that for intermediate values, $0.30 \leq T_I \leq 0.35$, the number of migrating cells is maximal. Consider this prediction in the context of our previous finding in Chapter VI that extension speeds are maximal for sprouts developing on matrix densities $0.30 \leq \rho \leq 0.40$. We can infer a positive correspondence between matrix density and the number of cell-ECM contacts and this activation threshold T_I. Also in Chapter VI, we discuss cell proliferation and cell recruitment as complementary mechanisms facilitating sprout extension. In our simulations, when $0.10 \leq T_I < 0.40$, sprout extension speeds did not significantly vary although the distribution of cell

phenotypes in the sprout did. The total number of proliferating and migrating cells in the sprout combined, however, remains approximately constant. This provides additional support to our previous finding that proliferation and migration are complementary mechanisms for sprout extension. For $T_I \geq 0.45$, simulations reveal an increase in apoptotic cells and a consequent interruption of angiogenesis. This result is consistent with what we might expect to occur based on experimental observations. In the model, when this threshold is set high, it is harder for the cell to receive a signal from its integrin receptors and consequently the cell dies. Experimentally it has been shown that endothelial cells will die when they are unable to adhere to the extracellular matrix [64], that is, they are anchorage dependent cells. In the context of angio-therapy, we can relate the effects of altering the threshold for integrin receptor signal transduction to the effects of interfering with integrin receptor binding affinity. When empirical data for the number of receptors and receptor regulation for specific matrix molecules becomes available, using the multi-scale cell-based model we can test specific anti-angiogenic therapies that target integrin receptors.

CHAPTER IX

Summary

9.1 Impact of Dissertation Research

Anti-angiogenic and ECM-targeted strategies are clinically recognized as having enormous potential in the treatment of cancer. Therapeutic advances in these areas could have immediate effects on the lives of millions of cancer patients.

Mathematical modeling and simulation of angiogenesis are becoming increasingly important in the development and testing of anti-angiogenic therapeutic strategies. Ultimately, the aim is to link models of avascular tumor growth, angiogenesis, and vascular tumor growth and metastasis for a complete and predictive model of tumor-induced angiogenesis. While significant progress has been made over the last two decades developing models of tumor-induced angiogenesis, no model couples multiple time and length scales, generates realistic capillary structures including branching and anastomoses without *a priori* prescribing rules and probabilities to these events, and considers the complex biochemical and mechanical interactions that occur between endothelial cells and the ECM. Despite the large body of experimental research on angiogenesis and convincing evidence pointing to the ECM as a critical component of vascular development, previous mathematical investigations have largely treated the ECM as a passive medium, ignoring the interactions between endothelial cells

and the ECM and intracellular signaling pathways in capillary network formation. Mathematical modeling and experimental observations provide convincing evidence that both mechanical and chemical processes may govern tumor-induced angiogenesis and that interactions between tumor cells and endothelial cells within the host environment cannot be ignored.

To advance the current state of mathematical models of tumor-induced angiogenesis, in this dissertation, we develop a multi-scale cell-based model of tumor-induced angiogenesis that integrates a cellular model for cell dynamics explicitly describing key interactions between cells and the ECM, an intracellular signal transduction network highlighting receptor cross-talk for cell decision making, and extracellular reaction-diffusion VEGF dynamics. This research makes significant and novel contributions to and advances the field of mathematical modeling of angiogenesis in the following ways. This model is the first cell-based model of angiogenesis. It facilitates a mechanistic study of the impact of local interactions on the resulting global dynamics of this complex system. Our cell-based model captures changes in cell shape and sprout morphology in time, details that cannot be observed with other models of angiogenesis. Another major advance is that the model contains a more detailed and explicit description of the interactions between cells and the extracellular matrix, interactions that are critical mediators of morphogenic processes. This model also is the first to include a signal transduction network that couples VEGF, integrin, and cadherin pathways and links environmental cues to cell function to elucidate the biochemical mechanisms responsible for new vessel growth. The addition of the signaling network also introduces apoptotic and quiescent cell phenotypes into the model. Cell quiescence and apoptosis have received very little attention in other models of angiogenesis. From only a small set of simple cellular behaviors (growth,

division, migration, and adhesion), the initial model presented in Chapter IV, captures emergent phenomena as evidenced by the formation of new sprout branches and loop formation. These emergent phenomona are also observed with the addition of quiescent and apoptotic cell phenotypes in the multi-scale model. This model is the first to simulate sprout branching without prescribing a phenomenological rule prescribing when and how a branch forms. This puts us in a unique position to explore and predict the mechanisms responsible for new branch formation.

The research completed for this dissertation is relevant not only to those interested in modeling angiogenesis and cell signaling, but also to the larger modeling community because capturing dynamics that occur across multiple time and length scales is a difficult computational and modeling challenge. Our approach is an example of how to integrate three different modeling techniques to bridge multiple scales in the context of tumor angiogenesis. The approach applied here to describe angiogenesis can also be used to model other complex biological systems, such as the immune system response and host-pathogen interactions.

This research is also relevant to experimentalists and clinicians. This model provides a great deal of biological flexibility and has been used to facilitate a deeper understanding of the cellular and molecular interactions associated with angiogenesis. We tested hypotheses formulated from conflicting experimental data to aid in the interpretation of such data and predicted under what conditions critical various sprout morphologies and cell behaviors emerge which can be tested experimentally. Most importantly, our model can be easily modified to mimic other experimental assays and to test new pro- and anti-angiogenic therapies for the treatment of angiogenesis-dependent diseases. Such applications, if they result in therapeutic advances, could have immediate and far-reaching impact.

9.2 Future Outlook

Beyond the research proposed under this dissertation, there is still much to do towards understanding all the mechanisms responsible for angiogenesis to occur. Additional extensions and improvements to the cell-based multi-scale model developed in this thesis research may include incorporating the effects of angiogenic inhibitors, other intracellular signaling pathways and cell cycle controls, explicit protease production and protein expression, variations in oxygen concentrations in the stroma, vessel maturation, and blood flow through the capillaries. Below, we present and partially develop two additional ideas for future model extensions.

9.2.1 Modeling matrix fiber reorganization

It is well-known that endothelial cells actively restructure the extracellular matrix as they migrate. Matrix degradation, which facilitates cell migration through the ECM, is already a feature of this model. ECM remodeling also occurs as a result of endothelial cell matrix production. Endothelial cells synthesize matrix proteins as they move through the ECM, recreating a matrix support structure along which sprouting capillaries can continue to grow and a means by which endothelial cells can self-regulate angiogenic events [147][57]. In Chapters V and VI, we predict optimal densities conducive to angiogenic progress and branching. Endothelial cell matrix secretion may be more likely when matrix density falls below these predicted thresholds. The degree of protein synthesis should affect cell migration and capillary formation and these proteins eventually form the mature vessels' basement membrane structure [147]. Endothelial cell matrix synthesis is easily incorporated into the model by allowing matrix molecules to be secreted by the individual endothelial cells in a manner similar to but opposite of the endothelial cell degradation of matrix.

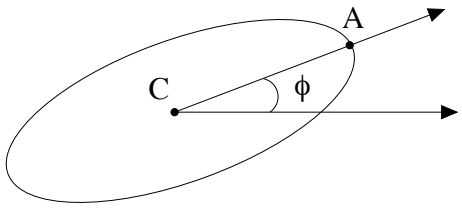

Figure 9.1: The direction of the frictional force exerted by an endothelial cell is quantified by taking the angle of inclination, ϕ, created by the ray joining a cell's center of mass, C, and the point, A, on the cell's boundary along its major axis.

In its role as a support structure for the endothelial cells, the ECM provides a type of scaffolding on which the endothelial cells can move. The cells try to move chemotactically toward higher chemical concentrations, but are additionally influenced by the matrix fibers. To gain traction to move, endothelial cells adhere to fibers in the ECM via cell surface receptors called integrins [34]. Integrin ligation gives rise to a frictional force that can restructure the ECM. These frictional forces act to align the collagen fibers of the ECM forming linear tracks, which in turn strongly influence the direction of endothelial cell migration [165][85]. Consequently, branching and anastomosis have also been associated with the mechanical forces exerted on the ECM by endothelial cells. An endothelial cell will exert a force in the direction it is moving. As a cell moves, it elongates. Therefore, in the model a cell's direction, or orientation, can be considered to be the direction described by the longest distance across the cell and can be quantified relative to the x-axis. Define the angle of inclination, ϕ, as the ray created by joining a cell's center of mass, C, and the point, A, on the cell's boundary (see Figure 9.1) along its major axis. Endothelial cell migration is up a chemical gradient as the cell tries to move to a lower potential energy state. Thus, chemotactic migration produces the force that is exerted on the matrix fibers by the endothelial cells. The difference between the chemical potential at two positions is the amount of energy liberated by moving to lower potential and

is equal to

$$\mu V(\vec{x}) - \mu V(\vec{x}\,')\,.$$

This is the amount of energy now available to do work on matrix fibers. The work will be distributed to (1) overcome friction as the cell moves along the fiber, (2) deform the fiber, and (3) displace the fiber. The work done as the endothelial cell moves along the fiber is equal to the frictional force multiplied by distance. The frictional force is a result of the binding between an endothelial cell and a matrix fiber. The deformation of the fiber is more complicated, and simplifying assumptions will have to be made. Estimates of elasticity and stiffness, which are given by Young's modulus, exist for matrix-like substrates used for *in vitro* experiments that studied how endothelial cells differentially remodel ECM proteins depending on the stiffness of the substrate [55]. Another rich source of parameter values for matrix stiffness is available in Holmes and Sleeman [61].

To implement ECM restructuring into the model, as was done with individual endothelial cells, each matrix fiber possesses its own identifying number or fiber ID. As an endothelial cell comes in contact with a matrix fiber, the cell exerts a force on the fiber which deforms and displaces the fiber. The connectivity of the matrix fibers also needs to be considered, that is, if the force exerted on a fiber by an endothelial cell is large enough, connecting fibers may also be affected. The precise formulation of the total force (friction+deformation+displacement) exerted on a matrix fiber by an endothelial cell has not been developed in the context of the cellular Potts model, but should be based on experimentally measured elasticity parameters, as was done in [99], [61] and similar studies.

The ECM fibrils are thought to strongly influence the direction of EC migration. In addition, we already know ECM topography is a critical regulator of morphogene-

sis. Endothelial cell matrix fiber reorganization, however, has not been characterized in mathematical models. Extending the model developed in this dissertation to explicitly incorporate fibril interactions is likely to provide additional insights into the mechanisms controlling vascular morphology, including sprout branching and anastomosis.

9.2.2 Influence of various VEGF isoforms

Including different VEGF isoforms and VEGF receptors in the model not only improves the physiological accuracy of the system, but also provides a mechanism allowing endothelial cells to respond to their microenvironment based on the actual intracellular signal transduction induced by different VEGF isoform-receptor combinations. Thus, endothelial cells can make informed decisions to migrate or proliferate depending on the type of VEGF form bound, the amount internalized, and whether binding has occurred via integrin receptors or VEGF receptors. In Chapter V, we show that steep versus shallow VEGF gradients markedly influence capillary sprout morphology, but do not explicitly model different VEGF isoforms. Incorporating multiple VEGF isoforms into the multi-scale model of angiogenesis will allow a true analysis of vessel morphology as a function of VEGF profiles to be conducted. The model can then be used to further elucidate how the delicate balance between migration of the tip cell and proliferation of the stalk cells during angiogenesis is achieved and maintained.

Hypotheses, including:

- The release of matrix bound growth factors ($VEGF_{189}$ and $VEGF_{165}$) as a result of matrix degradation by tip cell secreted proteases distinguishes a proliferating region of cells in the vicinity of the tip cell, and

- Different VEGF isoforms play a significant role in the guidance and formation of capillary sprouts

can be investigated by explicitly incorporating VEGF isoforms into the model.

BIBLIOGRAPHY

BIBLIOGRAPHY

[1] H. Abedi and I. Zachary. Signalling mechanisms in the regulation of vascular cell migration. *Cardiovasc. Res.*, 30(4):544 – 556, 1995.

[2] T. Alarcon, H. M. Byrne, and P. K. Maini. A multiple scale model for tumor growth. *SIAM: MMS*, 3(2):440 – 475, 2005.

[3] R. Albert and H. G. Othmer. The topology of the regulatory interactions predicts the expression pattern of the segment polarity genes in drosophila melanogaster. *J. Theor. Biol.*, 223(1):1 – 18, 2003.

[4] B. Alberts, D. Bray, J. Lewis, M. Raff, K. Roberts, and J. D. Watson. *Molecular Biology of the Cell*. Garland Science, New York, fourth edition, 2002.

[5] M. Aldana, E. Balleza, S. Kauffman, and O. Resendiz. Robustness and evolvability in genetic regulatory networks. *J. Theor. Biol.*, 245:433 – 448, 2007.

[6] M. Amano, M. Ito, K. Kimura, Y. Fukata, K. Chihara, T. Nakano, Y. Matsuura, and K. Kaibuchi. Phosphorylation and activation of myosin by Rho-associated kinase (rho-kinase). *J. Biol. Chem.*, 271(34):20246 – 20249, 1996.

[7] G. An. Concepts for developing a collaborative in silico model of the acute inflammatory response using agent-based modeling. *J. Crit. Care*, 21(1):105 – 110, 2006.

[8] A. R. A. Anderson and M. A. J. Chaplain. A mathematical model for capillary network formation in the absence of endothelial cell proliferation. *App. Math. Lett.*, 11:109 – 114, 1997.

[9] A. R. A. Anderson and M. A. J. Chaplain. Continuous and discrete mathematical models of tumor-induced angiogenesis. *Bull. Math. Biol.*, 60:857 – 900, 1998.

[10] T. Asahara, C. Kalka, and J. M. Isner. Stem cell therapy and gene transfer for regeneration. *Gene Ther.*, 7(6):451 – 457, 2000.

[11] D. H. Ausprunk and J. Folkman. Migration and proliferation of endothelial cells in preformed and newly formed blood vessels during tumor angiogenesis. *Microvasc. Res.*, 14:53 – 65, 1977.

[12] A. L. Bauer, T. L. Jackson, and Y. Jiang. A cell-based model exhibiting branching and anastomosis during tumor-induced angiogenesis. *Biophys. J.*, 92:3105 – 3121, 2007.

[13] A. L. Bauer, T. L. Jackson, and Y. Jiang. Topography of extracellular matrix mediates vascular morphogenesis and migration speeds. In revision for *Biophys. J.*, 2007.

[14] Pacific Northwest National Laboratory: Systems Biology.

[15] S. Bornholdt and T. Rohlf. Topological evolution of dynamical networks: Global criticality from local dynamics. *Phys. Rev. Lett.*, 84:6114 – 6117, 2000.

[16] S. Bornholdt and K. Sneppen. Neutral mutations and punctuated equilibrium in evolving genetic networks,. *Phys. Rev. Lett.*, 81:236 – 239, 1998.

[17] S. Braunewell and S. Bornholdt. Superstability of the yeast cell-cycle dynamics: "Ensuring causality in the presence of biochemical stochasticity. *J. Theor. Biol.*, 245(4):638 – 643, 2007.

[18] Y. Cao, H. Chen, L. Zhou, M. Chiang, B. Anand-Apte, J. A. Weatherbee, Y. Wang, F. Fang, J. G. Flanagan, and M. L. Tsang. Heterodimers of placenta growth factor/vascular endothelial growth factor: Endothelial activity, tumor cell expression, and high affinity binding to Flk-1/KDR. *J. Biol. Chem.*, 271(6):3154 – 3162, 1996.

[19] P. Carmeliet. Mechanisms of angiogenesis and arteriogenesis. *Nat. Med.*, 6(4):389 – 395, 2000.

[20] P. Carmeliet. VEGF as a key mediator of angiogenesis in cancer. *Oncology*, 69(supp 3):4 – 10, 2005.

[21] P. Carmeliet and R. K. Jain. Angiogenesis in cancer and other diseases. *Nature*, 407(6801):249 – 257, 2000.

[22] M. A. J. Chaplain and A. M. Stuart. A mathematical model for the diffusion of tumour angiogenesis factor into the surrounding host tissue. *IMA J. Math. Appl. Med. Biol.*, 8:191 – 220, 1991.

[23] M. A. J. Chaplain and A. M. Stuart. A model mechanism for the chemotactic response of endothelial cells to tumour angiogenesis factor. *IMA J. Math. Appl. Med. Biol.*, 10:149 – 168, 1993.

[24] M. Chaves, R. Albert, and E. D. Sontag. Robustness and fragility of Boolean models for genetic regulatory networks. *J. Theor. Biol.*, 235:431 – 449, 2005.

[25] C. S. Chen, M. Mrksich, S. Huang, G. M. Whitesides, and D. E. Ingber. Micropatterned surfaces for control of cell shape, position, and function. *Biotechnol. Prog.*, 14:356 – 363, 1998.

[26] M. E. Chicurel, C. S. Chen, and D. E. Ingber. Cellular control lies in the balance of forces. *Curr. Opin. Cell Biol.*, 10:232 – 239, 1998.

[27] A. D. Cox and C. J. Der. The dark side of Ras: Regulation of apoptosis. *Oncogene*, 22:8999 – 9006, 2003.

[28] A. Czirok, E. D. Perryn, and A. Czirok. Network formation of tissue cells via preferential attraction to elongated structures. *PRL*, 98:038102: 1–4, 2007.

[29] A. Czirok, E. A. Zamir, M. B. Filla, C. D. Little, and B. J. Rongish. Extracellular matrix macroassembly dynamics in early vertebrate embryos. *Curr. Top. Dev. Biol.*, 73:237 – 258, 2006.

[30] S. R. Datta, A. Brunet, and M. E. Greenberg. Cellular survival: A play in three Akts. *Genes Dev.*, 13:2905 – 2927, 1999.

[31] M. I. Davidich and S. Bornholdt. Boolean network model predicts cell cycle sequence of fission yeast. *arXiv: q-bio*, page 1313440, 2007.

[32] G. Davis and C. W. Camarillo. An $\alpha 2\beta 1$ integrin-dependent pinocytic mechanism involving intracellular vacuole formation and coalescence regulates capillary lumen and tube formation in three-dimensional collagen matrix. *Exp. Cell Res.*, 224:39 – 51, 1996.

[33] G. E. Davis, W. Koh, and A. N. Stratman. Mechanisms controlling human endothelial lumen formation and tube assembly in three-dimensional extracellular matrices. *Birth Defects Res. C Embryo Today*, page In press, 2007.

[34] G. E. Davis and D. R. Senger. Endothelial extracellular matrix: Biosynthesis, remodeling, and functions during vascular morphogenesis and neovessel stabilization. *Circ. Res.*, 97:1093 – 1107, 2005.

[35] T. Demuth and M. E. Berens. Molecular mechanisms of glioma cell migration and invasion. *J. Neurooncol.*, 70:217 – 228, 2004.

[36] B. Derrida and Y. Pomeau. Random networks of automata: A simple annealed approximation. *Europhys. Lett.*, 1(2):45 – 49, 1986.

[37] D. E. Discher, P. Janmey, and Y. Wang. Tissue cells feel and respond to the stiffness of their substrate. *Science*, 310:1139 – 1143, 2005.

[38] S. T. Eblen, J. K. Slack, M. J. Weber, and A. D. Catling. Rac-PAK signaling stimulates extracellular signal-regulated kinase (ERK) activation by regulating formation of MEK1-ERK complexes. *Mol. Cell. Biol.*, 22(17):6023 – 6033, 2002.

[39] N. Ferrara, H. Gerber, and J. LeCouter. The biology of VEGF and its receptors. *Nat. Med.*, 9(6):669 – 676, 2003.

[40] N. Ferrara and W. J. Henzel. Pituitary follicular cells secrete a novel heparin-binding growth factor specific for vascular endothelial cells. *Biochem. Biophys. Res. Commun.*, 161:851 – 858, 1989.

[41] I. Fiddler and L. M. Ellis. Angiogenesis and breast cancer metastasis. *Lancet*, 346:488 – 489, 1995.

[42] J. Folkman. Vascularization of tumors. *Sci. Am.*, 234(5):58 – 64, 1976.

[43] G. Forgacs. On the possible role of cytoskeletal filamentous networks in intracellular signaling: An approach based on percolation. *J. Cell Sci.*, 108:2131 – 2143, 1995.

[44] P. Friedl and E. B. Bröcker. The biology of cell locomotion within three-dimensional extracellular matrix. *Cell. Mol. Life Sci.*, 57(1):41 – 64, 2000.

[45] P. Friedl, Y. Hegerfeldt, and M. Tusch. Collective cell migration in morphogenesis and cancer. *Int. J. Dev. Biol.*, 48(5-6):441 – 449, 2004.

[46] F. Mac Gabhann and A. S. Popel. Model of competitive binding of vascular endothelial growth factor and placental growth factor to VEGF receptors on endothelial cells. *Am. J. Physiol. Heart Circ. Physiol.*, 286:153 – 164, 2004.

[47] P. Gagne, A. Akalu, and P. C. Brooks. Challenges facing antiangiogenic therapy for cancer: impact of the tumor extracelluar environment. *Expert Rev. Anticancer Ther.*, 4(1):129 – 140, 2004.

[48] H. P. Gerber, K. J. Hillan, A.M. Ryan, J. Kowalski, G. A. Keller, L. Rangell, B. D. Wright, F. Radtke, M. Aguet, and N. Ferrara. VEGF is required for growth and survival neonatal mice. *Dev.*, 126:1149 – 1159, 1999.

[49] H. P. Gerber, A. McMurtrey, J. Kowalski, M. Yan, B. A. Keyt, V. Dixit, and N. Ferrara. Vascular endothelial growth factor regulates endothelial cell survival through the phosphatidylinositol 3'-kinase/Akt signal transduction pathway. *J. Biol. Chem.*, 273(46):30336 – 30343, 1998.

[50] H. Gerhardt, M. Golding, M. Fruttiger, C. Ruhrberg, A. Lundkvist, A. Abramsson, M. Jeltsch, C. Mitchell, K. Alitalo, D. Shima, and C. Betsholtz. VEGF guides angiogenic sprouting utilizing endothelial tip cell filopodia. *J. Cell Biol.*, 161:1163 – 1177, 2003.

[51] C. Gershenson. Updating schemes in random Boolean networks: Do they really matter? In *ARTIFICIAL LIFE IX*, pages 238 – 243. M I T PRESS, 2004.

[52] M. A. Gimbrone, R. S. Cotran, S. B. Leapman, and J. Folkman. Tumor growth and neovascularization: An experimental model using the rabbit cornea. *J. Natl. Cancer Inst.*, 52:413 – 427, 1974.

[53] J. A. Glazier and F. Graner. Simulation of the differential adhesion driven arrangement of biological cells. *Phys. Rev. E*, 47:2128 – 2154, 1993.

[54] F. Goto, K. Goto, K. Weindel, and J. Folkman. Synergistic effects of vascular endothelial growth factor and basic fibroblast growth factor on the proliferation and cord formation of bovine capillary endothelial cells within collagen gels. *Lab. Invest.*, 69(5):508 – 517, 1993.

[55] D. S. Gray, J. Tien, and C. S. Chen. Repositioning of cells by mechanotaxis on surfaces with micropatterned Young's modulus. *Cell Science*, 66(A):605 – 614, 2002.

[56] M. Hangai, N. Kitaya, J. Xu, C. Chan, J. Kim, Z. Werb, S. Ryan, and P. Brooks. Matrix metalloproteinase-9-dependent exposure of a cryptic migratory control site in collagen is required before retinal angiogenesis. *Am. J. Path.*, 161:1429 – 1437, 2002.

[57] G. C. Haralabopoulos, D. S. Grant, H. K. Kleinman, P. Lelkes, S. P. Popaioannou, and M. E. Maragoudakis. Inhibitors of basement membrane collagen synthesis prevent endothelial cell alignment in matrigel in vitro and angiogenesis in vivo. *Lab. Invest*, 71:575 – 582, 1994.

[58] D. J. Hicklin and L. M. Ellis. Role of the vascular endothelial growth factor pathway in tumor growth and angiogenesis. *J. Clin. Onc.*, 23(5):1011 – 1027, 2005.

[59] K. K. Hirschi and P. A. D'Amore. Control of angiogenesis by the pericyte: molecular mechanisms and significance. *EXS*, 79:419 – 428, 1997.

[60] P. Hogeweg. Evolving mechanisms of morphogenesis: on the interplay between differential adhesion and cell differentaition. *J. Theor. Biol.*, 203:317 – 333, 2000.

[61] M. J. Holmes and D. B. Sleeman. A mathematical model of tumour angiogenesis incorporating cellular traction and viscoelastic effects. *J. Theor. Biol.*, 202(95):95 – 112, 2000.

[62] J. R. Hotchkiss, D. G. Strike, D. A. Simonson, A. F. Broccard, and P. S. Crooke. An agent-based and spatially explicit model of pathogen dissemination in the intensive care unit. *Crit. Care Med.*, 33(1):168 – 76; discussion 253, 2005.

[63] K. A. Houck, D. W. Leung, A. M. Rowland, J. Winer, and N. Ferrara. Dual regulation of vascular endothelial growth factor bioavailability by genetic and proteolytic mechanisms. *J. Biol. Chem.*, 267:26031 – 26037, 1992.

[64] S. Huang and D. E. Ingber. The structural and mechanical complexity of cell-growth control. *Nat. Cell Biol.*, 1(5):E131 – E138, 1999.

[65] W. L. Hunter and L. A. Arsenault. Vascular invasion of the epithelial growth plate: Analysis of metaphyseal capillary ultrastructure and growth dynamics. *Anat. Rec.*, 227:223 – 231, 1990.

[66] H. Hutchings, N. Ortega, and J. Plout. Extracellular matrix-bound vascular endothelial growth factor promotes endothelial cell adhesion, migration, and survival through integrin ligation. *FASEB J.*, 17(11):1520 – 1522, 2003.

[67] The Angiogenesis Foundation Inc., 2000.

[68] D. E. Ingber and J. Folkman. Mechanochemical switching between growth and differentiation during fibroblast growth factor-stimulated angiogenesis *in vitro*: Role of extracellular matrix. *J. Cell Biol.*, 109:317 – 330, 1989.

[69] M. L. Iruela-Arispe, P. Hasselaar, and H. Sage. Differential expression of extracellular proteins is correlated with angiogenesis in vitro. *Lab. Invest.*, 64:174, 1991.

[70] T. Ishizaki, M. Naito, K. Fujisawa, M. Maekawa, N. Watanabe, Y. Saito, and S. Narumiya. p160ROCK, a Rho-associated coiled-coil forming protein kinase, works downstream of Rho and induces focal adhesions. *FEBS Lett.*, 404:118 – 124, 1997.

[71] E. R. Jackson, D. Johnson, and W. G. Nash. Gene networks in development. *J. Theor. Biol.*, 119(4):379 – 396, 1986.

[72] H. V Jain, J. E. Nor, and T. L. Jackson. Modeling the VEGF-Bcl2-CXCL8 pathway in intratumoral angiogenesis. To appear in *Bull. Math. Biol.*, 2007.

[73] A. Jemal, T. Murray, E. Ward, A. Samuels, R. C. Tiwari, A. Ghafoor, E. J. Feuer, and M. J. Thun. Cancer statistics 2005. *CA. Cancer J. Clin.*, 55(4):259, 2005.

[74] Y. Jiang, H. Levine, and J. A. Glazier. Possible cooperation of differential adhesion and chemotaxis in mound formation of *dictyostelium*. *Biophys. J.*, 75:2615 – 2625, 1998.

[75] Y. Jiang, J. Pjesivac-Grbovic, C. Cantrell, and J. P. Freyer. A multiscale model for avascular tumor growth. *Biophys. J.*, 89:3884 – 3894, 2005.

[76] S. A. Kauffman. Metabolic stability and epigenesis in randomly constructed genetic nets. *J. Theor. Biol.*, 22:437 – 467, 1969.

[77] S. A. Kauffman. *The origins of order: Self-organization and selection in evolution*. Oxford University Press, first edition, 1993.

[78] L. J. Kaufman, C. P. Brangwynne, K. E. Kasza, E. Filippidi, V. D. Gordon, T. S. Deisboeck, and D. A. Weitz. Glioma expansion in collagen I matrices: Analyzing collagen concentration-dependent growth and motility patterns. *Biophys. J.*, 89:635 – 650, 2005.

[79] J. B. Kearney, N. C. Kappas, C. Ellerstrom, F. W. DiPaola, and V. L. Bautch. The VEGF receptor flt–1 (VEGFR–1) is a positive modulator of vascular sprout formation and branching morphogenesis. *Blood*, 103:4527 – 4535, 2004.

[80] P. J. Keely, J. K. Westwick, I. P. Whitehead, C. J. Der, and L. V. Parise. Cdc42 and Rac1 induce integrin-mediated cell motility and invasiveness through PI(3)K. *Nature*, 390:632 – 636, 1997.

[81] E. Keshet and S. A. Ben-Sasson. Anticancer drug targets: approaching angiogenesis. *J. Clin. Invest.*, 104(11):1497 – 1501, 1999.

[82] D. E. Kirschner, S. T. Chang, T. W. Riggs, N. Perry, and J. J. Linderman. Toward a multiscale model of antigen presentation in immunity. *Immun. Rev.*, 216:93 – 118, 2007.

[83] K. Klemm and S. Bornholdt. Robust gene regulation: Deterministic dynamics from asynchronous networks with delay. *arXiv: q-bio*, page 0309013, 2003.

[84] K. Klemm and S. Bornholdt. Stable and unstable attractors in Boolean networks. *Phys. Rev. E*, 72:055101(R), 2005.

[85] T. Korff and H. G. Augustin. Tensional forces in fibrillar extracellular matrices control directional capillary sprouting. *J. Cell Sci.*, 112:3249 – 3258, 1999.

[86] L. Krishnan, H. Ngyuen, H. Song, J. B. Hoying, and J. A. Weiss. Gene expression in a 3-dimensional model of angiogenesis: Relation to matrix mechanical properties. In *2005 Summer Bioengineering Conference, Vail, Colorado, USA*, 2005.

[87] K. E. Kürten. Correspondence between neural threshold networks and Kauffman Boolean cellular automata. *J. Phys. A*, 21(11):L615 – L619, 1988.

[88] K. E. Kürten. Critical phenomena in model neural networks. *Phys. Lett. A*, 129(3):157 – 160, 1988.

[89] M. G. Lampugnani, A. Zanetti, M. Corada, T. Takahashi, G. Balconi, F. Breviario, F. Orsenigo, A. Cattelino, R. Kemler, T. O. Daniel, and E. Dejana. Contact inhibition of VEGF-induced proliferation requires vascular endothelial cadherin, β-catenin, and the phosphatase DEP-1/CD148. *J. Cell Biol.*, 161(4):793 – 804, 2003.

[90] G. J. Laurent. Dynamic state of collagen: Pathways of collagen degradation in vivo and their possible role in regulation of collagen mass. *Am. J. Physiol., Cell Physiol.*, 252(1):C2 – C9, 1987.

[91] S. Lee, S. M. Jilani, G. V. Nikolava, D. Carpizo, and M. L. Iruela-Arispe. Processing of VEGF-A by matrix metalloproteinases regulates bioavailability and vascular patterning in tumors. *J. Cell Biol.*, 169(4):681 – 691, 2005.

[92] S. J. Leevers, B. Vanhaesebroeck, and M. D. Waterfield. Signaling through phosphoinositide 3-kinases: The lipids take centre stage. *Curr. Opin. Cell Biol.*, 11:219 – 225, 1999.

[93] J. T. Leith and S. Michelson. Secretion rates and levels of vascular endothelial growth factor in clone A or HCT-8 human colon tumour cells as a function of oxygen concentration. *Cell Prolif.*, 28:415 – 430, 1995.

[94] J. R. Levick. Flow through interstitium and other fibrous matrices. *Q. J. Exp. Physiol.*, 72:409 – 437, 1987.

[95] H. A. Levine, S. Pamuk, B. D. Sleeman, and M. Nilsen-Hamilton. Mathematical modeling of capillary formation and development in tumor angiogenesis: Penetration into the stroma. *Bull. Math. Biol.*, 63:801 – 863, 2001.

[96] H. A. Levine, A. L. Tucker, and M. Nilsen-Hamilton. A mathematical model for the role of cell signal transduction in the initiation and inhibition of angiogenesis. *Growth Factors*, 20(4):155 – 175, 2002.

[97] S. Li, S. M. Assmann, and R. Albert. Predicting essential components of signal transduction networks: A dynamic model of guard cell abscisic acid signaling. *PLoS Biology*, 4(10):1732–1748, 2006.

[98] J. Lilien and J. Balsamo. The regulation of cadherin-mediated adhesion by tyrosine phosphorylation/deposphorylation of β-catenin. *Curr. Opin. Cell Biol.*, 17:459 – 465, 2005.

[99] C. Lo and J. Ferrier. Electrically measuring viscoelastic parameters of adherent cell layers under controlled magnetic forces. *Eur. Biophys. J.*, 28:112 – 118, 1999.

[100] C. Lo, H. Wang, M. Dembo, and Y. Wang. Cell movement is guided by the rigidity of the substrate. *Biophys. J.*, 79:144 – 152, 2000.

[101] I. B. Lobov, P. C. Brooks, and R. A. Lang. Angioproietin-2 displays VEGF-dependent modulation of capillary structure and endothelial cell survival in vivo. *Proc. Natl. Acad. Sci. U.S.A.*, 99(17):11205 – 11210, 2002.

[102] P. M. Lowe, M. L. Lee, C. J. Jackson, S. S. To, A. J. Cooper, and L. Schrieber. The endothelium in psoriases. *Br. J. Dermatol.*, 132:497 – 505, 1995.

[103] B. Luque and R. V. Solé. Phase transitions in random networks: Simple analytic determination of critical points. *Phys. Lett. E*, 55(1):257 – 260, 1997.

[104] D. J. G. Mackay and A. Hall. Rho GTPases. *J. Biol. Chem.*, 273:20685 – 20688, 1998.

[105] D. Manoussaki. A mechanochemical model of angiogenesis and vasculogenesis. *ESAIM: M2NA*, 37(4):581 – 599, 2003.

[106] D. Manoussaki, S. R. Lubkin, R. B. Vernon, and J. D. Murray. A mechanical model for the formation of vascular networks *in vitro*. *Acta Biotheor.*, 42:271 – 282, 1996.

[107] N. V. Mantzaris, S. Webb, and H. G. Othmer. Mathematical modeling of tumor-induced angiogenesis. *J. Math. Biol.*, 49:111 – 187, 2004.

[108] L. A. Martinez-Lemus, X. Wu, E. Wilson, M. A. Hill, G. E. Davis, M. J. Davis, and G. A. Meininger. Integrins as unique receptors for vascular control. *J. Vasc. Res.*, 40:211 – 233, 2003.

[109] S. R. McDougall, A. R. A. Anderson, and M. A. J. Chaplain. Mathematical modelling of dynamic adaptive tumor-induced angiogenesis: clinical implications and therapeutic targeting strategies. *J. Theor. Biol.*, 241:564 – 589, 2006.

[110] R. M. H. Merks, S. V. Brodsky, M. S. Goligorksy, S. A. Newman, and J. A. Glazier. Cell elongation is key to in silico replication of in vitro vasculogenesis and subsequent remodeling. *Dev. Biol.*, 289:44 – 54, 2006.

[111] R. M. H Merks and J. A. Glazier. Dynamic mechanisms of blood vessel growth. *Nonlin.*, 19:C1 – C10, 2006.

[112] K. S. Midwood, L. V. Williams, and J. E. Schwarzbauer. Tissue repair and the dynamics of the extracellular matrix. *Int. J. Biochem. Cell Biol.*, 36(6):103 – 1037, 2004.

[113] P. Mignatti and D. B. Rifkin. Biology and biochemistry of proteinases in tumor invasion. *Physiol. Rev.*, 73(1):161 – 195, 1993.

[114] T. Mihaljev and B. Drossel. Scaling in a general class of critical random Boolean networks. *Phys. Rev. E*, 74:046101, 2006.

[115] J. D. Murray, G. Oster, and A. Harris. A mechanical model for mesenchymal morphogenesis. *J. Math. Biol.*, 17:125 – 129, 1983.

[116] V. R. Muthukkaruppan, L. Kubai, and R. Auerbach. Tumor-induced neovascularization in the mouse eye. *J. Natl. Cancer Inst.*, 69:699 – 704, 1982.

[117] H. Nakahara, L. Howard, E. W. Thompson, H. Seiki, M. Sato, Y. Yeh, and W. Chen. Transmembrane/cytoplasmic domain-mediated membrane type 1-matrix metalloproteinase docking to invadopodia is required for cell invasion. *Proc. Natl. Acad. Sci.*, 94(15):7959 – 7964, 1997.

[118] C. D. Nobes and A. Hall. Rho, rac, and cdc42 GTPases regulate the assembly of multimolecular focal complexes associated with actin stress fibers, lamellipodia, and filopodia. *Cell*, 18:53 – 62, 1995.

[119] C. D. Nobes and A. Hall. Rho GTPases control polarity, protrusion, and adhesion during cell movement. *J. Cell Biol.*, 144:1235 – 1244, 1999.

[120] J. E. Nör, J. Christensen, D. J. Mooney, and P. J. Polverini. Vascular endothelial growth factor (VEGF)-mediated angiogenesis is associated with enhanced endothelial cell survival and induction of bcl-2 expression. *Am. J. Path.*, 154(2):375 – 384, 1999.

[121] C. Oakley, N. A. F. Jaeger, and D. M. Brunette. Sensitivity of fibroblasts and their cytoskeletons to substratum topographies: Topographic guidance and topographic compensation by micromachined grooves of different dimensions. *Exp. Cell Res.*, 234:413 – 424, 1997.

[122] KEGG: Kyoto Encyclopedia of Genes and Genomes, 1995 – 2007.

[123] K. Okumura, M. Mendoza, R. M. Bachoo, R. A. DePinho, W. K. Cavenee, and F. B. Furnari. PCAF modulates PTEN activity. *J. Biol. Chem.*, 281(36):26562 – 26568, 1996.

[124] N. Paweletz and M. Knierim. Tumor related angiogenesis. *Crit. Rev. Oncol. Hematol.*, 9:197 – 242, 1989.

[125] S. M. Peirce, E. J. Van Gieson, and T. C. Skalak. Multicellular simulation predicts microvascular patterning and in silico tissue assembly. *FASEB J.*, 18(6):731 – 733, 2004.

[126] M. J. Plank, D. B. Sleeman, and P. F. Jones. The role of the angiopoietins in tumour angiogenesis. *Growth Factors*, 22(1):1 – 11, 2004.

[127] T. D. Pollard and G. G. Borisy. Cellular motility driven by assembly and disassembly of actin filaments. *Cell*, 112:453 – 465, 2003.

[128] P. Rafiee, J. Heidemann, H. Ogawa, N. A. Johnson, P. J. Fisher, M. S. Li, M. F. Otterson, C. P. Johnson, and D. G. Binion. Cyclosporin a differentially inhibits multiple steps in VEGF induced angiogenesis in human microvascular endothelial cells through altered intracellular signaling. *Cell Commun. Signal.*, 2(1):3, 2004.

[129] W. G. Roberts and G. E. Palade. Increased microvascular permeability and endothelial fenestration induced by vascular endothelial growth factor. *J. Cell Sci.*, 108:2369 – 2379, 1995.

[130] B. A. Roeder, K. Kokini, B. Z. Waisner, J. E. Sturgis, J. P. Robinson, and S. L. Voytik-Harbin. Extracellular matrix microstructure determines ecm-cell strain transfer in 3D tissue constructs. In *2003 Summer Bioengineering Conference, Key Biscayne, Florida, USA*, 2003.

[131] T. Rohlf. The critical line in random threshold networks with inhomogeneous thresholds. *arXiv: Condensed Matter*, page 07073621, 2007.

[132] T. Rohlf and S. Bornholdt. Criticality in random threshold networks: Annealed approximation and beyond. *Physica A*, 310(1 – 2):245 – 259, 2002.

[133] T. Rohlf and S. Bornholdt. Self-organized pattern formation and noise-induced control based on particle computations. *JSTAT*, L12001:379 – 396, 2005.

[134] C. Ruhrberg, H. Gerhardt, M. Golding, R. Watson, S. Ioannidou, H. Fujisawa, C. Betsholtz, and D. T. Shima. Spatially restricted patterning cues provided by heparin-binding VEGF-A control blood vessel branching morphogenesis. *Gene Dev.*, 16:2684 – 2698, 2002.

[135] E. Ruoslahti. Control of cell motility and tumor invasion by extracellular matrix interactions. *Br. J. Cancer*, 66(2):239 – 242, 1992.

[136] E. Ruoslahti and J. C. Reed. Anchorage dependence, integrins, and apoptosis. *Cell*, 77:477 – 478, 1994.

[137] P. A. Rupp and C. D. Little. Integrins in vascular development. *Circ. Res*, 89:566 – 572, 2001.

[138] R. C. Sainson, J. Aoto, M. N. Nakatsu, M. Holderfield, E. Conn, E. Koller, and C. C. Hughes. Cell-autonomous notch signaling regulates endothelial cell branching and proliferation during vascular tubulogenesis. *FASEB J.*, 19(8):1027 – 1029, 2005.

[139] Y. Sakumura, Y. Tsukada, N. Yamamoto, and S. Ishii. A molecular model for axon guidance based on crosstalk between rho GTPases. *Biophys. J.*, 89:812 – 822, 2005.

[140] B. Samuelson and C. Troein. Superpolynomial growth in the number of attractors in Kauffman networks. *Phys. Rev. Lett.*, 90:098701, 2003.

[141] B. Samuelsson and J. E. S. Socolar. Exhaustive percolation on random networks. *Phys. Rev. E*, 74:036113, 2006.

[142] E. E. Sandera, J. P. ten Kloostera, S. van Delfta, R. A. van der Kammena, and J. G. Collarda. Rac downregulates rho activity: Reciprocal balance between both GTPases determines cellular morphology and migratory behavior. *J. Cell Biol.*, 147:1009 – 1022, 1999.

[143] S. M. Schoenwaelder and K. Burridge. Bidirectional signaling between the cytoskeleton and integrins. *Curr. Opin. Cell Biol.*, 11:274 – 286, 1999.

[144] M. A. Schwartz, M. D. Schaller, and M. H. Ginsberg. Integrins: Emerging paradigms of signal transduction. *Annu. Rev. Cell Dev. Biol.*, 11:549 – 599, 1995.

[145] J. Segovia-Juarez, S. Ganguli, and D. E. Kirschner. Identifying control mechanisms of granuloma growth during *mycobacterium* tuberculosis infection using an agent based model. *J. Theor. Biol.*, 231:357 – 376, 2004.

[146] D. R. Senger, K. P. Claffey, J. E. Benes, C. A. Perruzzi, A. P. Sergiou, and M. Detmar. Angiogenesis promoted by vascular endothelial growth factor: Regulation through alpha 1 beta 1 and alpha 2 beta 1 integrins. *Proc. Natl. Acad. Sci. U.S.A.*, 94:13612 – 13617, 1997.

[147] G. C. Sephel, R. Kennedy, and S. Kudravi. Expression of capillary basement membrane components during sequential phases of wound angiogenesis. *Matrix Biol.*, 15:263 – 279, 1996.

[148] G. Serini, D. Ambrosi, E. Giraudo, A. Gamba, L. Preziosi, and F. Bussolino. Modeling the early stages of vascular network assembly. *EMBO J.*, 22:1771 – 1779, 2003.

[149] Y. Shiu, S. Li, W. A. Marganski, S. Usami, M. A. Schwartz, Y. Wang, M. Dembo, and S. Chien. Rho mediates the shear enhancement of endothelial cell migration and traction force generation. *Biophys. J.*, 86:2558 – 2565, 2004.

[150] Y. Shizukuda, S. Tang, R. Yokota, and J. A. Ware. Vascular endothelial growth factor-induced endothelial cell migration and proliferation depend on a nitric oxide-mediated decrease in protein kinase cδ activity. *Circ. Res.*, 85:247 – 256, 1999.

[151] M. M. Sholley, G. P. Ferguson, H. R. Seibel, J. L. Montour, and J. D. Wilson. Mechanisms of neovascularization. Vascular sprouting can occur without proliferation of endothelial cells. *Lab. Invest.*, 51:624 – 634, 1984.

[152] F. H. Silver, J. W. Freeman, and G. P. Seehra. Collagen self-assembly and the development of tendon mechanical properties. *J. Biomech.*, 36:1529 – 1553, 2003.

[153] R. V. Solé and B. Luque. Phase transitions and antichaos in generalized kauffman networks. *Phys. Lett. A*, 196(5 – 6):331 – 334, 1995.

[154] W. G. Stetler-Stevenson. Matrix metalloproteinases in angiogenesis: A moving target for therapeutic intervention. *J. Clin. Invest.*, 103:1237 – 1241, 1999.

[155] C. L. Stokes and G. A. Lauffenburger. Analysis of the roles of microvessel endothelial cell random motility and chemotaxis in angiogenesis. *J. Theor. Biol.*, 152:377 – 403, 1991.

[156] O. Straume, H. B. Salvesen, and L. A. Akslen. Angiogenesis is prognostically important in vertical growth phase melanomas. *Int. J. Oncol.*, 15(3):595 – 599, 1999.

[157] S. Stromblad, J. C. Becker, P. C. Brooks M. Yebra, and D. A. Cheresh. Suppression of p53 activity and p21WAF1/CIP1 expression by vascular cell integrin alphaVbeta3 during angiogenesis. *J. Clin. Invest.*, 98(2):426 – 433, 1996.

[158] S. Sun, M. F. Wheeler, M. Obeyesekere, and C. W. Patrick. A deterministic model of growth-factor induced angiogenesis. *Bull. Math. Biol.*, 67:131 – 337, 2005.

[159] N. Gulbhace T. Rohlf and C. Teuscher. Damage spreading and criticality in finite random dynamical networks. *arXiv: Condensed Matter*, page 0701601, 2007.

[160] R. T. Tranquillo. Self-organization of tissue-equivalents: The nature and role of contact guidance. *Biochem. Soc. Symp.*, 65:27 – 42, 1999.

[161] S. Turner and J. A. Sherratt. Intercellular adhesion and cancer invasion: A discrete simulation using the extended Potts model. *J. Theor. Biol.*, 216:85 – 100, 2002.

[162] T. Mihaljev V. Kaufman and B. Drossel. Scaling in critical random Boolean networks. *Phys. Rev. E*, 72:046124, 2005.

[163] F. N. van Leeuwen, H. E. T. Kain, R. A. van der Kammen, F. Michiels, O. W. Kranenburg, and J. G. Collard. The guanine nucleotide exchange factor Tiam1 affects neuronal morphology; Opposing roles for the small GTPases rac and rho. *J. Cell Biol.*, 139:797 – 807, 1997.

[164] R. B. Vernon, J. C. Angello, M. L. Iruela-Arispe, T. F. Lane, and E. H. Sage. Reorganization of basement membrane matrices by cellular traction promotes the formation of cellular networks *in vitro*. *Lab. Invest.*, 66:536 – 547, 1992.

[165] R. B. Vernon and E. H. Sage. Between molecules and morphology: Extracellular matrix and the creation of vascular form. *Am. J. Pathol.*, 147:873 – 883, 1995.

[166] G. von Dassow, E. Meir, E. M. Munro, and G. M. Odell. The segment polarity network is a robust developmental module. *Nature*, 406:188 – 192, 2000.

[167] J. Waltenberger, L. Claesson-Welsh, A. Siegbahn, M. Shibuya, and C. H. Heldin. Different signal transduction properties of kdr and flt1, two receptors for vascular endothelial growth factor. *J. Biol. Chem.*, 269:26988 – 26995, 1994.

[168] D. Wang, R. E. Lehman, D. B. Donner, M. R. Matli, R. S. Warren, and M. L. Welton. Expression and endocytosis of VEGF and its receptors in human colonic vascular endothelial cells. *Am. J. Physiol. Gastrointest. Liver Physiol.*, 282:1088 – 1096, 2002.

[169] K. B. Wee and B. D. Aguda. Akt versus p53 in a network of oncogenes and tumor suppressor genes regulating cell survival and death. *Biophys. J.*, 91:857 – 865, 2006.

[170] S. K. Williams. Isolation and culture of microvessel and large-vessel endothelial cells; Their use in transport and clinical studies. In P. F. McDonagh, editor, *Microvascular Perfusion and Transport in Health and Disease*, pages 204 – 245. S. Karger AG, Basel, Switzerland, 1987.

[171] G. D. Yancopoulos, S. Davis, N. W. Gale, J. S. Rudge, S. J. Wiegand, and J. Holash. Vascular-specific growth factors and blood vessel formation. *Nature*, 407:242 – 248, 2000.

[172] A. Yoshida, B. Anand-Apte, and B. R. Zetter. Differential endothelial migration and proliferation to basic fibroblast growth factor and vascular endothelial growth factor. *Growth Factors*, 13(1-2):57 – 64, 1996.

[173] A. Zanetti, M. G. Lampugnani, G. Balconi, F. Breviario, M. Corada, L. Lanfrancone, and E. Dejana. Vascular endothelial growth factor induces shc association with vascular endothelial cadherin: A potential feedback mechanism to control vascular endothelial growth factor receptor-2 signaling. *Arterioscler. Thromb. Vasc. Biol.*, 22:617 – 622, 2002.

[174] D. F. Zawicki, R. K. Jain, G. W. Schmid-Schoenbein, and S. Chien. Dynamics of neovascularization in normal tissue. *Microvasc. Res.*, 21:27 – 47, 1981.

[175] B. R. Zetter. Angiogenesis and tumor metastasis. *Annu. Rev. Med.*, 49:407 – 427, 1998.

[176] L. Zhang, C. A. Athale, and T. S. Deisboeck. Development of a three-dimensional multiscale agent-based tumor model: Simulating gene-protein interaction profiles, cell phenotypes and multicellular patterns in brain cancer. *J. Theor. Biol.*, 244:96 – 107, 2007.